Role of Transcription Factor EB in obesity mediated cardiac dysfunction.

by

Adithi Pisapati

Submitted in partial fulfillment of the requirements

for the degree of Master of Science

at

Dalhousie University

Halifax, Nova Scotia

August 2023

©Copyright by Adithi Pisapati, 2023

Table of Contents

List of Tables

List of Figures

Abstract

Lipotoxic complications drive impairment in cardiac function during obesity. Specifically, palmitate toxicity induces ER stress, calcium mishandling and perturbations in lysosomal function by downregulating transcription factor EB (TFEB). This study aims to understand the mechanisms behind palmitate-induced TFEB decline in the heart and the consequences of cardiomyocyte-specific TFEB deletion during obesity. Elevated miR-30b-5p levels were observed in palmitate-treated cells and obese patients' atrial appendages while inhibiting miR-30 prevented TFEB protein decline. Moreover, palmitate significantly accelerated TFEB protein degradation, even in the presence of proteasomal inhibitors, suggesting the involvement of plausible lysosomal degradative mechanisms. Furthermore, cardiomyocyte-specific TFEB deletion in mice fed a high-fat diet resulted in increased body weight, impaired insulin signaling, altered lipid storage, reduced substrate oxidation, changes in calcium transient amplitudes, and cardiac dysfunction, with sex-specific differences. Data from this thesis uncovered the novel role of miR-30b-5p in palmitate-induced TFEB decline and the sex-specific impact of myocyte TFEB insufficiency in the development of obesity-related cardiomyopathy.

List of Abbreviation and Symbols Used

AA	Atrial appendage
ACSL	Acetyl-CoA synthase
ADP	Adenosine diphosphate
Akt	Protein Kinase B
AMCM	Adult mouse cardiomyocyte
Ang-II	Angiotensin II
ANOVA	Analysis of variance formula
APV	A-wave peak velocity
ARCM	Adult rat cardiomyocyte
ATF	Activating transcription factor
Atg	Autophagy related
ATGL	Adipose triglyceride lipase
ATP	Adenosine triphosphate
AV	Aortic valve
BAT	Brown adipose tissue
BCA	Bicinchoninic acid
Bcl-2	B-cell lymphoma 2
bHLHZip	The basic/helix-loop-helix Zipper
BMI	Body Mass Index
BSA	Bovine serum albumin
CHOP	DNA damage-inducible transcript 3
CHX	Cycloheximide
CLEAR	Coordinated lysosomal expression and regulation
CMA	Chaperone mediated autophagy
CMBCD	Cardiometabolic-based chronic disease
CPT	Carnitine-palmitoyl transferase
CVD	Cardiovascular disease
DAG	Diacylglycerol
DGCR8	DiGeorge critical region-8
DIO	Diet-induced obesity
DMEM	Dulbecco's Modified Eagle Medium
DMSO	Dimethylsulfoxide
DOX	Doxorubicin
DTT	Dithiothreitol
ECG	Electrocardiogram
eIF2a	Eukaryotic Translation Initiation Factor 2A
EPV	E-wave peak velocity
ER	Endoplasmic reticulum
ERAD	Endoplasmic reticulum-associated degradation
ERK	Extracellular receptor kinase

ETC	Electron transport chain
FA	Fatty acid
FAO	Fatty acid oxidation
FATP	Fatty acid transporter protein
FBS	Fetal bovine serum
FFA	Free fatty acid
Fitm2	Fat Storage Inducing Transmembrane Protein 2)
FOXO3	transcription factor forkhead box O-3
G-6-P	Glucose 6-phosphate
GADD153	Growth Arrest and DNA damage-inducible 153
GLUT	Glucose transporter
HBP	Hexosamine biosynthesis pathway
HF	Heart failure
HIF-1α	Hypoxia-inducible factor 1a
HR	Heart rate
Hsc70	Heat shock cognate 71-kDa protein
HSL	Hormone-sensitive lipase
Hsp90	Heat shock protein
i.p	Intra peritoneal
IR	Insulin resistance
IRE	Inositol requiring enzyme
IRS	Insulin receptor substrate
IVCT	Isovolumetric contraction time
IVRT	Isovolumetric relaxation time
IκBα	nuclear factor of kappa light polypeptide gene enhancer in B-cells inhibitor, alpha
JNK	Janus kinase
KRAB	The Krüppel associated box
LAMP2A	Lysosome-associated membrane protein
LC3	Light chain 3
LC3-II	LC3-phosphatidylethanolamine conjugate
LCFA	Long-chain fatty acid
LD	Lipid droplet
LPL	Lipoprotein lipase
LTCCs	L-Type calcium channels
LV	Left ventricle
MCOLN1	Mucolipin 1
MG	Monoacylglycerol
MGL	Monoacylglycerol lipase
MHC	Myosin Heavy Chain
miR	Micro RNA
MiTF	Microphthalmia-associated transcription factor

MLC-2	Myosin Light Chain-2
mPTP	Mitochondrial permeability transition pore
MUFA	Monounsaturated fatty acid
MV	Mitral valve
MyBP-C	Myosin Binding Protein
NAFLD	Non-Alcoholic fatty liver disease
NCX	Sodium calcium exchanger
NRCM	Neonatal rat cardiomyocyte
Nrf2	Nuclear factor erythroid 2-related factors 2
OPOS	Impact of Obesity on Prospective Outcomes following cardiac Surgery
OXPHOS	Oxidative phosphorylation
PBS	Phosphate buffer saline
PCR	Polymerase chain reaction
PDAC	Pancreatic ductal adenocarcinoma
PDH	Pyruvate dehydrogenase
PDK1	Pyruvate dehydrogenase kinase 1
PLIN	Perilipin
PLN	Phospholamban
PPAR-α	Peroxisome proliferator-activated receptor-alpha
RISC	RNA-inducing silencing complex
ROS	Reactive oxygen species
RyRs	Ryanodine receptors
SAT	Subcutaneous adipose tissue
SDS	Sodium dodecyl sulfate
SERCA	Sarcoplasmic reticulum calcium ATPase
SL	Sarcomere length
SREBP-1	Sterol regulatory element-binding protein 1
SUnSET	Surface sensing of translation
T2D	Type 2 diabetes
TAG	Triacylglycerol
TBS	Tris-buffered saline
TCA	Tricarboxylic acid cycle
TFE3	Transcription Factor E3
TFEB	Transcription Factor EB
TFEC	Transcription Factor EC
TNT	Troponin-T
TRAF1	TNF receptor-associated Factor 1
UPP	Ubiquitin-proteasome pathway
UPR	Unfolded protein response
WAT	White adipose tissue
WHO	World Health Organization
WT	Wild type

ZDF	Zucker diabetic fatty
ZKSCAN3	Zinc finger with KRAB and SCAN domains 3

Acknowledgments

I want to express my sincere gratitude to my supervisor, Dr. Thomas Pulinilkunnil, for his invaluable guidance and unwavering support during my master's program. His laboratory has been an inspiring environment for scientific research, and I am truly thankful for the opportunity to conduct my research there. I would also like to thank Dr. Petra Kienesberger whose feedback and assistance have enhanced my research skills and capabilities. I extend my gratitude to Dr. Neale Ridgeway and Dr. Alexander Quinn for their participation on my thesis committee and for offering valuable feedback and suggestions. Their insights and guidance played a crucial role in shaping my research and the writing of this thesis.

I want to express my heartfelt appreciation to my lab colleagues in my study, Dr. Sundaram Pakkiriswami and Wai Naing. I am particularly grateful to Dr. Pakkiriswami for generously sharing his experiences and insights, which have proven invaluable to the success of my research and thesis. Your time and contribution have made a significant difference, and I sincerely thank you for your support. I extend my gratitude to my fellow researchers, both past and present, including Anu Jose, Angella Mercer, Dr. Logan Slade, Anastasia Dekic, and Gurpreet Kaur. Their presence and contributions have made working in the lab seamless and enjoyable. I am deeply grateful to Maggie Pickard for her tremendous moral support throughout my program here. Your support has meant much to me, and I truly appreciate it. Additionally, I extend my heartfelt thanks to Dr. Alli Murugesan and Dasse Rattina Nadaradjan for their words of encouragement and guidance, which have been instrumental professionally and personally.

Lastly, I must acknowledge my family's immense support and encouragement from afar during these two years. Your cheers and unwavering support have been indispensable, and I couldn't have accomplished this without all of you. Thank you for being my pillar of strength throughout this journey.

Finally, I want to extend my heartfelt gratitude to all those individuals whose names may not be listed here but have contributed in various ways to my academic growth and the successful completion of this thesis

Declaration:

The ideas conceived, experimental directions/protocols, and hypotheses presented in the current work were conceptualized by Adithi Pisapati under the mentorship of Dr. Thomas Pulinilkunnil. Unless otherwise stated, Adithi Pisapati designed and performed all experiments and analyzed results. Dr. Sundaram Pakkiriswami has contributed to the in-vivo data collection of results 3.8, 3.9, 3.12-3.15. Wai Naing and Angella Mercer have contributed to animal maintenance and data collection of results 3.8.

Chapter 1: Introduction

1.1 Obesity, insulin resistance, and cardiovascular disease.

Obesity results from diminished physical activity and the excessive intake of high-energy-yielding foods above an individual's needs. The Body Mass Index (BMI) utilizes an individual's height and weight for stratification into lean, overweight or obese class. If an individual's BMI falls between 15 and 19.9, they would be classified as underweight, while a BMI ranging from 20 to 24.9 would indicate a normal weight [1] Subjects with a BMI of 30-34.9 are categorized into class-1 obesity, those with a BMI of 35-39.9 into class-2, and finally all individuals with a BMI ≥40 into class-3 obesity [2]. According to the WHO, >2.1 billion adults globally were estimated to be overweight or obese in 2014, of which 1.5 billion were overweight, and 640 million were obese [3] [4] [5]. In Canada, one in four adults is obese, and between the years 2005 to 2018, the prevalence of obesity increased to 27.2% across all age groups and sexes [6].

White adipose tissue (WAT) is the most abundant adipose tissue in mammals, comprising subcutaneous adipose tissue (SAT; directly underneath the skin) and visceral adipose tissue (VAT; located within the abdominal cavity and thorax) [7]. In contrast, brown adipose tissue (BAT) represents a small proportion (0.2–3.0%) of total fat depots. Obesity is associated with an excess and/or dysfunction of SAT, particularly VAT depots. SAT forms 80% of the total fat mass and can expand more via cell hypertrophy and, to a lesser degree, via hyperplasia. The capacity of SAT expandability reaches saturation during obesity, leading to fat rerouting and transfer to VAT depots. VAT accounts for 5–20% of total body fat mass, which is mainly localized within the abdominal cavity but also includes epicardial (next to the heart, between the myocardium and visceral pericardium) and pericardial (external surface of the parietal pericardium) adipose tissue. When the lipid storage capacity of VAT is exceeded during obesity, lipid spillover occurs in several organs, such as skeletal muscle, liver, pancreas, and heart, given the proximity of VAT to these tissues [8]. Ectopic lipid accumulation triggers lipotoxicity, apoptosis, and inflammation. Chronic obesity leads to systemic inflammation, lipotoxicity, and cell death,

exacerbating insulin resistance (IR), precipitating beta cell dysfunction, and ultimately causing type 2 diabetes (T2D).

Obesity is strongly associated with poor quality of life, decreased productivity, increased unemployment, and escalating health care burden. Obesity triggers profound metabolic pathologies, manifesting as unfavorable chronic disorders. The chronic inflammatory state during obesity accelerates the progression to diabetes, including non-alcoholic fatty liver disease (NAFLD), retinopathy, cardiovascular disease (CVD), nephropathy, and underlying T2D comorbidities such as Alzheimer's disease, polycystic ovarian syndrome, gout, and rheumatoid arthritis. CVD accounts for more than two-thirds of mortalities linked with high BMI and ~ 66 million disability-adjusted life years [9] [10] [3]. Compared to normal weight individuals, young and middle-aged individuals with higher body weight show a 22% and 49% greater risk of all-cause mortality and CVD mortality, respectively [11]. CVD contributes to >75% of hospitalizations and >50% of deaths in obese and T2D. As of 2014, about 11% of heart failure in men and 14% in women is caused due to obesity-related outcomes, with CVD being the leading cause of mortality worldwide, with 32% of adults dying in the year 2019 [12] [13]. In Canada, 2.6 million adults over the age of 20 suffer from heart conditions and 14 die every hour [14]. CVD in obese individuals also contributes to 41% of BMI-related deaths and 34% of BMI-related disability-adjusted life years [15]. Given the disturbing trend of rising CVD in patients with obesity and T2D, a medically actionable model termed cardiometabolic-based chronic disease (CMBCD) was recently reconceptualized [16]. CMBCD model delineates inter-relationships among obesity, T2D, and CVD by presenting a framework focusing on three primary drivers (genetics, environment, and behavior) and 2 metabolic drivers (adiposity, and dysglycemia) with applications to 3 cardiovascular endpoints (coronary heart disease, heart failure, and atrial fibrillation) [16]. CMBCD modeling is in agreement with evidence from the Framingham heart study, which provided early evidence for obesity-related CVD that demonstrated an elevated risk of coronary disease, stroke, heart failure, and CVD death in obesity, independent of age, gender, smoking, cholesterol, or blood pressure [17] [18]. Long-term obesity is associated with left ventricular (LV) hypertrophy, cardiac fibrosis, and diastolic dysfunction that eventually evolves into overt heart failure [19]. During obesity, insulin resistance and metabolic dysfunction are sufficient to induce LV

structure/function disruptions in the heart, a pathology distinct from atherosclerosis and hypertensive heart damage or LV muscle-specific disease [10, 20, 21]. Cardiomyopathy manifested as LV enlargement and subclinical cardiac dysfunction in the absence of coronary artery disease, is a common cause of heart failure. For instance, elevated BMI in women of childbearing age increases the risk of dilated and hypertrophic cardiomyopathies [22]. Moreover, dilated cardiomyopathy and all-cause mortality is increased in overweight adults [23]. With moderately obese individuals showing structure function remodeling of the heart, it is evident that obesity is an independent risk factor for heart failure, and therefore, characterizing mechanisms of obesity-related metabolic cardiomyopathy should help guide clinical decisions to mitigate comorbidities and mortality associated with obesity.

1.2 Cardiac remodeling in health and obesity.

An initiating pathological event in the obese and diabetic heart includes impairment in cardiac energy remodeling, which has primarily been uncovered and extensively studied in preclinical models [24] and verified clinically [25, 26]. However, metabolic changes are underestimated in the clinical scenario due to the rapid metabolic transformation, underdiagnoses, and delayed detection in obese and diabetic humans exhibiting cardiomyopathy [27]. Cardiac metabolic remodeling is typically followed by impaired LV relaxation, collagen deposition, and dysregulation of Ca^{2+} homeostasis [28]. Therefore, it stands to reason that reversing altered cardiac substrate utilization or the detrimental effects of abnormal cardiac energy metabolism during obesity and diabetes will prevent cardiovascular complications. An in-depth understanding of how abnormalities in myocardial energy metabolism trigger disruptions in myocyte signaling and function in the heart during obesity is vital to treating obesity related heart disease.

1.2.1 Glucose and fatty acid utilization in a healthy heart.

Uninterrupted adenosine triphosphate (ATP) supply and utilization are critical for the viability and functioning of a healthy heart [29]. The heart consumes about 6 Kg of ATP per day and relies on multiple substrates such as fatty acids, carbohydrates, amino acids, and ketones [30] [31]. In a healthy heart, oxidation of long-chain fatty acids (LCFA) accounts for approximately 65–80% of ATP production; hence, they are the preferred

energy substrate for the heart [32]. Whereas glucose and lactate oxidation account for lower ATP production, representing 15–25% and 5–10%, respectively [33].

Fatty acid metabolism

Triacylglycerol (TAG) and free fatty acids (FA) are the two major sources of fatty acids that fuel the myocardium [33]. The heart receives FAs as FAs bound to albumin released from adipose tissue lipolysis or from intracellular TAG hydrolysis to FA. In the fed state, cardiomyocytes depend solely on the lipid substrates derived through the hydrolysis of circulating TAGs by lipoprotein lipase (LpL) [34]. Contractile function in the heart consumes ATP requiring substrates such as FA, which enters the cell through passive diffusion or fatty acid carriers/transporter. These carriers include two plasma membrane proteins, CD36/fatty acid translocase (FAT), fatty acid binding protein (FAB, Ppm), and two long chain acyl Co-A synthases – fatty acid transporter protein FATP1 and FATP6 [33]. Once inside the cardiomyocyte, long-chain fatty acyl-CoA synthase (ACSL1) converts FAs into fatty acyl-CoA esters in an ATP-dependent manner. The acyl group from fatty acyl-CoA is transferred from CoA to carnitine to form acylcarnitine by carnitine palmitoyl-transferase-1 (CPT-1), an enzyme residing in the outer mitochondrial membrane. Subsequently, CPT-2, an inner mitochondrial membrane enzyme, catalyzes the acyl group transfer from carnitine to CoA in the mitochondrial matrix. Within the mitochondrial matrix, fatty acyl-CoA molecules are sequentially broken down by β-oxidation to liberate acetyl-CoA, which is then metabolized through the tricarboxylic acid cycle (TCA) to generate ATP. FAs derived from TAG hydrolysis serve as energy substrates for forming complex lipids and plasma membrane biosynthesis. TAG hydrolysis represents a tightly regulated process involving the concerted action of adipose triglyceride lipase (ATGL), which generates DAG, hormone-sensitive lipase (HSL), which generates monoacylglycerol (MG), and monoacylglycerol lipase generates FA (MGL) [35].

Excess fatty acyl-CoA generates lipotoxic intermediates such as diacylglycerols, triacylglycerols, and glycerides [33]. Excessive accumulation of these lipotoxic intermediates drives insulin resistance, cell death, and contractile dysfunction. Lipid droplets (LD) which are intracellular vesicle-like structures, play a pivotal role in tightly regulating the balance between FA uptake and usage to avoid the accumulation of

detrimental lipid intermediates [36]. LD surface harbors different members of the lipid droplet-associating protein family, also known as the PAT family, including perilipins (PLINs), S3-12, and TIP47 [37]. The expression profile of the PAT family of proteins differs across tissues and their constitutive or differentiated organization on the LD surface [38, 39]. PLINS are the extensively characterized PAT family of proteins, controlling TAG hydrolysis and lipolysis.

Glucose utilization

Glucose uptake in the heart is mediated by glucose transporters termed GLUTs [40]. While there are 14 isoforms of GLUTs, GLUT 1 and GLUT 4 are major isoforms in the cardiac tissue [41]. GLUT 1 is an insulin-independent transporter present mainly in the erythrocytes and in the fetal heart, while GLUT 4, an insulin-sensitive transporter, is predominantly responsible for glucose uptake in the adult heart [42]. Glucose uptake through these transporters involves the translocation of GLUT 1 and GLUT4 to the sarcolemma. Insulin's binding to its transmembrane receptor initiates an intracellular autophosphorylation cascade that activates IRS-1 and promotes PI3K-phosphorylation of PIP2 to increase intracellular PIP3 concentrations. Increased PIP3 concentrations facilitate the recruitment of pyruvate dehydrogenase kinase 1 (PDK1) and protein kinase B (Akt) to the cardiomyocyte membrane, whereby PDK1 phosphorylates Akt. Subsequently, Akt inhibits AS160 and relieves inhibition of GLUT translocation. GLUT4 facilitates the transport of glucose through the cardiomyocyte sarcolemma. Insulin-induced GLUT4 translocation facilitates cellular glucose uptake and utilization [42].

Upon entry into the cardiac myocyte, glucose is phosphorylated by the enzyme hexokinase to glucose 6-phosphate that is either shunted into glycogen storage via glycogen synthase or processed further via the glycolytic pathway, hexosamine biosynthesis pathway (HBP), on pentose phosphate pathway (PPP) [40]. The glycolytic end-product pyruvate is transported into the mitochondrial matrix and converted by pyruvate dehydrogenase (PDH) to form acetyl-CoA, which is processed via the TCA cycle to generate ATP, two molecules of carbon dioxide, three NADH2, and one FADH2 [43]. In the anaerobic state or conditions of mitochondrial dysfunction, pyruvate is routed toward lactate production.

1.2.2 Metabolic remodeling in the obese heart.

"Obesity cardiomyopathy" encompasses morphological, functional, and metabolic abnormalities originating within the heart [44, 45]. In some cases, the term "metabolic cardiomyopathy" is used in reference to the broad setting of metabolic disorders, including insulin resistance, diabetes mellitus, and obesity. Chronic obesity is frequently associated with cardiomyopathy, and cardiac metabolism plays an important role in developing and progressing cardiomyopathic, metabolic, or lipotoxic heart failure. Obesity induces metabolic switching in the heart favoring FAO over glucose oxidation, which is initially adaptive although further dampen insulin sensitivity and metabolic flexibility over time, resulting in impaired cardiac efficiency and cardiac contractile anomalies [46]. Despite saturated FAO in the heart during obesity and diabetes, greater lipid accumulation is observed. Increased triglyceride accumulation and their products, such as ceramides and DAG, cause the majority of lipotoxicity in hearts. In obese Zucker Diabetic Fatty (ZDF) rats, intramyocardial lipid overload correlated with contractile dysfunction similar to that observed in human failing hearts with liposteatosis [47]. A comparable shift from relying on carbohydrates to adopting anaerobic free fatty acid metabolism occurs in cases of ischemia reperfusion injury. This leads to the generation of free radicals that trigger cardiomyocyte injury and cell death. Not only the amount of lipids but the type of lipid is equally important in governing functional outcomes in the heart during the early stages of obesity and during the progression to T2D. The heart generally prefers long-chain fatty acids such as palmitate and stearate among the saturated FA and oleate and elaidate among the unsaturated FA. Saturated FAs are lipotoxic, given their ability to induce myocyte apoptosis [48]. Monounsaturated fatty acid (MUFA) oleate, on the other hand, protects the heart against saturated fatty acid-induced lipotoxicity. Reduced cardiovascular issues and improved insulin sensitivity are linked to MUFA intake, which is highly enriched in olive oil [49]. This protective effect of oleate is most likely due to palmitate channeling into the intracellular pool of TAG, implying that different FA has distinct effects on cellular signaling and function.

Insulin being the central regulator of cardiac metabolism, disruptions in insulin signaling result in conditions such as hyperinsulinemia, insulin resistance during diabetes, and obesity [50]. In the heart, a high-fat diet-induced decrease in insulin-stimulated glucose

metabolism was observed much sooner when compared to skeletal muscle, adipose tissues, and liver [51], suggesting that obesity-induced cardiac dysfunction might be attributable to lipid overload inducing local insulin resistance and changes in cardiac metabolism rather than global systemic insulin resistance. Indeed, obesity interferes with insulin signaling via several mechanisms, including decreased tyrosine phosphorylation of IRS-1, increased serine/threonine phosphorylation, impaired AKT phosphorylation, and finally, altered GLUT-4 translocation to the sarcolemma [52]. Disruption in insulin signaling alters intracellular glucose and fatty acid (FA) flux compromising the heart's ability to partition nutrients for metabolism. This metabolic inflexibility leads to inefficient energy transfer from the oxidation of substrates to mechanical work [53]. Metabolic inflexibility in the obese and diabetic heart results in the underutilization of glucose and accumulation of FA metabolites, leading to glucotoxicity and lipotoxicity, which together is referred to as "glucolipotoxicity." Metabolic remodeling following "glucolipotoxicity" is manifested at the biochemical, structural, and functional levels in the cardiomyocyte and is hypothesized to be causative for inducing metabolic cardiomyopathy during the early stages of obesity.

1.3 Lipotoxicity and cardiomyocyte dysfunction.

1.3.1 Accumulation of lipid droplets and lipotoxic intermediates.

Metabolic remodeling in the heart during early obesity and diabetes culminates in adaptive molecular events to facilitate uninterrupted FA supply and oxidation. Augmented adipose tissue lipolysis and very low-density lipoprotein secretion from the liver significantly increase systemic FA and lipoprotein TAG, driving FA uptake by cardiomyocytes. Excessive FA in the heart, particularly TAGs, is stored in LD [54]. LDs are metabolically active intracellular organelles serving as the lipid reservoir that could be used for energy production and anabolism of membrane phospholipids [55]. The turnover of LD in the heart is regulated by important lipid droplet-associated proteins called perilipins, acyltransferases, and intracellular lipases [56]. The TGs present in these lipid structures are hydrolyzed by hormone-sensitive lipase (HSL) and adipocyte triglyceride lipase (ATGL) to liberate fatty acids, which may further be oxidized in the mitochondria [56]. Impaired LD degradation or increased LD turnover led to LD accumulation in the heart in patients with obesity and diabetes and the hearts of high-fat-fed rodents [57-59].

Fatty acid incorporation into the neutral lipid pool of LDs and controlled release of FA from LDs shield the heart from high acyl intermediate concentrations, which, when impaired, can interfere with contractile function and viability of the cardiomyocyte. Indeed, obesity is associated with enlarged sarcoplasmic reticulum, disordered alignment of myofilaments, abnormal morphology of mitochondria, and numerous lipid droplets between myofibrils in cardiac tissues [60]. Even though TAGs are most detectable, other metabolites, including diacylglycerols and ceramides, also contribute to lipid toxicity when their concentrations exceed normal physiological levels [61]. Accumulation of FA also enlarges the pool of intracellular FA metabolites, such as fatty-acyl-CoA, ceramides, DAGs, long-chain acyl CoAs, and/or acylcarnitine that are collectively referred to as "lipotoxic" intermediates [62]. Moreover, elevated intracellular FAs also activate transcription factor PPARα, which increases the transcription of genes involved in FAO, TAG biosynthesis, and hydrolysis and concomitantly inhibits glucose utilization [63] [64]. Notably, cardiomyocyte-specific PPARα overexpressing mice display mitochondrial ultrastructural abnormalities, lipotoxicity, and cardiac steatosis, causing systolic dysfunction and cardiomyopathy [63]. Moreover, DAG accumulation in the heart during obesity exacerbates cardiac insulin resistance by protein kinase C (PKCα)-dependent inhibitory phosphorylation of Akt and IRS-1 [65]. Not surprisingly, pharmacological and genetic strategies targeting lipotoxicity improve the metabolic health of the heart [66]. For example, in obese ZDF rats, troglitazone therapy lowers obesity-induced myocardial TAG and ceramide, ameliorating apoptosis and cardiac dysfunction [67]. Therefore these findings support the notion that the accumulation of intramyocellular FA and its lipotoxic metabolites is sufficient to cause cardiomyocyte apoptosis, cardiac fibrosis, and even myocardial remodeling [68]. Thus, learning the molecular underpinnings of lipotoxicity and its downstream effects on organelle function within the heart might offer novel avenues to mitigate metabolic cardiomyopathy in obesity and diabetes.

1.3.2 Mitochondrial dysfunction.

In addition to altered energy metabolism, increased FAO and metabolism during obesity and diabetes are linked to oxidative stress and mitochondrial dysfunction. It is estimated that ~80% of reactive oxygen species (ROS) are generated within the mitochondria of cardiomyocytes [69]. In well-coupled mitochondria, the electron flow rate

through the electron transport chain (ETC) is limited by the ATP turnover rate. Impaired electron transfer within the ETC facilitates electron leakage from the ETC complexes, forming ROS. Among the various acyl-CoA substrates, long-chain fatty acid substrates are primarily associated with the augmented generation of mitochondrial ROS. Despite mitochondria being the myocyte source of ROS during metabolic cardiomyopathy, mitochondria also suffer ROS-mediated damage [70]. ROS derived from excess FAO triggers mitochondrial uncoupling and oxidative damage to the mitochondria, impairing ATP production. Concerted action of mitochondrial enzymes such as glutathione, superoxide dismutase, and catalase neutralize ROS, keeping it at low levels within the myocyte. Accumulation of lipotoxic intermediate destabilizes ROS-neutralizing enzymes leading to ETC inactivation and mitochondrial dysfunction [70].

Emerging evidence also shows a decline in ETC complex activity, oxygen consumption, and mitochondrial DNA (mtDNA) content as plausible causes for mitochondrial dysfunction in cardiomyopathy. Oxidative damage to mtDNA also decreases mitochondrial protein content inactivating ETC and reducing ATP generation, which exacerbates mitochondrial ROS production accelerating mtDNA mutations to propel and amplify the cycle of mitochondrial damage [71]. Not only mtDNA but also lipids and proteins are impacted by excess ROS. Accumulation of lipotoxic intermediates within the internal mitochondrial membrane increases lipid peroxidation. For example, in obesity, oxidative modification of cardiolipin can impair mitochondrial membrane fluidity, reduce ETC activity, and induce mitochondrial permeability transition pore (mPTP) opening, disrupting mitochondrial function [72].

1.3.3 Calcium handling abnormalities.

Oxidative stress drives cardiac dysfunction during obesity by disrupting Ca^{2+} handling. During myocardial excitation-contraction coupling, cytoplasmic Ca^{2+} is taken up via voltage-sensitive LTCCs (L-type calcium channels) after sarcolemma depolarisation triggering Ca^{2+} release from the SR via ryanodine receptors (RyRs), a process commonly known as Ca^{2+} induced Ca^{2+} release [73]. During diastole, cardiac relaxation is driven by SR Ca^{2+}-ATPase (SERCA) mediated Ca^{2+} reuptake and Ca^{2+} extrusion from sarcolemmal Na^{+} and Ca^{2+} exchanger. High-fat diet-induced lipotoxicity in mice is associated with reduced phospholamban (PLN) phosphorylation contributing to diastolic dysfunction [74,

75]. Cardiac troponin (TNT) is a regulatory protein controlling the calcium-mediated interaction between myosin and actin [76]. In addition to PLN, TNT levels are reduced in high fat-fed mouse hearts [75]. PLN dephosphorylation at Thr17 and Ser16 residue inactivates SERCA2a, inhibiting Ca^{2+} uptake [77]. Furthermore, during cardiomyopathy, decreased content of Ca^{2+} transporters and Ca^{2+} transfer between mitochondria, ER, and SR leads to calcium mishandling, increasing action potential duration and diastolic relaxation time.

Increased ROS during lipotoxicity oxidatively modifies sulfhydryl groups of the cysteine residues within SERCA2a and RyR2, leading to their inactivation [78]. Oxidative modification of SERCA2a leads to prolonged Ca^{2+} transients and slower SERCA2a-mediated Ca^{2+} reuptake, similar to that observed in genetic models of obesity showing impaired ventricular relaxation [79]. Moreover, in murine genetic models of obesity and diabetes, aberrations in SR calcium handling and impaired mitochondrial calcium uptake are observed in isolated cardiomyocytes, as evident from a reduction in the rate of calcium decay [80]. The prevailing hypothesis is that calcium transfer from the cytosol to mitochondria represents a mechanism for coordinating ATP supply and demand for cardiomyocyte contraction. Mitochondrial calcium uptake functions as a spatial buffering system, removing calcium locally and modulating cytosolic calcium concentrations, thus regulating the activity of calcium-dependent processes. Appropriate Ca^{2+} handling is essential to mitochondria, where Ca^{2+} uptake supports oxidative phosphorylation (OXPHOS) and ATP production to limit excessive ROS production during cardiac contraction.

1.3.4 Endoplasmic reticulum stress.

The closer proximity and functional interaction of mitochondria and the ER dictates how ER gets impacted while adapting to mitochondrial dysfunction during obesity [81]. Dysregulation of glucose and fat metabolism triggers increases in ROS, which perturb ER homeostasis. ER is critical for protein quality control and biosynthesis of luminal and transmembrane proteins [82]. ER homeostasis is enabled through unfolded protein response (UPR), ER associated degradation (ERAD), and autophagy [83, 84]. Loss of ER function leads to an accumulation of misfolded or toxic proteins, a condition called ER

stress that acutely activates unfolded protein response (UPR) [83]. Activation of UPR involves three UPR sensors, including inositol-requiring enzyme 1α (IRE1 α), protein kinase R-like endoplasmic reticulum kinase (PERK), and activating transcription factor 6 (ATF6) on ER membrane, to clear misfolded or toxic protein accumulation [85]. During obesity, cardiac insulin resistance induces ER stress triggering proinflammatory events mediated by either IRE-1α/TRAF2/JNK1/c-Jun pathway or PERK/eIF2α/IκBα pathway and ATF6 [86, 87]. Data from our laboratory showed that DIO induces ER stress by activating CHOP/GADD153, facilitator of the ERAD pathway and executor of apoptotic cell death. Indeed, palmitate-induced lipotoxicity causes alteration in ER membrane phospholipids, resulting in ER swelling and compromising ER membrane structure and integrity. Moreover, the accumulation of saturated FFA- containing phospholipids increases ordering of the ER membrane, causing a loss in membrane fluidity and protein misfolding which inhibit SERCA2b activity and cause Ca^{2+} depletion [88].

Activation of ER stress is a homeostatic mechanism to clear misfolded proteins. However, ER stress activation is inadequate when the metabolic/lipotoxic stress is overwhelming. When the UPR cannot handle unfolded and/or misfolded proteins in the ER, ER-initiated apoptotic signaling is turned on. Impairment in the ER stress response pathway yields terminally misfolded proteins, which are degraded in the proteasome or lysosome to prevent facing the fate of cell demise by apoptosis [89] [90]. During mild to moderate metabolic stress, the proteasomal system is activated to degrade misfolded proteins, however, failure of the proteasome compensatorily activates lysosomal autophagy to maximize protein degradation and maintain proteostasis [89]. Disruption of lysosomal autophagy culminates in the accumulation of toxic protein aggregates, causing "proteotoxicity" and leading to cell death. A notable example of proteotoxicity in obese and diabetic individuals is the accumulation of circulating amylin protein, leading to amylin deposition in the heart. Accumulation of amylin oligomers leads to proteotoxic stress and apoptosis in multiple organs, including remodeling of cardiomyocyte structure and function, causing cardiomyopathy [91]. Therefore, the pathogenesis of cardiomyopathy observed during obesity and diabetes is likely an outcome of glucolipotoxicity induced proteotoxicity triggered by mitochondrial dysfunction, ROS overload, and ER stress. It is also plausible that changes in lysosome function impact the

mitochondrial, ER, and nuclear function of the cardiomyocyte in obesity, insulin resistance and diabetes. However, limited studies have examined the molecular mechanisms by which glucolipotoxicity impacts inter-and intra-lysosomal signaling events.

1.3.5 Lysosomal function in health and disease.

Proteostasis is crucial in maintaining protein quality control and efficient cardiomyocyte structure and function [92]. The ubiquitin-proteasome pathway (UPP) degrades damaged, misfolded and short-lived cellular proteins in the cardiomyocyte [93]. Contrastingly, extracellular proteins such as those on the organelle membrane undergo degradation via lysosome-mediated autophagy [93]. An impairment in protein degradation, either due to organelle dysfunction or aggregation of misfolded proteins caused by an imbalance between synthesis and degradation, could lead to proteotoxic stress and cardiomyocyte cell death [94]. Glucolipotoxicity induced by obesity disrupts protein quality control and induces ER stress leading to the activation of the UPP pathway [95]. However, chronic obesity or sustained glucolipotoxic milieu in the heart saturates and impairs this form of protein degradation leading to the toxic aggregation of misfolded and damaged proteins [96]. Supporting evidence has revealed the presence of a significant accumulation of non-degraded proteins in failing hearts from chronically obese humans with type 2 diabetes, suggesting that dysfunctional proteasomal degradation causes a maladaptive buildup of cytotoxic proteins leading to cardiomyopathy [97]. Cargo degradation by lysosomes is carried out either via macroautophagy or chaperone-mediated autophagy. Macroautophagy is a catabolic mechanism wherein double- or multi-membrane structures called autophagosomes engulf cargo such as proteins and organelles and fuse with the lysosome for ensuing cargo degradation [98]. Autophagy-related (Atg) proteins organize and control various steps of macroautophagy [99, 100] with inputs from microtubule-associated protein 1A/1B-light chain 3 (LC3) [101]. The autophagosomes then engulf cytoplasmic elements, such as cytosolic proteins and organelles, for degradation. During this, LC3-phosphatidylethanolamine conjugate (LC3-II), which is recruited to the autophagosomal membranes, is formed when a cytosolic form of LC3 (LC3-I) combines with phosphatidylethanolamine [101]. Lysosomal enzymes break down components within autophagosomes as they merge with lysosomes, forming

autolysosomes. This leads to the degradation of LC3-II within the autolysosomal interior. As a result, starvation-induced autophagic activity is reflected in the lysosomal turnover of the autophagosomal marker LC3-II, [100] a readout for the autophagic flux that refers to the dynamic kinetics of autophagosome production and clearance by lysosomes. In the hearts of mice and humans with obesity and diabetes, altered autophagic flux is associated with defects in eliciting the formation of LC3-II from LC3-1 [102-105]. Our laboratory has previously demonstrated significant suppression of autophagic flux in the hearts of diet-induced obese mice and H9C2 cells, neonatal rat cardiomyocytes (NRCM), and adult rat cardiomyocytes (ARCM) subjected to palmitate-induced lipotoxicity [105].

In contrast to macroautophagy, chaperone mediate autophagy (CMA) recognizes a single soluble protein with the help of cytoplasmic heat shock-associated protein (Hsc70) and targets it to the lysosome through a lysosome-associated membrane protein (LAMP2A) [106]. Indeed, lysosomal homeostasis is perturbed during loss of function mutations of cytosolic chaperones, Hsc70 and Hsp90 and lysosomal CMA receptor, LAMP2A. Notably, the heart of patients with Danon's disease carries a mutation in the gene that encodes for LAMP2, resulting in the toxic accumulation of autophagic vacuoles and cardiomyopathy [107, 108]. Data from our laboratory showed decreased expression of lysosomal proteins (Hsc70, Hsp90, LAMP2A), lysosomal content, and lysosomal hydrolase activity in type-1 diabetes, diet-induced obesity, and cardiomyocytes subjected ex vivo to glucolipotoxicity. Moreover, H9C2 and NRCM cells treated with saturated fatty acid palmitate (but not oleate) displayed loss of lysosomal content and proteolysis, suggesting the detrimental effect of lipotoxic species on lysosomal integrity and function.

Notably, lysosomal autophagy and function are transcriptionally regulated by transcription factors, including FOXO3, nuclear factor erythroid 2-related factor 2 (Nrf2), hypoxia-inducible factor-1α (HIF-1α), p53, and most recently characterized ZKSCAN3 and MiTF family of transcription factors. ZKSCAN3 is a zinc-finger transcription factor family member with KRAB and SCAN domains [109] that negatively regulates lysosomal biogenesis and function, thereby repressing autophagy. On the other hand, during starvation, ZKSCAN accumulation leads to inactivation, thus promoting autophagic degradation [109]. The MiTF family of transcription factors promotes the expression of

autophagy-related genes in response to various stimuli, including starvation, lysosomal stress, and mitochondrial dysfunction [110].

1.4 Transcription factor EB and MiTF-family.

TFEB is a member of the micropthalmia-associated transcription factor superfamily (MiTF), including MiTF, TFE3 and TFEC [111]. TFEB is a basic helix-loop-helix transcription factor with E-box binding elements [112]. Three critically important regions are shared by all MiTF/TFE proteins, which are the DNA-binding motif, the basic helix loop helix structure, and leucine zipper motifs (bHLHZip), and which are important for protein interaction and dimerization. The microphthalmia family members heterodimerize with each other to trigger the expression of genes that regulate lysosomal biogenesis and autophagy [113]. Sardiello et al. characterized a coordinated lysosomal expression and regulation (CLEAR) network in lysosomal gene promoters, which, when bound by MITF proteins, trigger expression of genes encoding lysosomal acidification and degradation, biogenesis, exo-, endo-, and phagocytosis [110, 114, 115]. CLEAR promoter elements are repetitions of ten base pair motifs (GTCACGTGAC) located within the first 200 base pair of numerous lysosomal genes. Notably, CLEAR elements form a type of E Box (CANNTG), recognized robustly by TFEB and/or other bHLH/LZ family members. Transcription factor EB (TFEB) is a master transcriptional regulator of proteins involved in autophagosomal assembly, autophagosomal maturation, autophagosome-lysosome fusion, and lysosomal biogenesis and function [116]. However, TFEB was not fully described until 2009 when Sardiello et al. elegantly characterized TFEB's ability and capacity to regulate cellular degradation processes, particularly those involving autophagy and lysosomal proteolysis.

1.4.1 Regulation of TFEB signalling and function in the heart.

The activity of TFEB is nutritionally regulated. During the fed state, inhibition of protein degradation prevents amino acid utilization leading to lysosomal retention of amino acids [117-119]. Elevation of lysosome amino acid content recruits mammalian targets of rapamycin (mTOR) and extracellular receptor kinase (ERK) on the lysosomal membrane to phosphorylate and inactivate TFEB, thus inhibiting autophagy [120]. Moreover, lysosomal membrane proteins such as Rag A/B, Rag C/D, vATPase, lysosome Na ATP,

Ragulator, mTOR, and DEPTOR sense intralysosomal nutrient and amino acid content [121]. TFEB is phosphorylated by mTOR-mediated Ser211 phosphorylation or ERK2-mediated Ser142 phosphorylation, leading to its cytosolic retention. Phosphorylation of TFEB leads to a conformational change in TFEB, enabling its binding to 14-3-3, a cytosolic adapter protein [122]. 14-3-3 masks the nuclear localization sequence of TFEB, thus preventing nuclear translocation of TFEB and activating transcription of CLEAR and autophagy genes (LC3, p62, cathepsin, beclin). However, in the fasted state, cells utilize endogenous energy stores such as glucose, lipids, and proteins by autophagy. During fasting, translocation of TFEB into the nucleus activates genes that induce autophagy to promote lysosomal nutrient degradation. TFEB-signaling not only generates more autophagosomes but also accelerates their delivery to lysosomes by increasing lysosomal number, thereby facilitating protein degradation [123]. Protein degradation depletes amino acid content within the lysosome. However, mTOR dissociation from the lysosome during fasting releases Ca^{2+} from the lysosomal lumen through mucolipin 1 (MCOLN1), which promotes calcineurin-mediated TFEB dephosphorylation and entry into the nucleus to induce transcription of CLEAR network genes [124]. Indeed, lysosomal dysfunction during ischemia and lipid loading is associated with abnormalities in TFEB phosphorylation, localization, and function. Our data demonstrate that following type 1 diabetes and diet-induced obesity, inactivating phosphorylation of TFEB is augmented with a concomitant decline in nuclear TFEB [105].

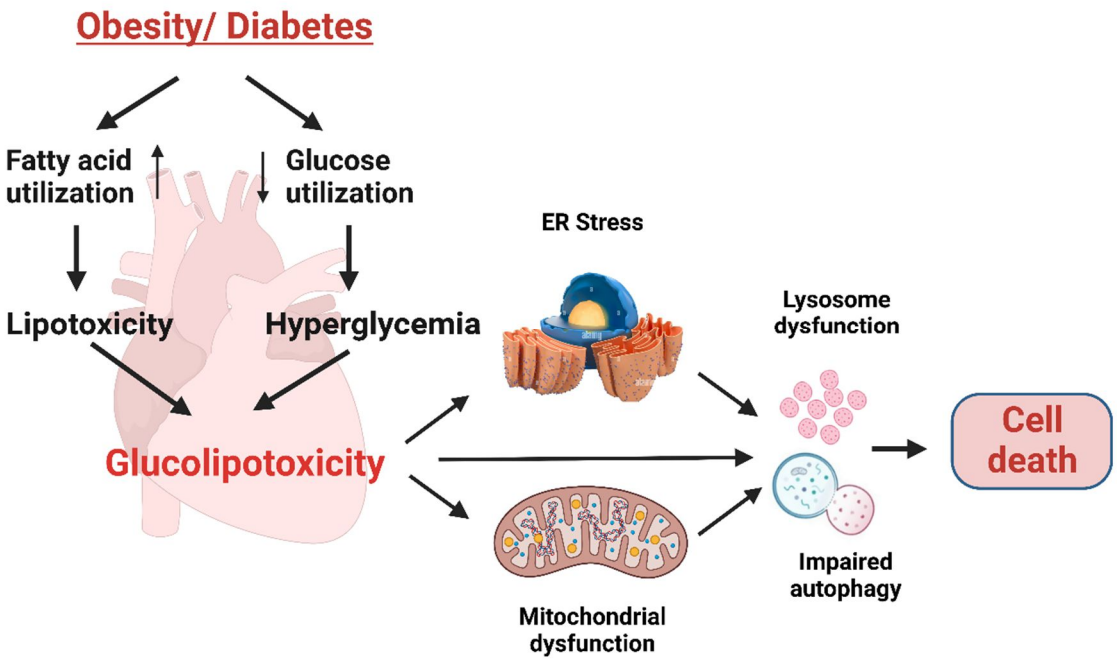

Figure 1.1 Glucolipotoxicity in the heart leads to impaired organelle function and cardiomyocyte death

Obesity and diabetes cause increased fatty acid utilization leading to lipotoxicity and decreased glucose utilization in the heart. Together, these conditions lead to glucolipotoxicity, which, in turn, induces endoplasmic reticulum stress and mitochondrial dysfunction, ultimately resulting in cell death. Previous research conducted in our laboratory has demonstrated that glucolipotoxicity directly causes lysosomal dysfunction and impaired autophagy, preceding cardiac cell death and contributing to heart failure.

What is not known is the molecular mechanism by which "glucolipotoxicity" in the obese and diabetic heart decreases TFEB content [105]. In addition, the turnover rate of TFEB in the heart is currently unknown, and whether protein content is regulated by lysosomal or proteasomal degradation remains to be ascertained. Beyond phosphorylation, TFEB is modified by acetylation, SUMOylation, PARsylation, glycosylation, and cysteine oxidation [125]. The presence of many post-translational modifications of TFEB highlights the importance of these modifications for cellular fate. Furthermore, TFEB is regulated in multimodal ways, including transcriptional rate, post-transcriptional regulation, and post-translational modifications. Post-transcriptional regulation is, in part, mediated by miRNAs [126]. A myriad of miRNAs recognize the TFEB transcript or regulate its function by targeting accessory molecules or enzymes involved in its post-translational modifications. Moreover, TFEB-responsive transcriptional programs are plausibly influenced by the miRNA-mediated regulation of TFEB targets.

1.4 Micro-RNA and its regulatory control of TFEB.

MiRNA or microRNAs are the class of non-coding RNAs that induce post-translational modifications of about 60% of the protein-coding genes [127]. miRNAs are ~22 nucleotide-long molecules primarily processed from introns by forming random hairpins and are often regulated by their promoters [128]. miRNA generation involves a two-step process that begins with forming a primary miRNA in the non-coding sections of DNA [127]. Alternatively, miRNAs can also be generated by duplicating existing miRNAs. DROSHA, belonging to the class III family of RNases, cleaves the above-formed primary miRNA to generate the precursor miRNA, otherwise known as pre-miRNA [129]. Another double-stranded RNA-binding protein, DiGeorge Syndrome Critical Region 8 (DGCR8), interacts with DROSHA to carry out the critical step of pre-miRNA formation [129]. These intermediates are transported out of the nucleus by Exportin 5, forming a miRNA duplex with DICER, another class III ribonuclease. Further, the duplex attaches itself to the RNA-inducing silencing complex (RISC), which uses the miRNA as a template to recognize the complementary mRNA for degradation. The argonaute proteins present in this RISC complex are responsible for the silencing action of miRNA [130]. The interaction of the single-stranded, mature miRNA with the 3'untranslated regions of the target gene to bring about degradation depends on multiple factors, such as the abundance

or availability of miRNA, their subcellular location, and the affinity of miRNA-mRNA interactions (see Figure 1.2) [131]. Notably, miRNA-128 induces TFEB mRNA degradation in HeLa cells, concomitantly declining several lysosomal CLEAR genes [123]. A role for miRNA-29 in regulating autophagy and TFEB has also been shown in choroid/retinal pigment epithelial cells, where miRNA-29 overexpression leads to reduced cytosolic TFEB protein [132]. Similarly, miRNA-30b-5p inhibits lysosomal biogenesis by downregulating TFEB expression in HEK293 cells [133]. In pancreatic ductal adenocarcinoma (PDAC) cell lines decreases in miRNA-29 is associated with the upregulation of autophagy and protein content of TFEB and ATG9A, which is a transmembrane protein that supports the formation of autophagosomes. Moreover, in myocardial infarction, miRNA-330-3p was found to be downregulated simultaneously with an upregulation of TFEB [134]. While the direct effect of miRNA on TFEB stability and content have been evaluated, whether miRNA degrades TFEB in the heart during lipotoxicity is still unknown. Since TFEB is indispensable for lysosomal function, characterizing miRNA that inhibits TFEB in the cardiomyocyte would lead to a druggable target for obesity and diabetes-related cardiomyopathy.

An indirect effect of miRNA on TFEB-mediated lysosomal autophagy is through regulating the steps in the mTOR pathway [135]. Some miRNAs directly target mTOR, while others control its expression by focusing on proteins involved in the signaling cascade. miR-7, miR-17-5p, miR-30a/b/c, miR-96, miR-99, and miR-100 are a few among the 16 miRNA that target various aspects of mTOR signaling and function across varied tissues [136]. TFEB and ATG9 are important targets of miR-29, often downregulated in cancerous environments [137].

Considering the heart, a few miRNAs have been shown to regulate TFEB expression in multiple ways. The miRNA-132/212 family promotes cardiac hypertrophy and autophagy in cardiomyocytes, and conversely, mice lacking miRNA-132/212 are protected from pressure overload-induced heart failure [138]. This family of miRNA also regulates lipid metabolism by targeting Fitm2, the fat storage-inducing transmembrane protein 2 genes. Additional targets of the 132/212 miRNA cluster include FOXO3, which can reduce ROS production and enhance autophagy [139].

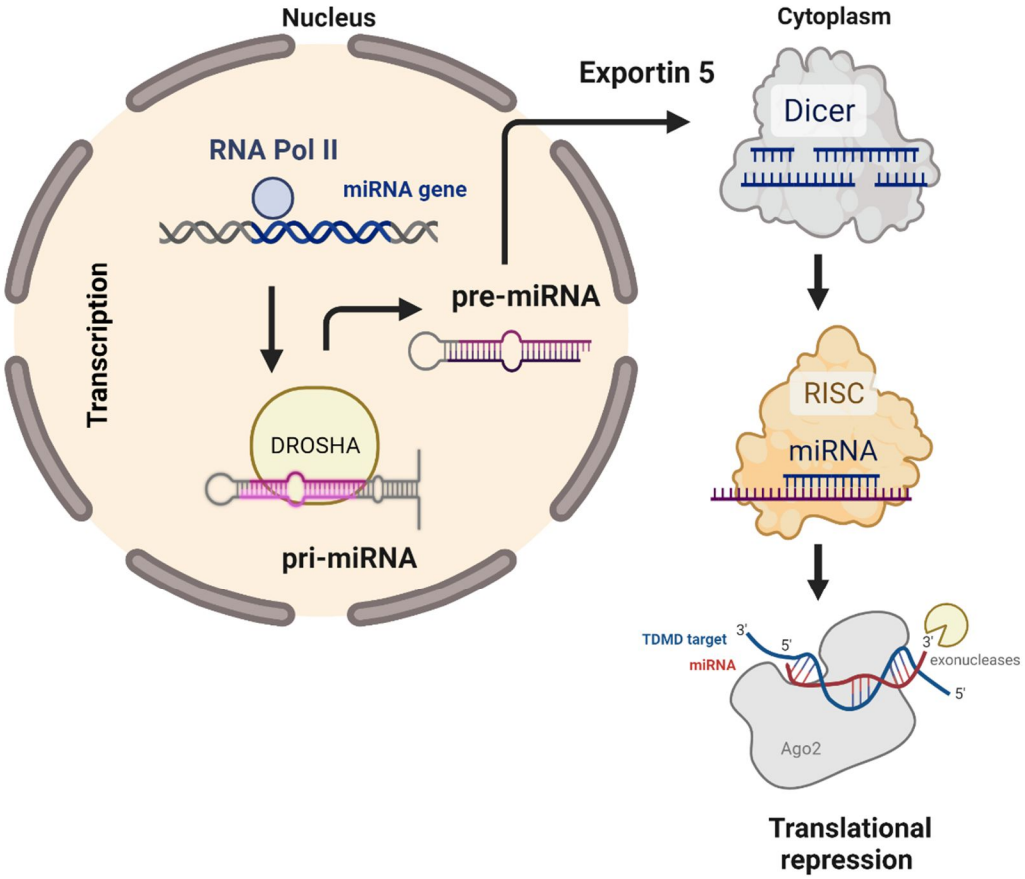

Figure 1.2 miRNA biogenesis and mode of action

The biogenesis of miRNA commences with synthesizing the primary miRNA transcript (pri-miRNA). This pri-miRNA is then cleaved by the microprocessor complex, consisting of Drosha and DiGeorge Syndrome Critical Region 8 (DGCR8), forming the precursor miRNA (pre-miRNA). The pre-miRNA is subsequently transported to the cytoplasm in an Exportin5/RanGTP-dependent manner, where it undergoes further processing to produce the mature miRNA duplex. Finally, one of the strands, either the 5p or 3p strand, of the mature miRNA duplex, is incorporated into the Argonaute (AGO) protein family, forming a miRNA-induced silencing complex (miRISC).

1.6 Effect of TFEB on systemic metabolism, cardiac energetics, and contractile function

Data from our laboratory and others have now clarified that TFEB exerts a non-canonical role in altering cellular metabolism in addition to its canonical role in promoting lysosome-mediated autophagy and cellular survival. Palmitate potentiates inhibitory phosphorylation of TFEB, thus barring TFEB from entering the nucleus to activate CLEAR

genes and lysosomal autophagy. Supporting evidence on TFEB's role in cardiac lipid metabolism was revealed by an assessment of the transcriptome of cardiomyocyte-specific TFEB-/- mice, which demonstrated that genes linked to lipid biosynthesis and storage were upregulated, whereas genes governing lipid catabolism were downregulated [140]. In addition to decreased FAO, oleate treatment induced increased lipid droplet accumulation and enlarged lipid droplet size in cardiomyocytes from mice with $TFEB^{fl/fl\ CRE-/-}$ deletion when compared to the WT cardiomyocytes [140]; these data suggest that TFEB regulates lipid metabolism in the cardiomyocyte by governing FA storage and catabolism.

Furthermore, $TFEB^{fl/fl\ CRE-/-}$ cardiomyocytes showed an upregulation of genes involved in the cycling of Ca^{2+} in the heart, including Ca^{2+} channel genes (Cacna1 and Cacnb1), Na+/Ca^{2+} exchanger (NCX) channels (Slc8a2), and SR Ca^{2+} ATPase pump 1 (Atp2a1) [140]. It is unknown if TFEB directly regulates calcium handling in the cardiomyocyte. Moreover, if lipotoxicity-induced dysregulation of calcium handling during obesity involves TFEB remains undetermined. However, the mechanisms by which lipotoxicity induces loss of TFEB content and function and whether this decline in TFEB action remodels lipid metabolism and calcium handling, exacerbating cardiomyopathic dysfunction in diet-induced obesity, remains undetermined. Unravelling these mechanisms could boost utility of TFEB activators to treat obesity-related cardiomyopathy.

1.7 Summary leading to rationale.

Obesity, insulin resistance, and diabetes play significant roles in cardiovascular disease (CVD)-related hospitalizations (>75%) and deaths (>50%) [141]. Among the various CVD observed in obese and diabetic individuals, left ventricular muscle myopathy or cardiomyopathy is becoming increasingly prevalent. Prior to the onset of cardiomyopathy, abnormalities in cardiomyocyte lipid metabolism and lysosomal autophagy have been observed [50]. Our laboratory has shown that in the obese and diabetic heart, an overload of lipid (specifically palmitate) leads to a decrease and inactivation of bHLH-leucine zipper transcription factor EB (TFEB), a crucial regulator of lysosomal biogenesis and autophagy, thereby inducing cardiomyopathy [105]. Nevertheless, the exact mechanism(s) through which palmitate reduces myocyte TFEB content and function has yet to be determined. Gene and protein expression is controlled within the cell by activating miRNAs, which act

as endogenous regulators of target mRNA. Hence, I hypothesized that lipotoxicity following diet-induced obesity upregulates posttranscriptional and posttranslational mechanisms of TFEB degradation leading to disruptions in energy metabolism, calcium handling, insulin action, and cardiac function. To address this hypothesis, I will execute the following aims in my thesis:

1. Determine whether palmitate promotes the expression of miRNA (miR-29,30,132/212) targeting TFEB (Figure 1.3).
2. Examine the effect of palmitate on the protein turnover of TFEB in H9C2 cells.
3. Investigate the impact of cardiomyocyte-specific TFEB loss of function on cardiac function and energy metabolism in diet-induced obesity (Figure 1.4).

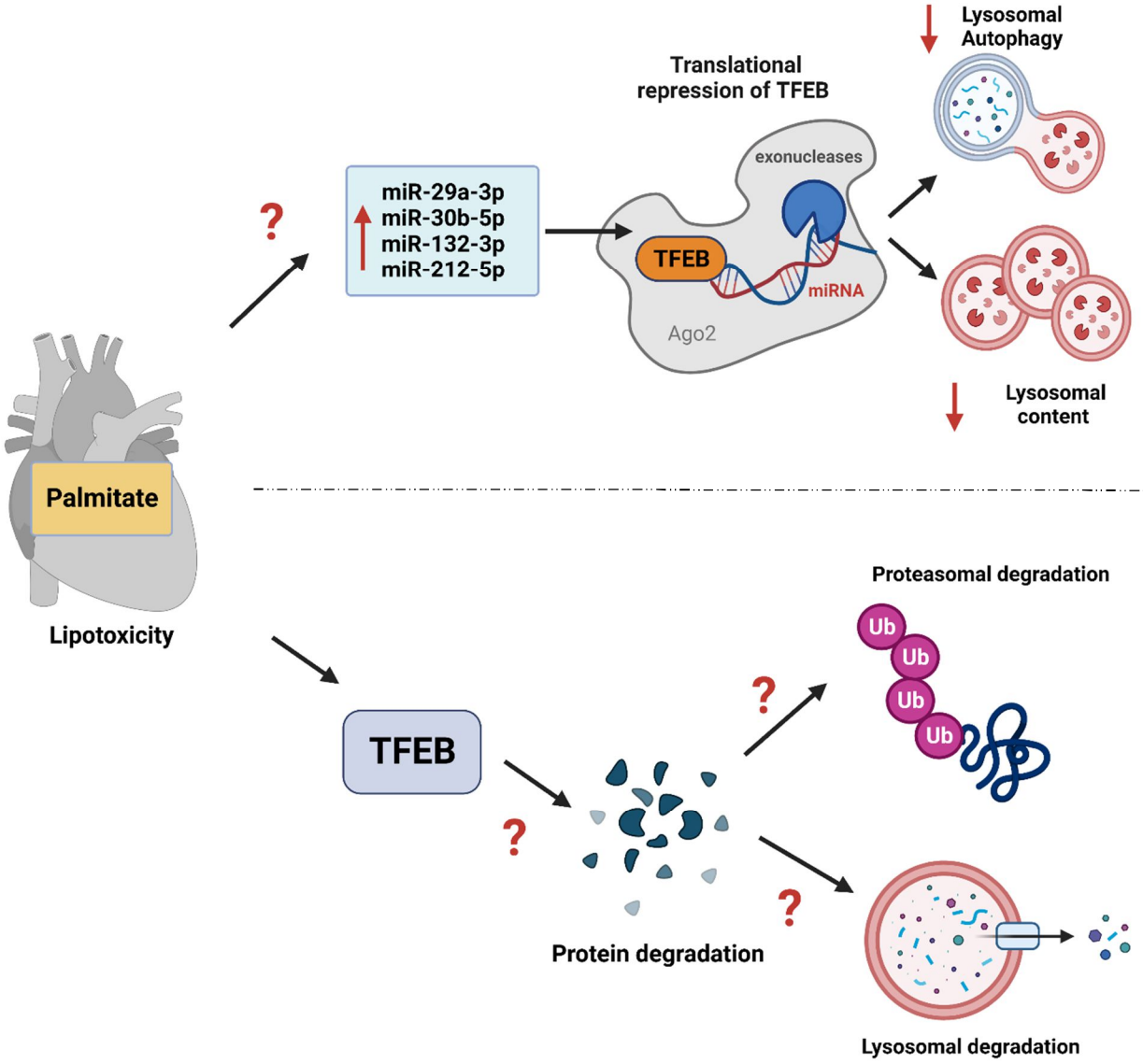

Figure 1.3 Possible mechanisms of palmitate-induced TFEB degradation.

A hypothetical model of palmitate-induced reduction in TFEB content within the heart by elevating miRNAs targeting TFEB and/or accelerating the degradation of TFEB protein by proteasomal or lysosomal degradation pathways.

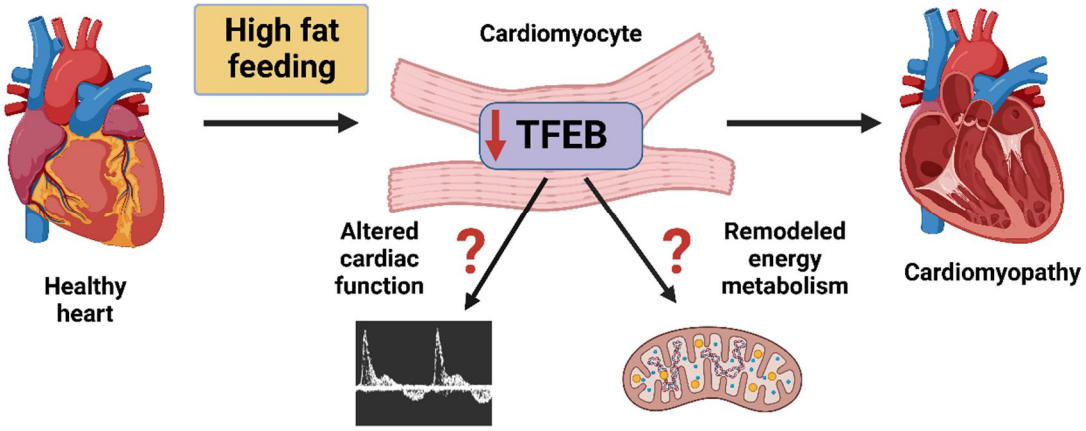

Figure 1.4 Examining the role of cardiomyocyte-specific TFEB deletion on energy metabolism and cardiac function during diet-induced obesity.

Chapter 2: Experimental Methods.

2.1 Animal models.

All protocols involving rodents were approved by the Dalhousie University Institutional Animal Care and Use Committee (Protocol # 18-116).

2.1.1 Generation of constitutive cardiomyocyte-specific TFEB$^{-/-}$ mice.

Mice carrying TFEB-floxed alleles (TFEB$^{fl/fl}$, Stock # 400102) were provided by Dr. Andrea Ballabio to be crossed with transgenic mice expressing Cre driven by myosin heavy chain promoter (MHC-Cre, Stock: 009074) to produce cardiomyocyte-specific Tcfeb knockout (TFEB $^{fl/fl\ Cre/-}$) mice. Genomic DNA isolated from TFEB $^{fl/fl\ Cre/-}$ and MHC-Cre mice was subjected to PCR analysis using specific primers (see Table 3). Male and female mice on a C57BL/6J background strain were used in this study. Experimental control for TFEB$^{fl/fl\ Cre/-}$ mice was TFEB$^{fl/fl\ -/-}$ mice that did not carry MHC-Cre transgene.

2.1.2 Generating diet-induced obese models of TFEB $^{fl/fl\ -/-}$ and TFEB $^{fl/fl\ CRE/-}$ mice.

Nine to ten weeks mice (TFEB$^{fl/fl\ -/-}$ and TFEB$^{fl/fl\ Cre/-}$) were assigned at random to cohorts fed with high fat (60% kcal fat; Research Diets 12492) or low fat (10% kcal fat; Research Diets D12450J) for 20 weeks (see Figure 2.1). Body weight gain was recorded once every 4 weeks by calculating the difference in body weight before starting the diet and every 4 weeks after starting the diet. At week 20, the mice were fasted for 16 hrs prior to euthanasia to eliminate the confounding influence of variability in circulating substrates and hormones. Adult mouse cardiomyocytes were isolated from aerobically perfused hearts, and other tissues were collected and stored at - 80°C for future analysis.

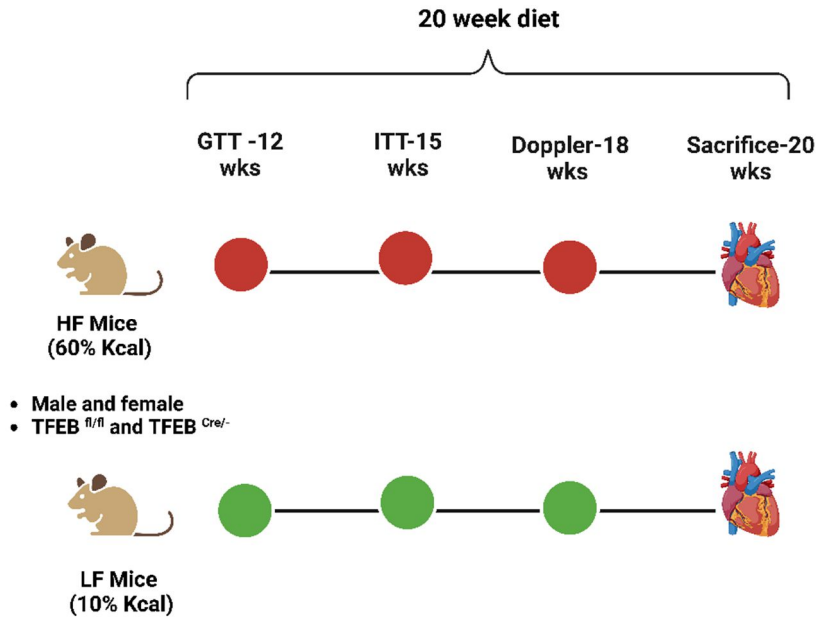

Figure 2.1 Generating diet-induced obese models of TFEB$^{fl/fl\ -/-}$ and TFEB$^{fl/fl\ CRE/-}$ mice. Male and female TFEB$^{fl/fl\ -/-}$ and TFEB$^{fl/fl\ CRE/-}$ mice were randomly assigned high or low-fat for 20 weeks. Weights were recorded once every 4 weeks, glucose tolerance test was performed at 12 weeks, insulin tolerance test at 15 weeks, and tissue Doppler analysis at 18 weeks. The animals were finally euthanized at week 20 and hearts were used for either tissue processing or isolation of cardiomyocytes.

2.1.3 Glucose tolerance test.

Glucose tolerance was assessed in 16 hrs fasted non-anesthetized mice following intraperitoneal (i.p.) administration of 20% D-glucose in saline at 2g/kg body weight. Blood glucose was measured at 0, 15, 30, 60, and 120 min after glucose administration using Accu-Check Aviva glucometers (Roche, Basel, CH).

2.1.4 Insulin tolerance test.

Systemic insulin tolerance was assessed following 5 hrs of food withdrawal to eliminate the confounding influence of variability in circulating substrates and hormones. Non-anesthetized mice were injected intraperitoneally (i.p.) with human insulin (00586714; Humulin R, Eli Lilly) at 0.8 units/kg body weight. Blood glucose was measured at 0, 15, 30, 60, and 120 min after insulin administration using Accu-Check Aviva glucometers (Roche, Basel, CH).

2.1.5 Pulse Wave Doppler analysis.

Cardiac function was analyzed in low and high-fat-fed $TFEB^{fl/fl\ -/-}$ and $TFEB^{fl/fl\ Cre/-}$ mice during weeks 18-19 of the diet period. The mice were anesthetized using a cocktail of isoflurane and oxygen inhalation (1L of oxygen maintained on 2% of isoflurane). When the mice were sufficiently anesthetized, as determined by the absence of response to firm tail pressure, mice were placed supine on a warmed (37 °C) monitoring mat (Indus Instruments Rodent Surgical Monitor), where heart rate (HR) and electrocardiogram (ECG) readings were continuously monitored.

A 10 MHz Doppler probe (Indus Instruments Doppler Flow Velocity System, made by Indus Instruments 721 Tristar Drive Webster, Texas, 77598, USA) was focused on either the aortic valve (AV) or the mitral valve (MV). For analysis, pulse wave Doppler sonograms of blood flow through the chosen valve were captured. All measurements were based on an average of three consecutive cardiac cycles. The aortic doppler ultrasonography is a readout for left ventricular systolic function, while the mitral doppler sonogram denotes left ventricular diastolic function [142] [143].

2.1.6 Sarcomere length measurement

Adult mouse cardiomyocytes (AMCM) were isolated, as described in section 2.2.1. Sarcomere length was measured using a cell shortening analysis system from HORIBA. Inc. Briefly, cells were mounted in the stage of an inverted microscope with a buffer

containing: 131 mM NaCl, 4 mM KCl, 1 mM $CaCl_2$, 1 mM $MgCl_2$, 10 mM glucose, 10 mM HEPES, at pH 7.4. The cells were field stimulated with a suprathreshold voltage at a frequency of 0.5, 1, 1.5 and 2 Hz for 30 sec durations, using a pair of platinum wires placed on the side of the chamber connected to a Myopacer (Myopacer Field Stimulator, Ion Optix). The myocyte being studied was displayed on the computer monitor using a Grabber camera (ZEISS microscope). The amplitude and velocity of contraction and relaxation is recorded with good fidelity. The FelixGX software was used to capture changes in cell length during contraction and relaxation. Cardiomyocyte contraction and relaxation were assessed using the following indices: Min represents contraction (shortening), Max represents relaxation (relengthening), and SL represents sarcomere length. Min SL (peak shortening), which indicates sarcomere length during peak ventricular contraction; Max SL (peak relengthening) indicates sarcomere length during peak ventricular relaxation; ΔSL, which indicates a change in sarcomere length from the peak of contraction to the peak of relaxation; ΔSL (%) which indicates % change in sarcomere length from peak ventricular contraction to peak relaxation; -dSL/dtmin and +dSL/dtmax indicates the maximum rate of contraction and relaxation, respectively; Time to Min SL indicates time to reach peak ventricular contraction and Time to Max SL indicates time to reach ventricular relaxation. After altering stimulus frequency (from 0.5 - 2 Hz), the steady-state contraction of myocyte was achieved (after the first five to six beats) before sarcomere length was recorded. Myocytes with obvious sarcolemmal blebs or spontaneous contractions were excluded from mechanical recording. All measurements were performed at 25–27℃. Sarcomere length was analyzed using Matlab software.

2.1.7 Intracellular Ca^{2+} transient measurement.

Both intracellular Ca^{2+} and sarcomere length were measured simultaneously in the same set of myocytes. Myocytes were loaded with Fura-2AM (1 mM) for 15 min at room temperature in the dark, and fluorescence measurements were recorded with a dual-excitation fluorescence photomultiplier system. In brief, coverslips containing AMCMs were placed on a ZEISS inverted microscope with a temperature-controlled Warner chamber and imaged through a Fluor640 oil objective. Myocytes were exposed to light emitted by a 75W lamp and passed through a 360 or a 380 nm filter while electrically paced at 0.5, 1, 1.5 and 2 Hz. Fluorescence emissions were detected between 480–520 nm by a

photomultiplier tube after alternating illumination of the cardiomyocytes with 360 nm and 380 nm for 30 sec. The qualitative changes in intracellular Ca^{2+} ($[Ca^{2+}]_i$) concentration were inferred from the ratio of the fluorescence intensity at the two wavelengths (360/380). Intracellular ($[Ca^{2+}]_i$) was measured using the following indices: $[Ca^{2+}]_{imin}$ indicates $[Ca^{2+}]_i$ during cellular relaxation; $[Ca^{2+}]_{imax}$ indicates $[Ca^{2+}]_i$ during cellular contraction; $\Delta[Ca^{2+}]_i$ indicates Ca^{2+} transient amplitude (change in intracellular Ca^{2+} from the peak of relaxation to peak of contraction); $+dCa/dt_{max}$ indicates the maximum rate of Ca^{2+} transient; $-dCa/dt_{min}$ indicates maximum rate of Ca^{2+} removal, 50% Ca^{2+} Tau and 80% Ca^{2+} Tau indicate time constant to 50% and 80% Ca^{2+} decay.

2.2 Cell culture experiments.

2.2.1 Adult mouse cardiomyocyte isolation.

Adult mouse cardiomyocytes (AMCMs) were isolated from TFEB $^{fl/fl\ -/-}$ and TFEB $^{fl/fl\ CRE/-}$ mice that were fasted for 16 hours prior to decapitation. Isolated hearts were perfused retrogradely by the non-circulating Langendorff method using the perfusion buffer (113 mM NaCl, 4.7 mM KCl, 0.6 mM KH_2PO4, 0.6 mM Na_2HPO4, 1.2 mM $MgSO_4.7H2O$, 12 mM $NaHCO_3$, 10 mM $KHCO_3$, 10 mM HEPES, 30 mM Taurine, 10 mM BDM and 5.5 mM glucose, pH 7.4) and digested using Collagenase (41H21476, Worthington). The isolated ventricular myocytes were exposed to increasing concentrations of Ca^{2+} (100 μM, 400 μM and 900 μM) to render myocytes Ca^{2+} tolerant. Cardiomyocytes were plated on laminin-coated plates at a density of 40-60 x 103 cells/plate and incubated at 37°C. The media was changed to cardiomyocyte culture media (Minimum Essential Media containing 0.1% BSA, 10 mM BDM, 100 U/ml penicillin, 2 mM glutamine and 2 mM ATP) after 2 hrs of plating.

2.2.2 H9C2 rat cardio myoblast culture.

Female H9C2 rat embryonic cardiomyoblast (CRL-1446; ATCC) cells were cultured at a cell density of 300,000 cells in 60 mm plates and maintained in Dulbecco's modified Eagle's high glucose medium (SH30243.01; DMEM-HG; Hyclone Laboratories, UT, USA) supplemented with 10% fetal bovine serum (1400-500; FBS, Seradigm) for 48 hr. H9C2 cardiomyoblasts were allowed to differentiate from cardiomyoblasts to cardiomyotubes for 48 hrs in DMEM-1X medium (11966025; Thermo Fisher Scientific, MA, USA) supplemented with 0.5% FBS and 5 mM glucose. After 48 hrs of

differentiation, cells were exposed to either low or high concentrations of different substrates, as mentioned in section 2.2.5.

2.2.3 miRNA mimic treatment.

miR-30b-5p endogenous expression was inhibited in H9C2 using a rat specific miR-30b mimic. H9C2 cells were plated at a seeding density of 300,000 cells/60mm dishes and differentiated for 48 hrs in DMEM-1X medium (11966025; Thermo Fisher Scientific, MA, USA) supplemented with 0.5% FBS and 5 mM glucose. Subsequently, the culture media was exchanged with fresh differentiated media containing 5nm of rat-specific miR-30 mimic (219600; miScript miRNA Mimic - Syn-rno-miR-30b-5p; Qiagen) for 24 hrs. Following this, the cells underwent treatment with a combination of 1.2 mM palmitate (see section 2.2.5) and miR-30 mimic for 16 hours before being harvested using 1X- phosphate-buffered saline (PBS; MT21040; Corning). The lysates were stored at -80ºC for protein isolation and TFEB immunoblotting analysis (see sections 2.3.1 and 2.3.3).

2.2.4 Insulin signalling.

Adult mouse cardiomyocytes (AMCMs) were isolated and plated in 30mm dishes containing cardiomyocyte culture media. The cells were allowed to rest for 2 hrs, following which 100nM insulin (Bovine insulin I0516; Sigma was diluted to a final concentration of 100nM) containing media was added to the cells and incubated for 15 min at 37°C. After incubation, plates were placed on ice to stop the reaction and washed in warm 1X phosphate-buffered saline (PBS; Corning; MT21040) before harvesting for protein analysis (see sections 2.3.1 and 2.3.3).

2.2.5 Preparation of bovine serum albumin (BSA) complexed fatty acid.

Bovine serum albumin (BSA): FA solutions were prepared in DMEM 1X, glucose-free medium. 100mM stock solutions of sodium palmitate (P9767; Sigma) and sodium oleate (O7501; Sigma) were prepared in DMEM1X media at a total volume of 7.5mL and heated to 95°C in a boiling water bath to dissolve FA. 1% FA-free BSA (68700; Proliant Biologicals) solution was prepared in serum-free DMEM1X, wherein BSA was dissolved by centrifugation for 5min at 2500g and subsequently warmed at 50°C to dissolve further. 100mM stocks of palmitate were diluted to final concentrations of 0.8 or 1.2 mM, as indicated in figure legends, in pre-warmed 1% BSA. The resulting FA: BSA (4:1) solution was incubated at 50°C for 20 min to complex, prior to sterile filtering for cell culture

treatment [105]. Media in wells was replaced with FA: BSA treatment and incubated for 16 hrs at 37ºC prior to harvest or further treatment.

2.2.6 Presto blue cell viability assay

H9C2 rat cardiomyoblasts were seeded in a 96-well plate at a density of 3000 cells per well in 200 µL of DMEM-HG + 10% FBS. H9C2 cells were differentiated for 48 hrs and then treated with increasing concentrations of Cycloheximide (CHX) (66-81-9; Biovision) (10µM, 15µM, 30µM, 45µM, 75µM, 100µM) for 16 hrs. 2µM Doxorubicin (CA80058-048; EMD Chemicals) was used as the positive control, whereas untreated cells were used as a negative control. Following the treatment, presto blue reagent (A13261; Invitrogen) was added according to the manufacturer's specifications. The plate was read at time points ranging from 0.5-4 hrs in a Synergy H4 plate reader at a wavelength of 570nm.

2.2.7 SUnSET Assay.

Protein synthesis was measured in vitro by the Surface Sensing of Translation (SUnSET) assay. The SUnSET assay measures protein synthesis by quantifying puromycin incorporation into newly synthesized proteins. H9C2 cells were plated in 60mm dishes and differentiated 48 hrs as previously described. This was followed by 35µM CHX treatment in DMEM1X media with 0.5% FBS and 5mM glucose for 16 hrs. This was followed by 6 hr serum starvation and incubation in serum-free DMEM1X media. 50mM puromycin dihydrochloride (P8833; Sigma) was prepared in ddH_2O. The stock solution was further diluted in DMEM1X media with 0.5% FBS and 5mM glucose to 1mM, and a puromycin solution was prepared at a final concentration of 1nM. Media in wells was replaced with 1nM puromycin treatment, or media-only control, in which cells were incubated for 30min at 37°C. Cells were subsequently washed with warm 1X PBS, harvested, and prepared for further protein analysis (as described in section 2.3.1). Puromycin incorporation was detected by western blotting using the monoclonal puromycin antibody (MABE343; Millipore) at a final concentration of 1:5000.

2.2.8 Inhibiting proteasomal degradation in H9C2.

H9C2 rat cardiomyoblasts were seeded in a 60mm dish at a density of 300,000 cells per well in 3mL of DMEM-HG + 10% FBS. The cells were then differentiated for 48 hrs using DMEM-1X medium supplemented with 0.5% FBS and 5mM glucose. Subsequently,

cells were treated with 3μM Mg-132 (1211877-36-9; Millipore Sigma) for 4 hrs, followed by 0.8mM Palmitate treatment (see section 2.2.5) for 16 hrs. The cells were harvested using 1X- phosphate-buffered saline (PBS; MT21040; Corning), and the lysates were used for protein isolation and quantification (see section 2.3.1) following immunoblot analysis (see section 2.3.3) of TFEB protein.

2.2.9 Mitochondrial respiration analysis.

Oxygen flux in AMCMs was measured using the Oxygraph-2k (OROBOROS Instruments). Following isolation, the cells were plated in media (Minimum Essential Media containing 0.1% BSA, 10mM BDM, 100 U/ml penicillin, 2 mM glutamine and 2 mM ATP) for 2 hrs. At this point, the cells were rinsed with warm PBS prior to 15-minute incubation with warm Accutase (A6964; Sigma Aldrich) to detach the cells. Detached cells were collected and centrifuged at 300g for 5min. Subsequently, Accutase was discarded, and cells were resuspended in mitochondrial respiration medium (MiR05) buffer (Table 1) and diluted to a final concentration of 20-30,000 cells/mL. Consequently, cells were permeabilized with 25μg/mL saponin to prepare for respirational analysis in 2mL oxygenated-MiR05 buffer at 37°C in oxygraph chambers.

Respiration and FA oxidation were estimated after the sequential addition of malate, palmitate, and adenosine diphosphate (ADP). Details of the addition and titration of substrates and inhibitors are listed in Table 2. The instrument baseline was allowed to stabilize between each addition. Following respiration analysis, cells were collected into 2.0mL tubes from oxygraph chambers and centrifuged at 10,000 g for 5 min at 4°C. The supernatant was aspirated, and the resulting protein pellet was stored at -80°C for BCA protein assay, as described in section 2.3.1. Mitochondrial respiration was normalized to cell count and protein concentration in μg/mL.

Table 1: Chemical components, concentrations, and vendor information for mitochondrial respiration medium (MiR05) buffer

Chemical Compound	Concentration	Vendor; Catalog Number
EGTA	0.5 mM	Sigma; E4378
$MgCl_2$-$6H_20$	3 mM	Scharlau; MA0036
Lactobionic acid	60 mM	Sigma; 153516
Taurine	20 mM	Sigma; T0625
KH_2PO4	10 mM	Merck; 104873
HEPES	20 mM	Sigma; H7523
Sucrose	110 mM	Sigma; 84097
Fatty acid-free-BSA	1 g/l	Sigma; A6003

Table 2: Substrate uncoupler inhibitor titration protocol to examine fatty-acid oxidation in saponin-permeabilized AMCMs and Myofibrils.

Chemical	Concentration	Mark	Vendor; Catalog Number
Saponin	20 µM	Sap	Sigma; S4521
Malate	0.5mM	M	Sigma; M1000
Palmitate	5mM	Pyr	Sigma; P5280
ADP	0.1mM	D 0.1	Sigma; A2754
ADP	0.5mM	D 0.5	Sigma; A2754
ADP	5mM	D 5	Sigma; A2754
Octanoyl-carnitine	0.2mM	Oct	Sigma; 50892
FCCP	0.5µM	FCCP	Sigma; C2920
Rotenone	0.5µM	R	Sigma; R8875
Succinate	10µM	S	Sigma; S3674
Antimycin A	5µM	AmA	Sigma; A8674

2.3 Immunoblotting.

2.3.1 Sample processing and protein lysate preparation.

Cells (H9C2, AMCMs) were harvested in ice-cold 1X PBS, transferred to microcentrifuge tubes, and pelleted by centrifugation at 10,000g for 10 min. Ice-cold lysis buffer (20mM Tris, 5mM EDTA, 10mM $Na_4P_2O_7$, 100mM Sodium Fluoride, 1% NP-40 and ddH_2O) along with protease (P8340, Sigma Aldrich) and phosphatase inhibitor (524628, Calbiochem) cocktails was added, and cell pellets were subsequently sonicated three times for 10 seconds, with 5 seconds each on the ice between each sonication. Human atrial appendages (AA) were homogenized for 10 seconds in a lysis buffer and then sonicated three times for 10 seconds each. Lysates were allowed to settle on the ice before

centrifugation for 18 min at 12000 g. The supernatant (total lysate) was aspirated and stored at -80º C until needed. Cell and tissue lysates were diluted 1:5-10 prior to using the Pierce BCA Protein Assay Kit (23225; Thermo Fisher Scientific) to determine protein concentration, according to the manufacturer's instructions. Protein samples (10-30µg) were diluted in 4X Laemmle Buffer with 1mM dithiothreitol (DTT) and boiled for 5min at 100°C.

2.3.2 Myofilament isolation and processing.

Myofilaments were isolated from whole heart tissues and isolated cardiomyocytes. Tissues collected were excised and rinsed in 1ml ice-cold 1X PBS and transferred to a 1ml glass Kimble mortar (885450-0020) containing 250µl-1ml ice-cold K60 buffer; 60mM KCl, 30mM imidazole at pH 7.0, and 2mM MgCl2, with freshly added protease [P8340; Sigma-Aldrich] and phosphatase [524628; Calbiochem] inhibitor cocktails at a volumetric ratio of 100:1:1). Samples were gently homogenized on ice with a glass Kimble pestle until tissues or cells became dissociated and insoluble white myofilaments were visible. Samples were then transferred to a fresh 1.5ml microcentrifuge tube and placed on ice.

Following homogenization, the myofilament lysates were centrifuged at 14,000g for 15min at 4°C. The supernatant was discarded, and the remaining pellet was resuspended by gentle pipetting in 1ml K60 buffer supplemented with 1% Triton X100 (v/v; Sigma Aldrich Cat# T9284-100ML). Samples within the ice box were tilted to a 45° angle to maximize K60-Triton mixing. Ice boxes containing samples were transferred to a shaker plate and left to shake at 150 rpm for 45min until insoluble filaments became completely white. Samples were then centrifuged at 1100g for 15min at 4°C. Supernatants were discarded, and white myofilament pellets were washed by resuspension in 0.5ml cold K60 buffer. Samples were centrifuged once again at 1100 g for 15min at 4°C. This wash-and-centrifugation step was repeated three times. After the fourth wash and centrifugation, supernatants were discarded, and myofilaments were re-suspended in 250µl K60 buffer. Myofilament protein content was measured by BCA assay using a 1-in-10 dilution in ddH_2O. The samples were stored at -80°C for phosphoprotein staining.

2.3.3 Western Blotting.

Protein samples were denatured and electrophoresed using 10% Mini-Protean Sodium dodecyl sulphate (SDS) polyacrylamide gel electrophoresis or by pre-cast CriterionTM TGXTM 4-20% acrylamide gradient gels (5671095; Bio-Rad). Samples were loaded alongside Precision Plus Protein™ Standards Kaleidoscope™ ladder (1610375; BioRad). Criterion™ gels were run at 90V for 30 min and 120V for 90 min on ice. Protein was transferred to nitrocellulose membranes (0.2µM; 1620112; Biorad) at 90V for 1hr 30min at 4°C in 1X Tris/Glycine Transfer Buffer (1610771EDU; Biorad) with 20 % methanol. Following the transfer, membranes were rinsed in ddH_2O and stained with the Pierce Reversible Protein Stain Kit (24580; Thermo Fisher Scientific) to assess loading and transfer efficiency. Membranes were imaged using a ChemiDoc MP Imaging system, and the stain was removed using Pierce Stain Eraser. Subsequently, membranes were blocked with 5% skim milk made in tris-buffered saline (TBS) with 0.05% Tween-20 (0777; VWR) (TBS-T) before overnight incubation at 4°C in primary antibodies (1% milk-TBS-T with sodium azide) targeting TFEB (A303-673A; Bethyl Labs), pAKT s473 (4060; Cell Signalling), pAKT T308 (07-416; Millipore), Akt (07-416; Millipore), Puromycin (MABE343; Millipore). Membranes were incubated with horseradish peroxidase (HRP)-tagged anti-mouse (1:1000-5000; 7076S, Cell Signaling), anti-rabbit (1:1000-5000; 7074S, Cell Signaling) secondary antibody diluted in 5% milk-TBS-T for 2 hrs at room temperature. Proteins were visualized using Western Lightning Plus chemiluminescent substrate (NEL103E001EA; PerkinElmer) or Clarity™ Western Enhanced Chemiluminescence Substrate (1705060S; BioRad). To strip the protein from the blots prior to re-probing, membranes were incubated in 50mL of 0.5M Tris-HCl/SDS buffer supplemented with 250µl β-mercaptoethanol (6010; OmniPur®) for 1 hour at 50°C.

2.3.4 Phosphoprotein staining.

Gel electrophoresis was performed as previously described in section 2.3.3, with an addition of a phosphoprotein standard ladder (Peppermint Stick ladder, P27167; Invitrogen). The Peppermint Stick ladder was prepared fresh by adding 3µl of ladder to 9µl 4X Laemmle Buffer with 1M DTT and boiling for 5min. After electrophoresis was completed, gels were submerged into a glass container filled with ddH_2O. Water was discarded, and the gel was immersed in fresh fixative solution (100ml; 80ml ddH_2O, 100ml

methanol, and 20ml glacial acetic acid) with a lid seal. The gel was incubated in fixative at room temperature—with gentle agitation—for at least 30min, after which the fixative was renewed for another 30min to ensure SDS removal. Following the second incubation in fixative, gels were rinsed and completely submerged in ddH_2O three times for 10min each with gentle agitation. Water was discarded and gels were stained with Pro-Q™ Diamond phosphoprotein stain (P33300; Invitrogen) while protected from light for 90min. All subsequent steps were performed with the gel protected from light. Gels were gently washed three times in 100ml Pro-Q™ Diamond Phosphoprotein Gel Destaining Solution (P33310; Invitrogen) for 30min followed by a 100ml ddH_2O wash for 5min. For phosphoprotein imaging, gels were transferred to a translucent cover sheet and then onto a clean ChemiDoc MP transilluminator (Bio-Rad). Gels were imaged via Image Lab using the built-in Pro-Q™ Diamond UV excitation protocol.

2.3.5 Coomassie Gel Staining.

Coomassie stain (0.25%) was prepared by adding 0.5g Coomassie Brilliant Blue R-250 (Amresco Cat# 0472-25G) to a solution of 100ml methanol, 20ml glacial acetic acid, and 80ml ddH_2O. Coomassie stain was added directly to gels following phosphoprotein imaging and was incubated on a shaker plate overnight at 50rpm. Gels were then rinsed five times with ddH_2O and were subsequently incubated in fixative solution for 1.5hrs on a shaker plate. Fixative was renewed and gels were incubated for an additional 30min until the background became clear and colorless. Gels were rinsed in ddH_2O and transferred to a translucent cover sheet, then to a White Light Conversion Screen (Bio-Rad) inserted into a Bio-Rad ChemiDoc MP Imaging System. Gels were imaged via Image Lab using the default colorimetric imaging protocol.

2.3.6 Densitometry.

Densitometric analysis was performed using Image lab software v6.1 (Bio-Rad). Protein expression in arbitrary units was calculated by measuring the relative integrated density of the target protein stain normalized to the total protein density of the appropriate MemCode-stained blot. MemCode stain allows for the visualization of proteins and the efficiency of transfer to the nitrocellulose membrane and serves as a normalization tool and confirmation of equal protein loading.

2.4 Quantitative polymerase chain reaction (qPCR).

2.4.1 RNA extraction.

RNA was extracted from cell pellets using RiboZol RNA extraction reagent (VWR), cell pellets were resuspended in 750µL of RiboZol (VWRVN580; VWR) in RNase/DNase free tubes. Samples were sonicated for 30s before adding 300µL of chloroform (613312; Sigma Aldrich). Samples were quickly vortexed and inverted by hand 3X and incubated at room temperature for 3min until two separate layers were indistinguishable. Samples were centrifuged at 12,000g for 20min at 4ºC to separate the phases. The upper, colourless aqueous phase was transferred to a fresh RNase/DNase-free tube, while the lower phenol-red organic and interphases were discarded. This was followed by a second extraction with an additional 100µL of chloroform added to the upper phase. Samples were again inverted and incubated at room temperature before another centrifugation at 12,000g for 20min at 4ºC. Again, the upper phase was transferred to a fresh RNase/DNase-free tube, and the lower phenol-red organic and interphases were discarded. Ice-cold 100% isopropanol (500µL; Sigma-Aldrich) was added to the aqueous phase, and the tubes were inverted by hand before incubation at room temperature for 3 min. Samples were centrifuged at 12,000g for 20 min at 4ºC to pellet the RNA. The supernatant was discarded, and the RNA pellet was then rinsed and resuspended in 1mL ice-cold 75% ethanol prepared in nuclease-free water (10977-015; Life Technologies). Samples were briefly vortexed and then centrifuged at 7500g for 5min at 4ºC. The ethanol wash was discarded, and the RNA pellet was left to air dry for 20 min. The RNA pellet was re-suspended in 25 µL of nuclease-free water. Samples were briefly vortex and spun, and RNA was quantified using the BioTek Synergy H4 and Take3 plate by reading absorbance at 260/280nM.

2.4.2 Complementary DNA (cDNA) synthesis.

cDNA was prepared in two different ways for mRNA measurement and miRNA measurement. For regular mRNA detection and measurement, cDNA was synthesized for each sample by loading the volume equivalency of 500ng RNA template, 2µL of 5X qScript cDNA supermix (95048; Quantabio) and RNAse-free water up to a total volume of 10µL into RNase/DNase-free strip-tubes. The reaction was briefly vortexed and

centrifuged prior to incubation at 25ºC for 5 min, 42ºC for 30 min, 85ºC for 5 min and then held at 4ºC using a Master cycler Nexus Gradient Thermocycler (Eppendorf).

For miRNA detection and measurement, cDNA was synthesized by loading the volume equivalency of 25ng RNA template, 2µL of 5X miRCURY Buffer, 1µL of 10X miRCURY enzyme and made RNAse-free water up to a total volume of 10µL (as per kit instructions -miRCURY LNA RT Kit; #339340). cDNA was stored at -80°C until needed.

2.4.3 Applied Biosystems qPCR.

qPCR reactions were conducted in 96-well plates on a ViiA7 Real-time PCR machine (Thermo Fisher Scientific). For mRNA measurement, each well contained 2µL standard curve or cDNA template diluted 1:3-5, 5µL of Perfecta SYBR green Supermix - Low ROX supermix (95053; Quantabio), 0.25µl of each forward and reverse primer (see Table 3 for primer pair sequences) and 2.5µL of nuclease-free water in a total of 10µl per reaction mixture. The qPCR plate was centrifuged at 300 g for 1min prior to incubating the reaction mix at 95ºC for 20s, followed by 32 cycles for 1s at 95ºC, 20s at 60ºC, and 5min at 20ºC.

Similarly, for miRNA measurement, the cDNA prepared before was diluted 1:20 with RNAse free water. The reaction mixture contained 3µL of the diluted cDNA template, 5µL of 2X SYBR green master mix, 0.05µL of ROX reference dye, 1µL of specific primer and 1µL of nuclease free water in a total of 10µl (as per kit instructions - miRCURY LNA SYBR Green PCR Kit; # 339346). The qPCR plate was centrifuged at 300 g for 1min prior to incubating the reaction mix at 95ºC for 2min, followed by 32 cycles for 10s at 95ºC, 1min at 56ºC, and for 5min at 20ºC. Data were normalized to either one or geometric mean of two reference genes and quantified by the 2- ΔΔCt method. As previously reported [144], all miRNA data was normalized using miR-16 as the reference gene due to its prevalent expression in the heart.

Table 3 List of primers

Species and target	Primer Sequence (5'-3')
Mouse-TFEB F	GTAGAACTGAGTCAAGGCATACTGG
Mouse-TFEB R	GGGTCCTACCTACCACAGAGCC
Mouse-LOX P	CTTCGTATAATGTATGCTATACGAAG
Mouse-LAR 3	CAACGGGTTCTTCTGTTA GTCC
Mouse-ET-189 R	ATGGCTAATCGCCATCTTCCAGCA
Mouse-ET-188 F	GCC CTGGAAGGGATTTTTGAAGCA
Mouse-ET-191 R	GGTCAGCCTAATTAGCTCTGT
Mouse-ET-190 R	GATCTCCAGCTCCTCCTCTGTC
Mouse-RPL 27 F	AAGCCGTCATCGTGAAGAACA
Mouse-RPL 27 R	CTTGATCTTGGATCGCTTGGC
Mouse-HPRT1 F	CAGTCCCAGCGTCGTGATTA
Mouse-HPRT1 R	GGCCTCCCATCTCCTTCACG
Human-TFEB F	GGTGCAGTCCTACCTGGAGA
Human-TFEB R	GTGGGCAGCAAACTTGTTCC
Human-YWHAZ F	ACGTCCCTCAAACCTTGCTT
Human-YWHAZ R	TGAGTGTGGCTGAGTGATGG
Human-PPIA F	AGACAAGGTCCCAAGAC
Human-PPIA R	ACCACCCTGACACATAAA
Human-GAPDH F	TGCACCACCAACTGCTTAGC
Human-GAPDH R	GGCATGGACTGTGGTCATGAG
hsa-miR-30b-5p	5'UGUAAACAUCCUACACUCAGCU
hsa-miR-29a-3p	5'UAGCACCAUCUGAAAUCGGUUA
hsa-miR-132b-3p	5'UAACAGUCUACAGCCAUGGUCG
hsa-miR-212-5p	5'ACCUUGGCUCUAGACUGCUUACU
hsa-miR-16-5p	5'UAGCAGCACGUAAAUAUUGGCG

2.5 Lipid droplet staining and quantification.

Isolated cardiomyocytes were plated on 60 mm plates with a coverslip at a density of 0.5 x 10^6 and treated with BSA or 1.2mM oleate for 16 hrs to induce lipid droplet formation. Oil Red O stock solution was prepared by dissolving 300 mg of Oil Red O powder (O0625; Sigma Aldrich) in 100 ml of 100% isopropanol. Oil Red O working solution was prepared by adding 3 parts of Oil Red O stock solution to 2 parts of water, following which the solution was filtered through Whatman filter paper (1001-150; Whatman Filter Papers). Cells were washed 2X with PBS and fixed using 10% formalin for 30 mins. After fixing, cells were washed twice with PBS and incubated with 60% isopropanol for 5 mins. After 5 mins, isopropanol was discarded, and cells were covered

evenly with the Oil Red O working solution for 20 mins. Cells were then washed with water carefully to discard the excess stain and incubated with hematoxylin (72704; Thermo Fisher Scientific) for 1 min to stain the nuclei. Following hematoxylin staining, cells were washed, and the coverslips were mounted onto glass slides using ProLong Gold Antifade Reagent (P36391; Thermo Fisher). Coverslips were allowed to harden for 48hrs prior to imaging slides on Zeiss LSM 900 with Airyscan 2 detector. The images obtained were used to quantify the number of lipid droplets. The area of cardiomyocytes covered with lipid droplets was quantified using HALO software.

2.6 Statistical Analysis

Statistical analyses were performed in Graph Pad Prism 9. Data sets with three or more groups were analyzed using one-way or two-way analysis of variance (ANOVA). Significant differences between individual groups were assessed with Tukey's post-hoc test. A pairwise comparison between data sets with two groups was performed using a two-tailed Student's t-test. P-values less than 0.05 were considered statistically significant. Unless otherwise indicated, data are presented with a standard error of the mean (±SEM).

Chapter 3: Results

3.1 miRNA-30b-5p is expressed in H9C2 cells.

Earlier studies from our lab revealed that TFEB content was depleted in cardiomyocytes and hearts in diet-induced obesity, STZ diabetes, and ex-vivo in response to palmitate exposure [105], suggesting that lipotoxic milieu decreased cellular TFEB. Mechanisms or pathways contributing to TFEB decline during lipotoxicity remain to be ascertained. Notably, micro-RNAs (miRNAs), specifically miR-29, 30, 132/212 [138] [132, 133, 145].were reported to alter TFEB content in different cells, including PDAC and HEK293. We surmised whether lipotoxicity induces the expression of TFEB degrading miRNAs to decrease TFEB expression and content. My initial approach was to examine if I could detect miRNAs (miR29,30,132,212) in differentiated H9C2 cells using the commercially available miRCURY LNA RT kit. I detected miRNAs 29, 30, 132-212 in unstimulated conditions (**Figure 3.1 A-B)**. To validate the expression, data were normalized to the CT values of two reference genes, Uni6 (**Figure 3.1 A)** and miR-16 **(Figure 3.1 B),** in H9C2 cells. Amongst the detected miRNAs, I chose to study miRNA-30-5p since it directly targets TFEB mRNA, as opposed to other miRNAs that indirectly affect TFEB transcription [133].

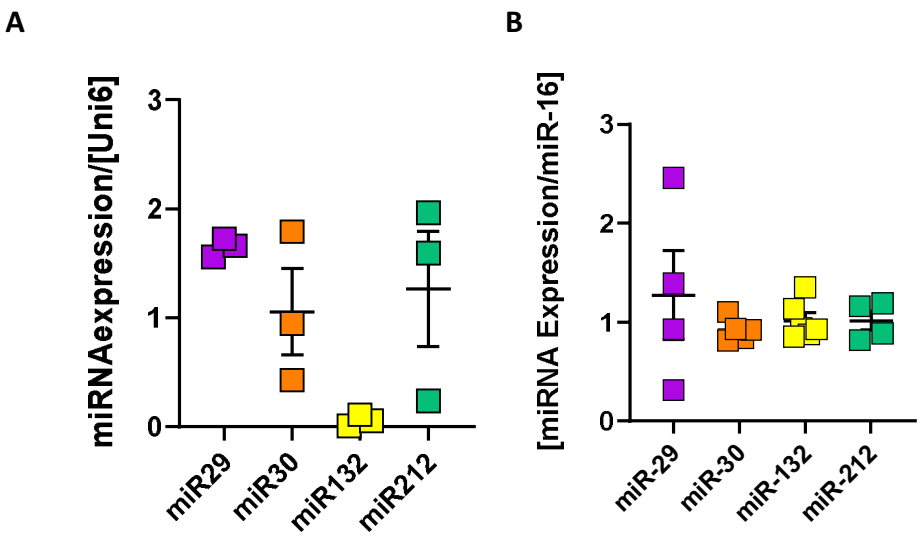

Figure 3.1 Detection of miRNAs in unstimulated H9C2 cells. (A) miRNA expression of miR-29, miR-30, miR-132 and miR-212 normalized to endogenous Uni 6 ctrl. (B) miRNA expression of miR-29, miR-30, miR-132 and miR-212 normalized to miR-16. n=4 for A-B.

3.2 miRNA-30b-5p expression is elevated in palmitate-treated H9C2 cells.

After confirming the detection of miRNAs in unchallenged differentiated H9C2 cells, we next sought to examine if palmitate lipotoxicity altered the expression of miRNA-30b-5p in H9C2 cells. miRNA-30b-5p expression was significantly elevated at 16 hrs in palmitate-treated cells compared to 1% BSA- controls **(Figure 3.2 A),** with a concomitant decline in cellular TFEB-content **(Figure 3.2 B-C)**. Data was normalized to miR-16. These findings present a robust correlation between increased miRNA-30b-5p expression and decreased TFEB content following palmitate overload.

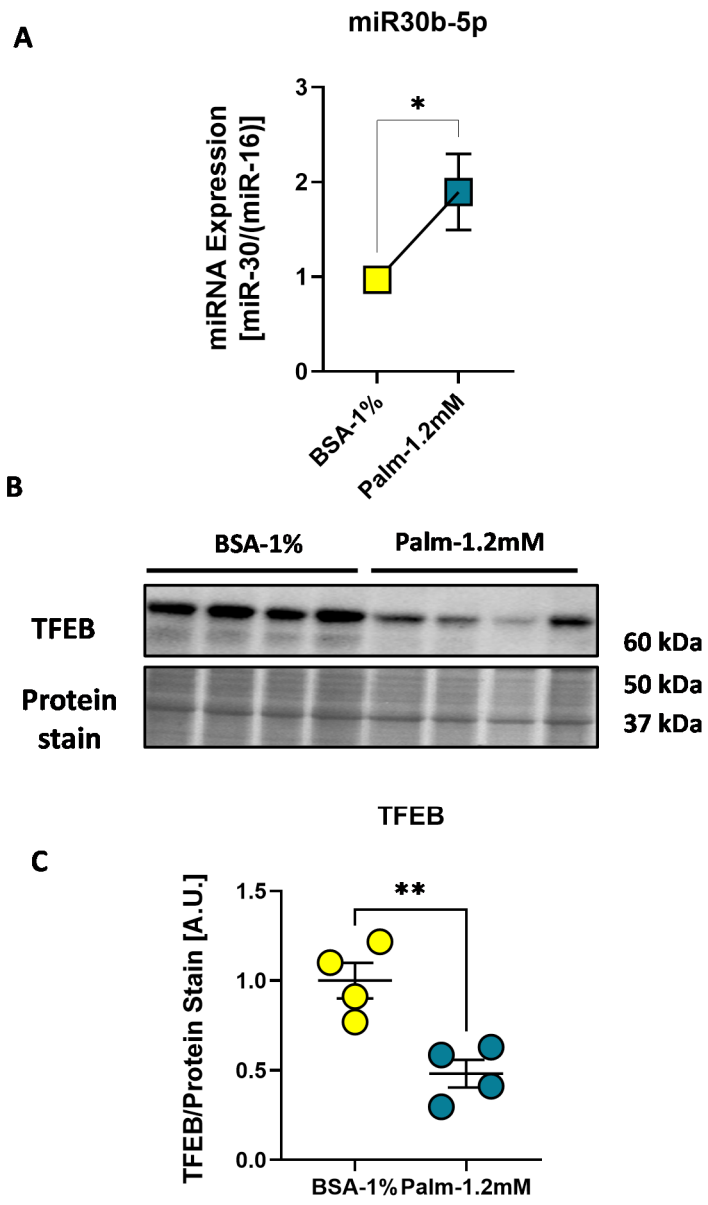

Figure 3.2 miR30b-5p is elevated in palmitate-treated H9C2 cells. H9C2 cells were differentiated for 48hrs prior to treatment with BSA-1% or Palmitate-1.2mM for 16 hours. (A) miR-30b-5p expression in H9C2 cells normalized to miR-16. (B-C) Immunoblot and densitometric analysis of TFEB. Data is normalized to protein stain. The graph represents mean ± S.E.M. Statistical analysis was performed using an unpaired t-test, *$p<0.05$ for BSA-1% vs Palm-1.2mM, n=12 (A)**$p<0.01$ for BSA-1% vs Palm-1.2mM, n=4 (C), AU; Arbitrary Unit. Note: all the presented immunoblot lanes are from the same membrane.

3.3 miRNA-30b-5p is increased, and TFEB is decreased in the atrial appendages of patients with obesity.

I next determined if our cell line data could be extended to the human population, specifically in patients with obesity and CVD. Atrial appendage (AA) samples were collected from patients registered in the OPOS (Impact of Obesity on Prospective Outcomes following cardiac Surgery, TCPS-2–2014) trial [146]. Patients were stratified as per their body mass index (BMI) as non-obese (N-O, BMI 18.5-24.9 kg/m2), pre-obese (P-O, BMI 25-29.9 kg/m2), and obese class-I-III (BMI 30-34.9 kg/m2) **(Figure 3.3 A).**

TFEB mRNA is significantly and progressively decreased in AA samples of patients within the obese and preobese classes when compared to the non-obese group **(Figure 3.3 B)**. A decrease in TFEB mRNA translated into a corresponding reduction in TFEB protein content within samples of patients with obesity and decreasing trend within the preobese group compared to the non-obese samples **(Figure 3.3 C-D)**. A significant elevation in miRNA 30b-5p was observed in the obese samples **(Figure 3.3 E)** compared to preobese and non-obese groups. Data were normalized to hGAPDH for AA samples. These data suggest that miRNA-30b-5p levels are elevated during obesity, possibly driving decreases in TFEB mRNA and protein content within the heart.

(See figure on next page)

Figure 3.3 miR30b-5p expression is elevated in atrial-appendage samples from patients with obesity related CVD. (A) Body mass-index. (B) TFEB mRNA expression in the atrial appendages, data normalized to YWHAZ/PPIA reference genes. (C-D) Immunoblot and densitometric analysis of TFEB. Data is normalized to protein stain. Ran GTPase served as a protein loading control. (E) miR-30b-5p expression in atrial appendages normalized to hGAPDH reference gene. The graph represents mean ± S.E.M. Statistical analysis was performed using ordinary one-way ANOVA, ****$p<0.0001$ for Non-obese vs Obese and ***$p<0.001$ for Pre-obese vs Obese, n=4-7(A); **$p<0.01$for Non-obese vs Obese (B); ****$p<0.0001$ for Non-obese vs Pre-obese and ****$p<0.0001$ for Non-obese vs Obese; *$p<0.05$ for Non-obese vs Obese, n=4-7 (D); **$p<0.01$ for Pre-obese vs Obese, n=4-5 (E) AU; Arbitrary Unit. Note: all the presented immunoblot lanes are from the same membranes.

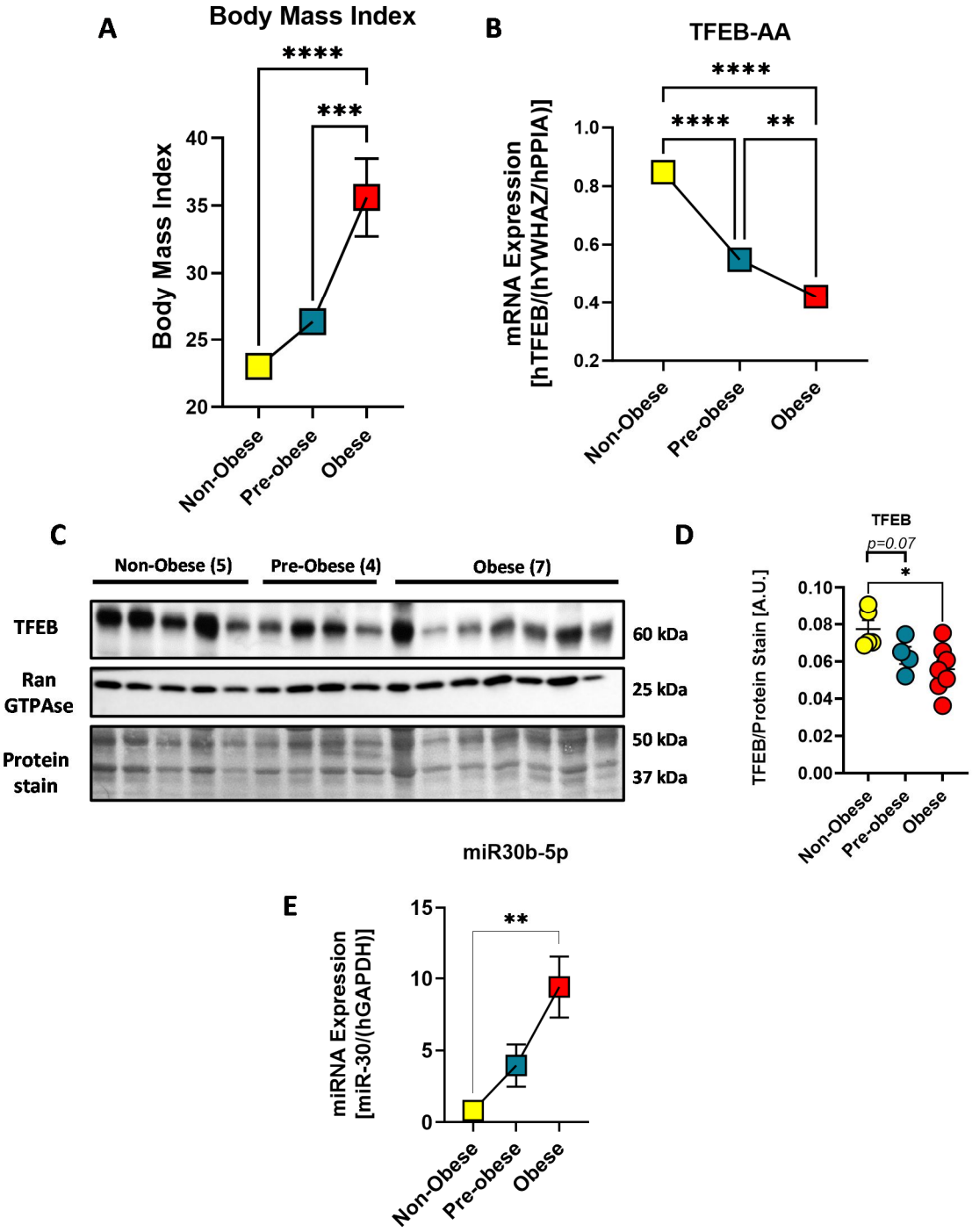

(See legend on the previous page)

3.4 Mimicking miR-30b-5p protects cardiac TFEB content during lipotoxicity.

I next examined if inhibitory mimicking of miR-30b-5p would prevent the decline in TFEB content during lipotoxicity. TFEB content in the cells pretreated with miR-30 inhibitory mimic increased significantly despite palmitate treatment (**Figure 3.4 A-B)**. These observations indicate that mimicking miR-30b-5p prevents TFEB decline during lipotoxicity in H9C2 cells.

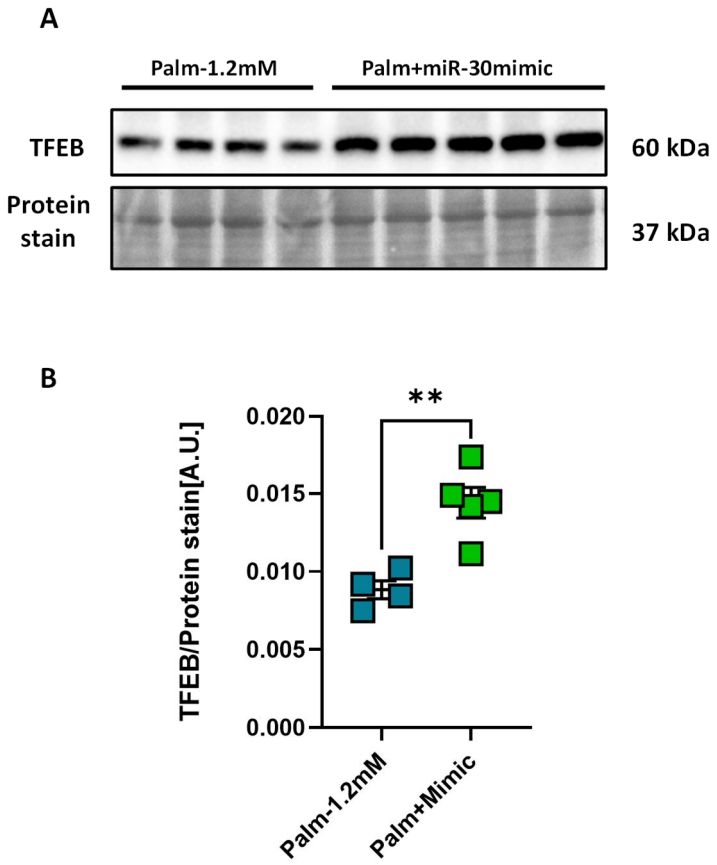

Figure 3.4 Mimicking miR-30b-5p protects cardiac TFEB content during lipotoxicity. H9C2 cells were differentiated for 48hrs prior to miR-30 mimic treatment (5nM) for 24 hrs. Cells were then treated with Palmitate-1.2mM for 16 hours. (A-B) Immunoblot and densitometric analysis of TFEB. Data is normalized to protein stain. The graph represents mean ± S.E.M. Statistical analysis was performed using unpaired T-test, **p<0.01 for Palm-1.2mM vs Palm+miR-30mimic, n=4-5 (B); AU; Arbitrary Unit. Note: all the presented lanes are from the same membranes.

3.5 Cycloheximide inhibits protein synthesis in H9C2 cells.

In addition to posttranscriptional regulation of TFEB, posttranslational turnover of TFEB is equally important in maintaining cellular TFEB content. I sought to investigate if lipotoxicity activates the post-translational degradation of TFEB. To do so, I initially examined the half-life of the TFEB protein in H9C2 cells by using Cycloheximide (CHX), a protein synthesis inhibitor. Cycloheximide (CHX) interferes with the translocation step blocking the translational elongation [147] and protein synthesis. When cells are treated with CHX, the extent of TFEB protein remaining in the cells after inhibition of protein synthesis is the amount subjected to degradation, which can be estimated using protein degradation inhibitors.

Cell viability assays using Presto Blue reagent showed that CHX decreased cell viability at 10μM, 15μM, 30μM, 45μM, 75μM, and 100μM **(Figure 3.5 A-B)**, however, viability of cells treated with all concentrations of CHX was significantly higher than positive control Doxorubicin (DOX), a chemotherapeutic (**Figure 3.5 B)** implying reduced toxicity of CHX in H9C2s compared to DOX.

After determining the cytotoxicity of CHX, the next aim was to test the ability of CHX to inhibit protein synthesis. SUnSET assay was performed, which involves the incorporation of puromycin into the nascent peptide chain, reflecting the rate of in vitro protein translation [148]. After 48 hrs of differentiation, H9C2 cells were incubated with 35μM CHX for 16 hrs and then treated with 1nM of Puromycin for 30 minutes before harvest and immunoblotting with monoclonal puromycin antibody to detect puromycin levels in H9C2 samples **(Figure 3.5 C-D)**. Cells treated with CHX significantly reduced puromycin levels compared to DMSO vehicle control, indicating that 35μM effectively reduced protein synthesis in H9C2 cells.

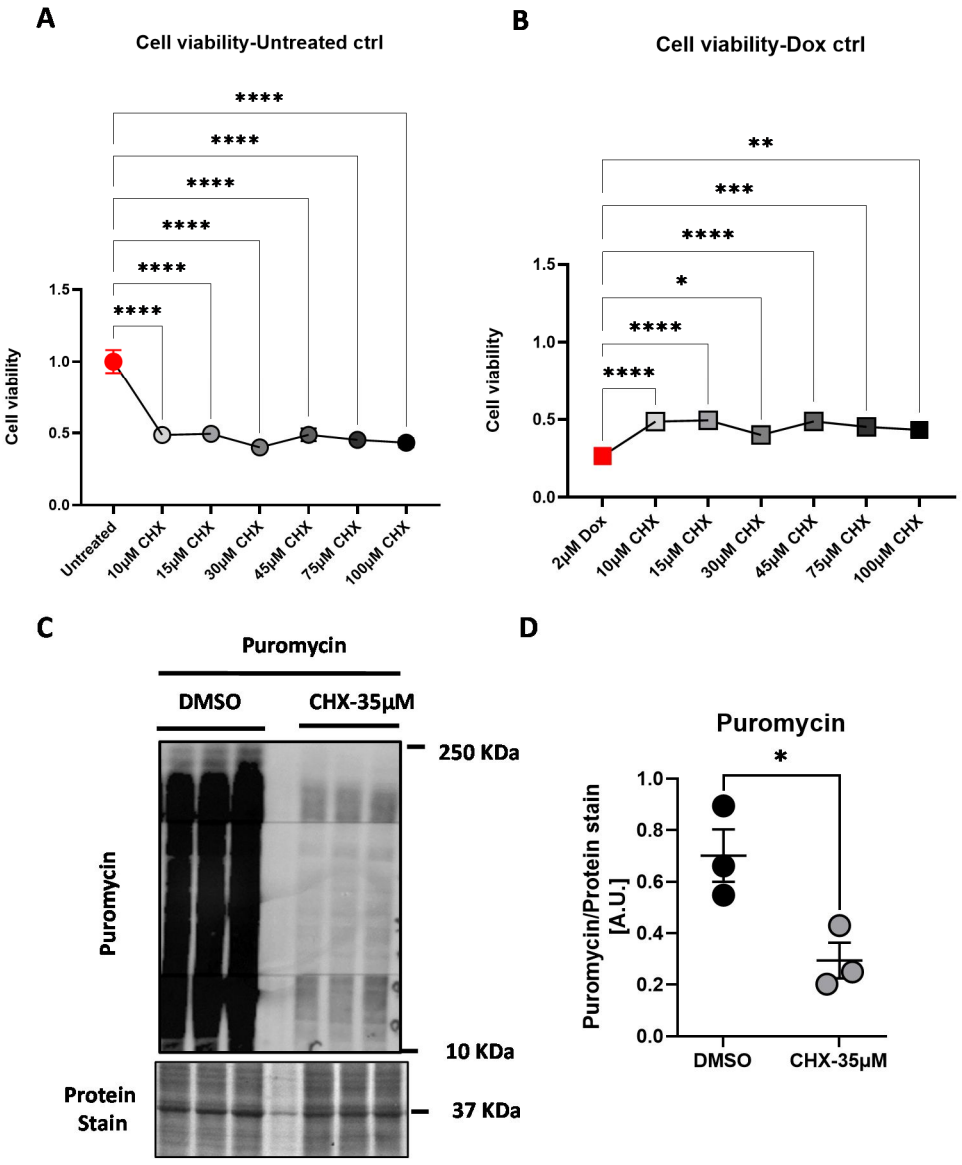

Figure 3.5 Cycloheximide inhibits protein synthesis in H9C2 cells. Cell viability of H9C2s treated with varying concentrations (10μM, 15μM, 30μM, 45μM, 75μM, 100μM) of CHX for 16 hours, corrected to untreated media as a negative control (A) and Doxorubicin as a positive control (B). (C-D) Immunoblot and densitometric analysis of cells treated with either DMSO or CHX prior to puromycin treatment. Data is normalized to protein stain. The graph represents mean ± S.E.M. Statistical analysis was performed using two-way ANOVA, followed by Tukey's multiple comparison tests for (A-B), n=6, ****p<0.0001, ***p<0.001, **p<0.01, *p<0.05 for media or Dox vs CHX, or T test for (D), n=3, *p<0.05 for DMSO vs 35μM CHX. AU; Arbitrary Unit. Note: all the presented lanes are from the same membrane.

3.6 Palmitate significantly accelerates TFEB protein degradation.

Given that CHX inhibits protein synthesis in H9C2, the subsequent aim was to determine TFEB protein turnover. H9C2 cells were differentiated for 48 hrs and then treated with 35μM CHX or DMSO for 4hrs, 8hrs, and 16hrs before harvesting. Immunoblot and densitometric analysis revealed that TFEB protein content was significantly reduced upon CHX treatment at 4, 8, and 16 hrs **(Figure 3.6 A-D),** signifying that residual TFEB protein content after CHX-induced inhibition of protein synthesis is diminished by 16 hrs in the myocyte. The half-life of TFEB (a time at which 50% of cellular TFEB is degraded) in myocytes is plausibly 16 hrs, and indeed this data closely correlates with the half-life of TFEB in other cell types such as 13.5 hrs in SH-SY5Y neuroblastoma cells [149].

Cells were treated with 0.8mM Palmitate and 35μM CHX for 16 hrs to ascertain if palmitate induces TFEB degradation. TFEB was significantly decreased in cells treated with a combination of palmitate and cycloheximide compared to the cells that were treated with either palmitate or cycloheximide **(Figure 3.6 E-F)** alone. This suggests that palmitate actively promotes TFEB degradation however, the location and mechanisms remain unclear.

(See figure on the next page)

Figure 3.6 Palmitate significantly accelerates TFEB protein degradation. (A-D) Immunoblot and densitometric analysis of H9C2s treated with 35μM CHX for 4, 8, and 16hrs. (E-F) Immunoblot and densitometric analysis of cells treated with a combination of 0.8mM Palmitate and CHX for 16 hrs following differentiation. Data is normalized to protein stain. The graph represents mean ± S.E.M. Statistical analysis was performed using either unpaired T test for (B-D), n=3, **p<0.01 and *p<0.05 for DMSO ctrl vs CHX; or one-way ANOVA for (F), n=4, ****p<0.0001 for BSA-1% vs Palm+CHX; ***p<0.001 for BSA-1% vs Palm-0.8mM; *p<0.05 for BSA-1% vs CHX-35μM; **p<0.01 for Palm+CHX vs CHX-35μM, AU; Arbitrary Unit. Note: all the presented immunoblot lanes are from the same membranes. Experiments were repeated thrice.

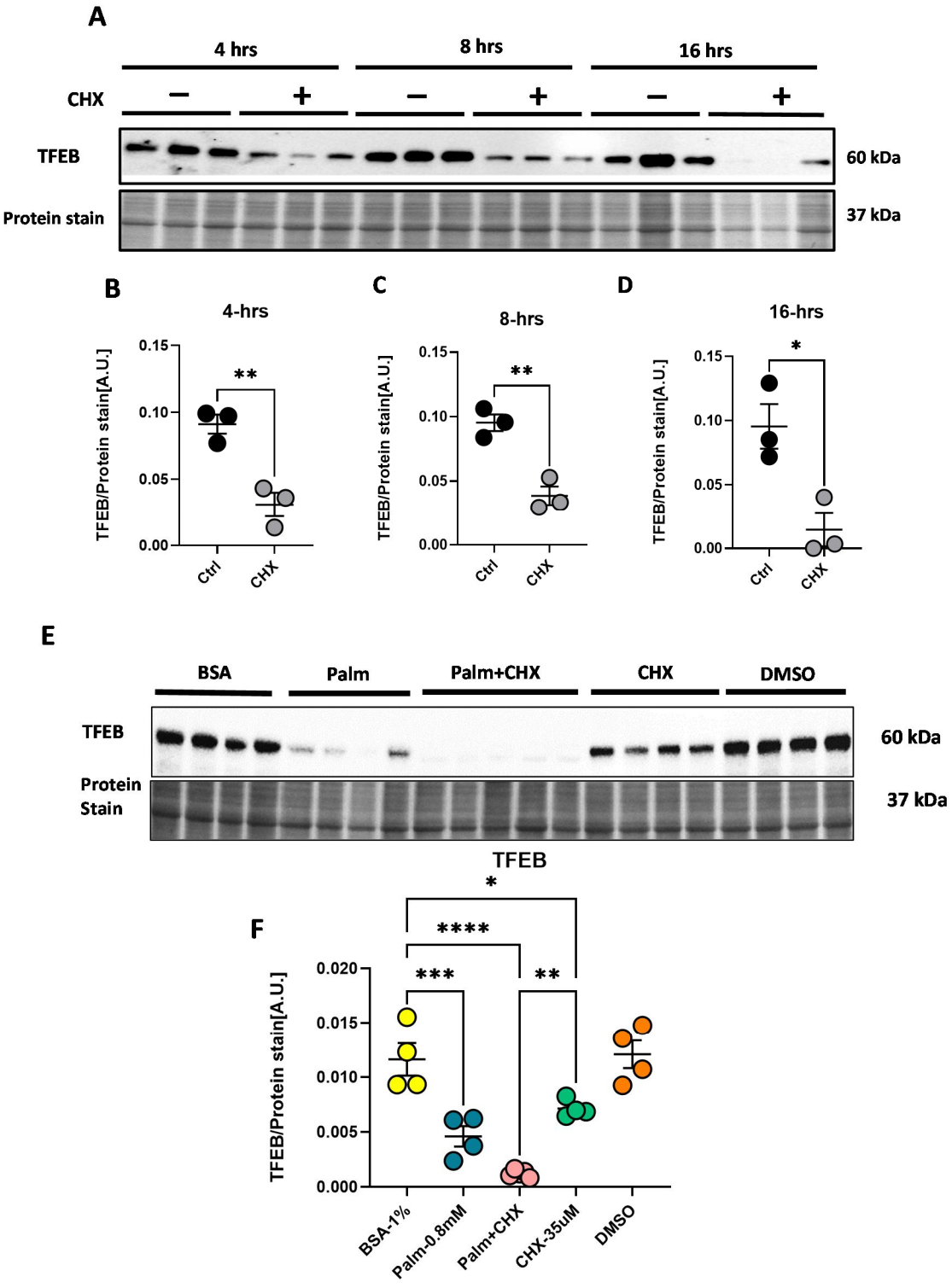

(See legend on the previous page)

3.7 Palmitate induces a decline of TFEB protein content in the presence of proteasomal inhibitor.

Proteins are degraded through the lysosome-mediated autophagy or the proteasome-mediated ubiquitin degradation pathway. To determine which of these two pathways actively degraded TFEB under the influence of palmitate, we inhibited the proteasome activity using Mg-132 and measured TFEB content. H9C2 cells were differentiated for 48 hrs and treated with 3μM Mg-132 for 4 hrs, followed by co-treatment with 0.8mM palmitate for 16 hours **(Figure 3.7 A)**.

TFEB was significantly decreased in cells treated with 0.8mM Palmitate compared to BSA-treated cells. Since Mg-132 inhibits proteasomal degradation, the cells treated with this compound showed augmented TFEB levels compared to the palmitate-treated group. However, when the cells were treated with a combination of palmitate and Mg-132, TFEB levels were not restored, indicating that TFEB does not undergo proteasomal degradation **(Figure 3.7 B-C)**. Whether increasing concentrations of Mg-132 increased TFEB content in the presence of palmitate is yet to be ascertained. Similarly, testing for TFEB protein content following the inhibition of lysosomal autophagy could provide further understating of how palmitate accelerates TFEB degradation in the myocyte.

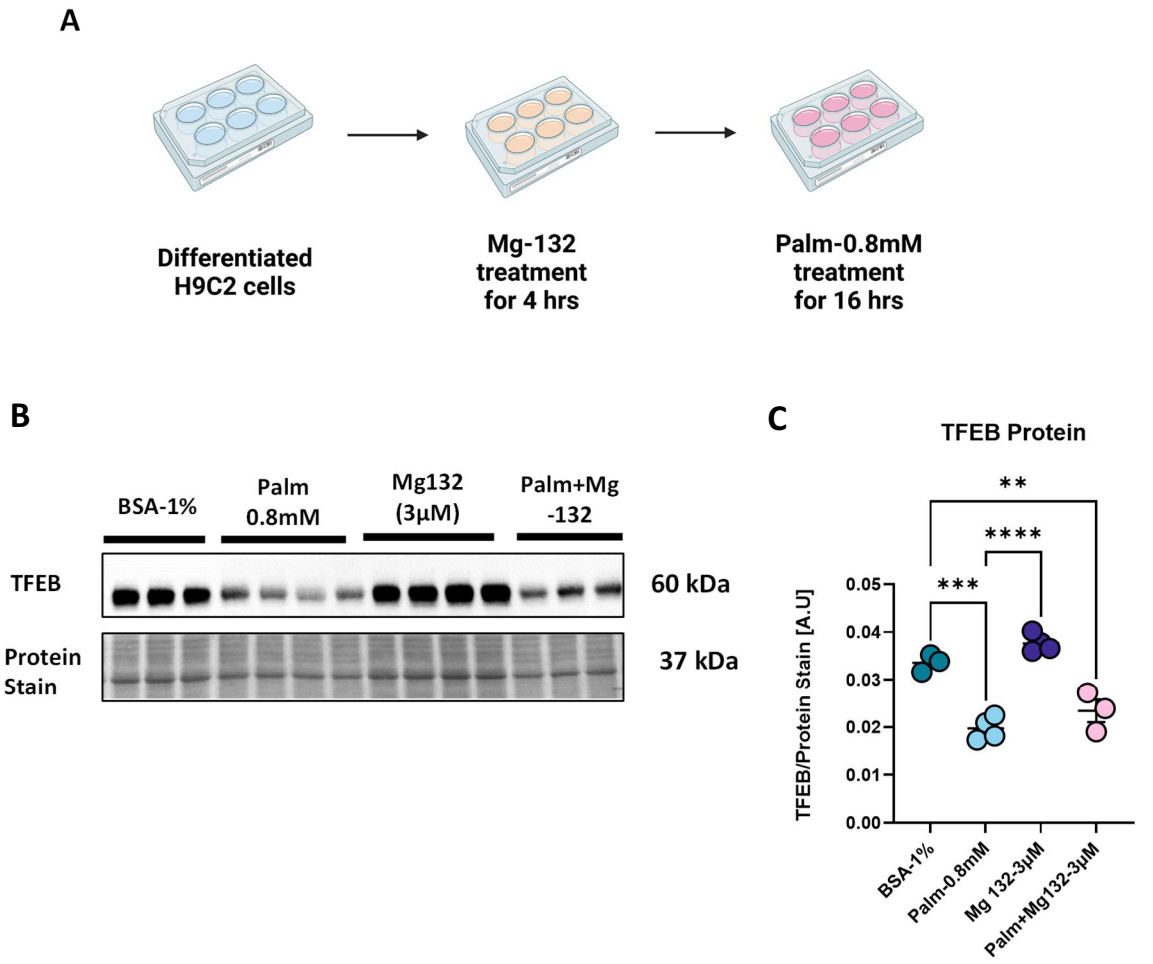

Figure 3.7 Palmitate induces a decline of TFEB protein content in the presence of proteasomal inhibitor. (A) Schematic representation of the series of treatments performed using H9C2 cells. Differentiated H9C2 cells were treated with 3µM Mg-132 for 4 hours followed by 0.8mM palmitate treatment for 16 hours prior to harvest. (B-C) Immunoblot and densitometric analysis of TFEB protein content. Data is normalized to protein stain. The graph represents mean ± S.E.M. Statistical analysis was performed using one-way ANOVA followed by Tukey's multiple comparison tests for (C), n=3-4, ***p<0.001 for BSA-1% vs 0.8mM Palm; ****p<0.0001 for 0.8mM Palm vs Mg-132-3µM; **p<0.01 for BSA-1% vs Palm+Mg-132-3µM, AU; Arbitrary Unit. Note: all the presented lanes are from the same membranes.

3.8 Differential effect of high-fat feeding on body weight gain, glucose, and insulin intolerance in male and female mice with myocyte restricted TFEB deletion.

The identity of underlying pathways engaged following the loss of TFEB in the heart and the mechanisms by which these pathways signal and reprogram cardiac metabolism and function during obesity remains unclear. The next half of my thesis examined how deficiency of TFEB in the cardiomyocyte impacted systemic metabolism, myocyte viability, nutrient signaling and cardiac function in conditions of diet-induced obesity. Our laboratory previously employed a loss-of-function approach based on a knockdown mouse model to explore the physiological role of TFEB [140]. By breeding TFEB floxed mice with CRE expressing mice under the control of cardiomyocyte-specific α-myosin heavy chain (Myh6) promoter, cardiomyocyte-specific TFEB deletion ($TFEB^{fl/fl\ Cre/-}$) were generated and $TFEB^{fl/fl\ -/-}$ mice were used as a control. Baseline characterization of $TFEB^{fl/fl\ Cre/-}$ was reported previously [140]. However, the impact of challenging $TFEB^{fl/fl\ Cre/-}$ and $TFEB^{fl/fl\ -/-}$ with DIO on systemic and cardiac metabolism and function remained undetermined.

In males and females, when compared to the low-fat diet group, both genotypes showed significant weight gain on a high-fat diet for 20 weeks **(Figure 3.8 A-D)**. Strikingly, the female mice that lacked TFEB had exacerbated weight gain on high-fat diet when compared to their high-fat diet floxed controls **(Figure 3.8 B),** suggesting that weight gain on a high-fat diet was increased in female mice with myocyte-restricted TFEB.

Both males and females of both genotypes showed significant glucose and insulin intolerance on a high-fat diet for 20 weeks compared to the low-fat diet group **(Figure 3.8 E-H)**. Interestingly, the female $TFEB^{fl/fl\ CRE/-}$ on high-fat display a trend of increasing susceptibility to glucose intolerance compared to the males, but the data was not statistically significant. **(Figure 3.8 E-H).** Overall, these results suggest that male and female mice lacking TFEB show a differential impact on body weight gain, glucose and insulin intolerance when fed high-fat.

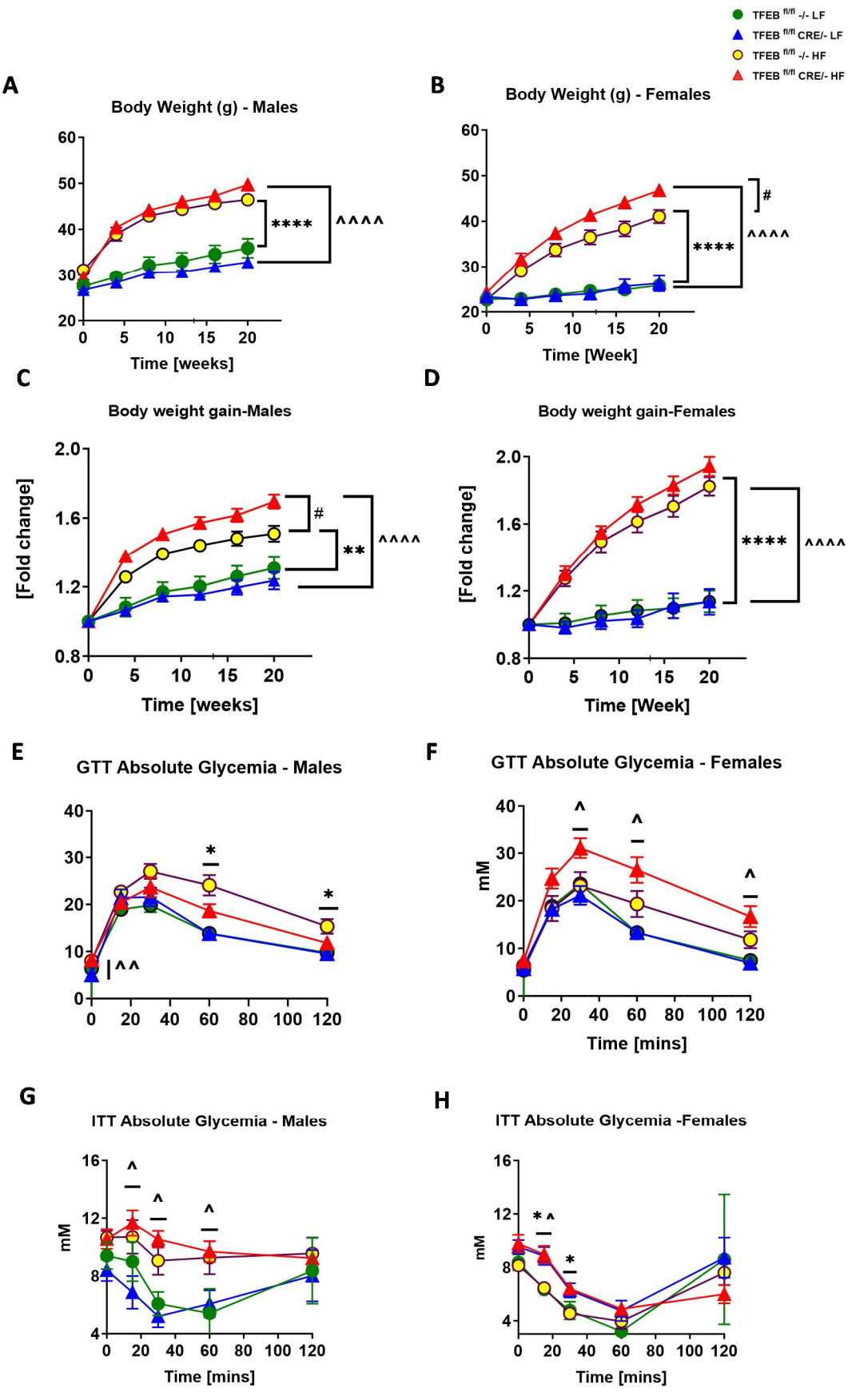
TFEB fl/fl -/- LF
TFEB fl/fl CRE/- LF
TFEB fl/fl -/- HF
TFEB fl/fl CRE/- HF
A
Body Weight (g) - Males
Time [weeks]
****
^^^^
B
Body Weight (g) - Females
Time [Week]
#
****
^^^^
C
Body weight gain-Males
[Fold change]
Time [weeks]
#
**
^^^^
D
Body weight gain-Females
[Fold change]
Time [Week]
****
^^^^
E
GTT Absolute Glycemia - Males
*
*
^^
F
GTT Absolute Glycemia - Females
mM
Time [mins]
^
^
^
G
ITT Absolute Glycemia - Males
mM
Time [mins]
^
^
^
H
ITT Absolute Glycemia -Females
mM
Time [mins]
*^
*

Figure 3.8 Differential effect of high-fat feeding on body weight gain, glucose, and insulin intolerance in male and female mice with myocyte restricted TFEB deletion. (A-B) Male and female body weight curve for 20 weeks. (C-D) Male and female body weight gain over 20 weeks represented as fold change. Glucose Tolerance Test - Absolute glycemia was noted for 0, 15, 30, 60, and 120min following intraperitoneal injection with D-glucose at 2 g/kg body weight in males (E) and females (F). Insulin Tolerance Test-absolute glycemia measured at 0, 15, 30, 60, and 120min following intraperitoneal injection with Humulin at 1 U/kg body weight in males (G) and females (H). Graph represents mean ± S.E.M., Statistical analysis was performed using Two-way ANOVA with repeated measures followed by Tukey's multiple comparison test. n-=5-15 (A-B); n=3-7 (E-H), *for $TFEB^{fl/fl\ -/-}$ LF vs $TFEB^{fl/fl\ -/-}$ HF; ^ for $TFEB^{fl/fl\ CRE/-}$ LF vs $TFEB^{fl/fl\ CRE/-}$ HF; # for $TFEB^{fl/fl\ CRE/-}$ HF vs $TFEB^{fl/fl\ -/-}$ HF, ^^^^p<0.0001; ^^^p<0.001; ^^p<0.01; ^p<0.05, ****p<0.0001; ***p<0.001; **p<0.01; *p<0.05, #p<0.05

3.9 Loss of TFEB decreases insulin-induced AKT serine phosphorylation in female but not male mice fed a high-fat diet.

I next examined if changes observed in glucose and insulin tolerance at the whole-body level are related to changes in myocyte insulin signaling since changes in cardiac insulin signaling is reported to alter whole-body glucose and lipid utilization, adiposity and energy expenditure [150]. Due to issues with breeding and time constraints, I chose $TFEB^{fl/fl\ Cre/-}$ and $TFEB^{fl/fl\ -/-}$ mice of both sexes on a high-fat diet for this experiment and did not have enough animals with a low-fat diet in this study. TFEB knockdown in adult mouse cardiomyocytes was confirmed at both protein and mRNA levels **(Figure 3.9 G-J).**

Ex vivo insulin stimulation studies in cardiomyocytes revealed significant decreases in insulin-induced AKT phosphorylation at Ser473 in female $TFEB^{fl/fl\ CRE/-}$ on high-fat diet when compared to the floxed controls **(Figure 3.9 B-C),** an effect not observed in male mice lacking myocyte TFEB **(Figure 3.9 E-F)**. Insulin-induced AKT phosphorylation at Thr308 remained unchanged across genotypes and between sexes **(Figure 3.9 A, C, F**). These findings suggest that systemic changes observed in glucose and insulin tolerance in response to high-fat diet feeding is plausibly attributed to differences in myocyte insulin signaling in female mice lacking TFEB but not necessarily male with myocyte specific TFEB deletion, pointing to sexual dimorphisms in insulin signaling and sensitivity following the loss of TFEB.

(See figure on the next page)

Figure 3.9. Loss of TFEB decreases insulin-induced AKT serine phosphorylation in female but not male mice fed high-fat diet. AMCMs were isolated and treated with 100nM insulin for 15 mins prior to harvesting. Immunoblot and densitometric analysis p-T AKT s473 and p-AKT T308 in females (A-C) and males (D-F) normalized to total AKT. Immunoblot and densitometric analysis of TFEB normalized to protein stain (G-I). mRNA analysis of TFEB – values normalized to mHPRT-1 and mRPL-27 reference genes (J). The graph represents mean ± S.E.M. Statistical analysis was performed using unpaired t-test for (B,C,E,F,H,I,J), **p<0.01 for $TFEB^{fl/fl\ CRE/-}$ LF vs $TFEB^{fl/fl\ CRE/-}$ HF, n=3; ****p<0.0001 for $TFEB^{fl/fl\ -/-}$ vs $TFEB^{fl/fl\ CRE/-}$, n=13 (J); AU; Arbitrary Unit. Note: all the presented lanes are from the same membranes.

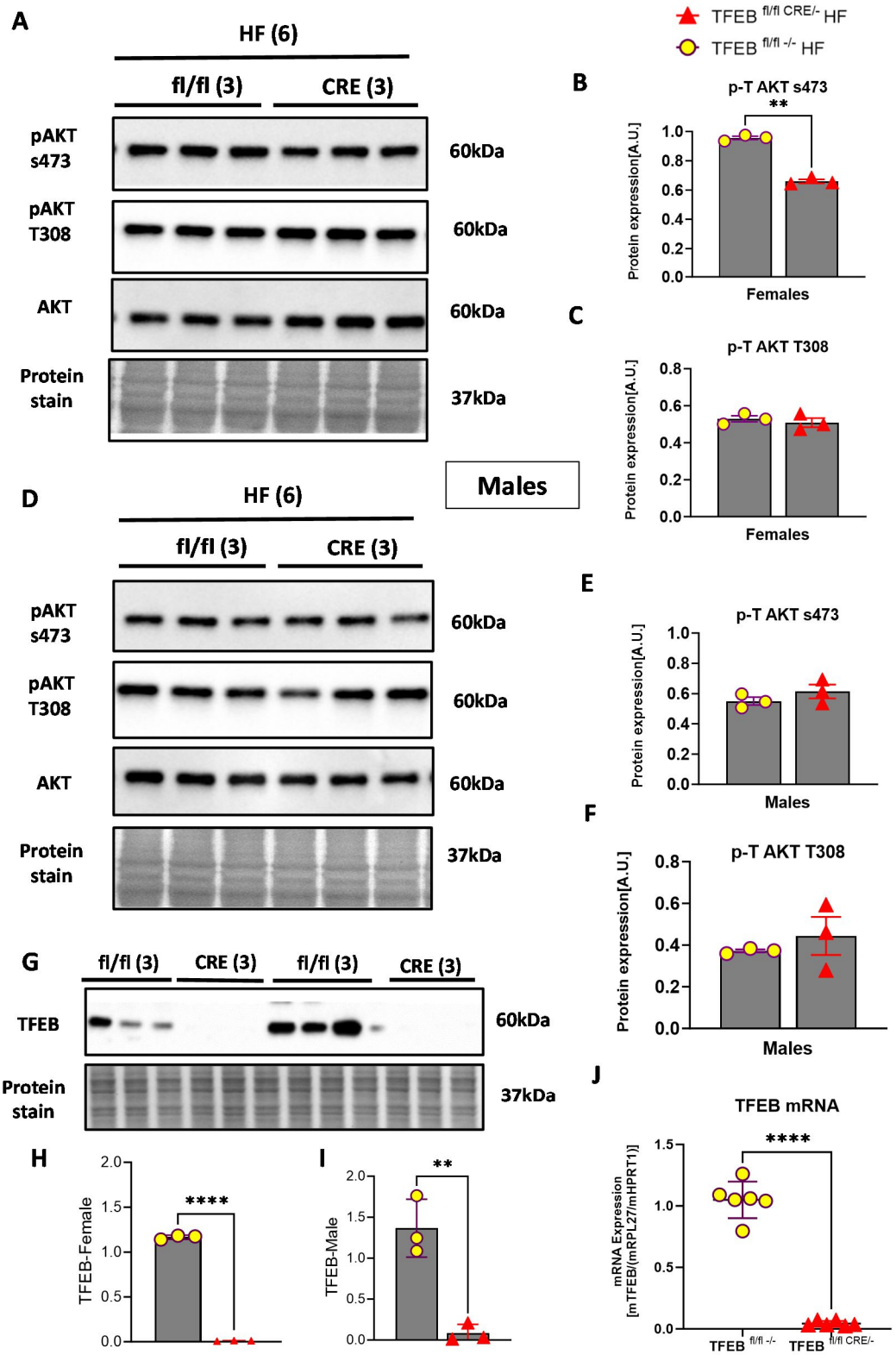

(See legend on the previous page)

3.10 Cardiomyocyte-specific TFEB deletion increased lipid droplet accumulation in high-fat diet-fed mice.

Mitochondrial dysfunction is reported to be an outcome of TFEB inaction, as TFEB regulates genes involved in mitochondrial energy metabolism, biogenesis and function [119]. Moreover, changes in myocyte insulin signaling could alter mitochondrial metabolism and function. Indeed, previous data from our lab involving transcriptome analysis in $TFEB^{fl/fl\ CRE/-}$ cardiomyocytes revealed that loss of TFEB induces differential expression of genes involved in lipid synthesis, uptake, lipolysis and storage [140]. Consequently, my initial investigation focused on studying the impact of TFEB deletion on cardiomyocyte lipid storage during diet-induced obesity.

As anticipated, the presence of oleate induced a notable increase in lipid droplet accumulation (represented as the area of the cardiomyocyte covered with lipid droplets) in cardiomyocytes isolated from $TFEB^{fl/fl\ CRE/-}$ mice compared to the lipid droplets observed in $TFEB^{fl/fl\ -/-}$ mice fed with a high-fat diet. **(Figure 3.10 A-C).** The findings from these experiments indicate that the deletion of TFEB, specifically in the heart, leads to increased lipid storage, which, likely, is a consequence of remodeled cardiac lipid metabolism during diet-induced obesity in the absence of TFEB.

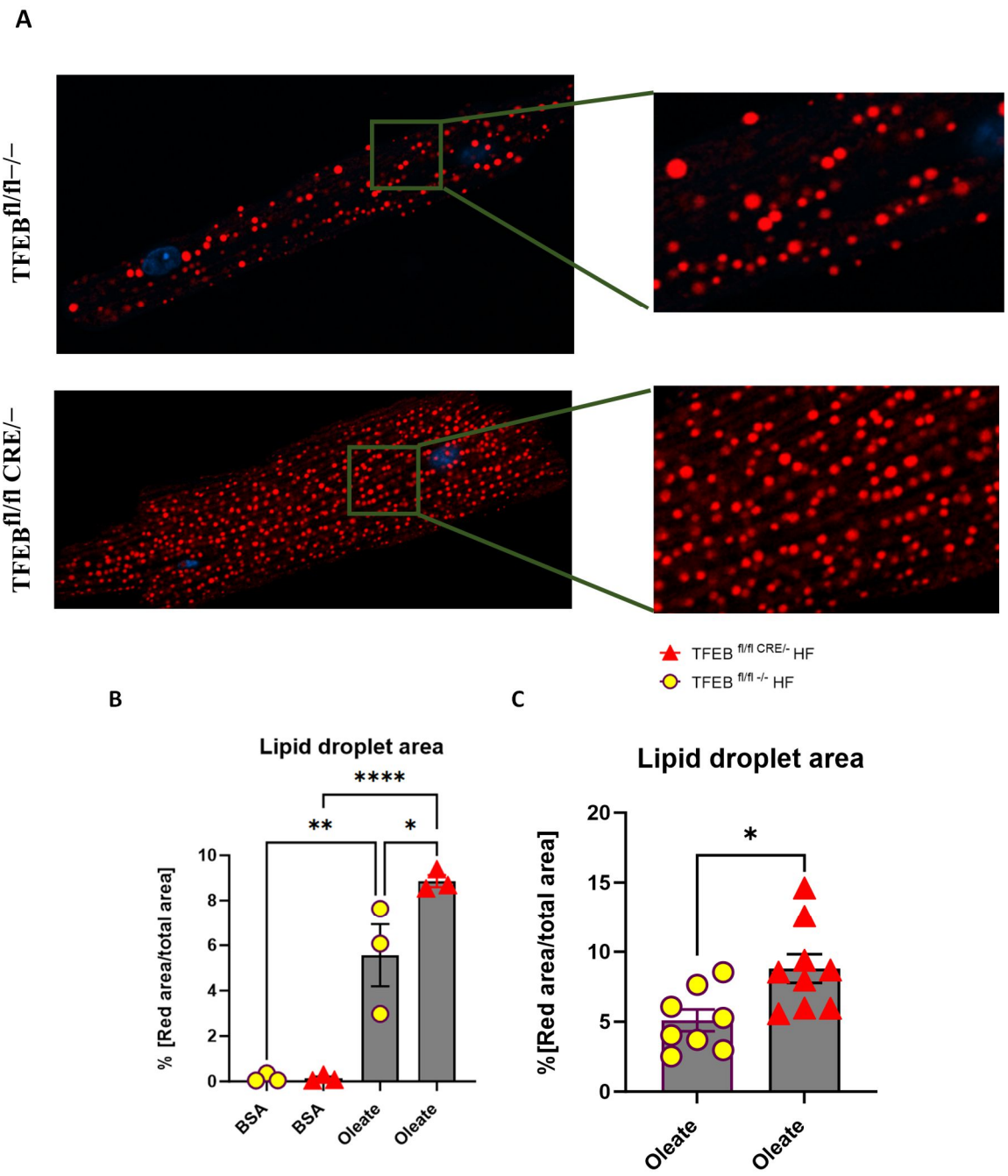

Figure 3.10 Cardiomyocyte-specific TFEB deletion increased lipid droplet accumulation in high-fat diet-fed mice. (A) Lipid droplet images were obtained using super-resolution microscopy. (B) Represents the percentage of lipid droplet area in BSA and oleate-treated AMCMs. (C) Percentage of area covered with lipid droplets in oleate-treated AMCMs. The graph represents mean ± S.E.M., Statistical analysis was performed using either unpaired t-test, n=3 (C) or one-way ANOVA with Tukey's multiple comparisons test for, n=11 (B), *P<0.05, **P<0.01, ****P <0.0001.

3.11 Myocyte-restricted TFEB deletion suppressed mitochondrial fatty acid-linked respiration in high-fat diet-fed mice.

The restriction of TFEB, leading to increased lipid accumulation in the heart, indicates a potential decrease in the flux of FA towards mitochondrial oxidation. To test this hypothesis, I examined FA-linked mitochondrial respiration levels in cardiomyocytes of mice that lacked TFEB with or without diet-induced obesity.

Adult mouse cardiomyocytes were permeabilized in the oxygraph chamber using saponin prior to the sequential addition of different electron transport substrates and inhibitors **(Figure 3.11 A)** to obtain a representative trace, as outlined in **Figure 3.11 B**. Due to issues with breeding and time constraints, I chose $TFEB^{fl/fl\ Cre/-}$ and $TFEB^{fl/fl\ -/-}$ male mice on high-fat diets for this experiment and did not have enough female animals on low and high-fat diets in this study. When normalized to protein and corrected to the respiration observed after the addition of Antimycin A, FA oxidation was seen to be significantly suppressed in cardiomyocytes isolated from male mice on a high-fat diet that lacked TFEB compared to their respective floxed controls on high-fat **(Figure 3.11 C-D).** Therefore, these results suggest that TFEB deficiency exacerbates lipotoxicity by diverting the FA flux from oxidation to storage.

A

Compound	Concentration	Mark
Malate	0.5mM	M
Palmitoylcarnitine	50μM	Pal
ADP	0.1mM	D 0.1
ADP	0.5mM	D 0.5
ADP	5mM	D 5
Octanoyl-carnitine	0.2mM	Oct
FCCP	0.5μM	FCCP
Rotenone	0.5μM	R
Succinate	10μM	S
Antimycin A	5μM	AmA

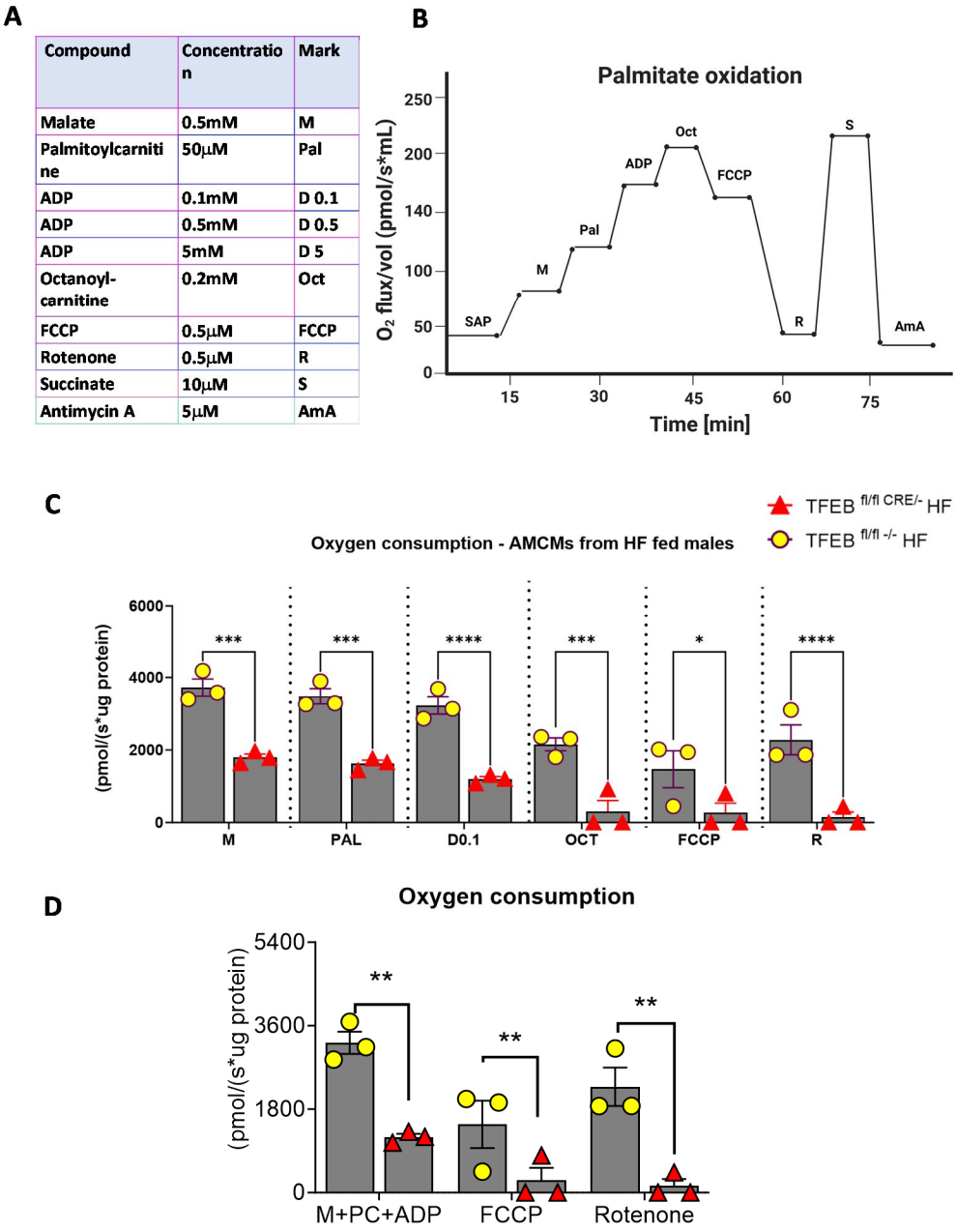

Figure 3.11 Myocyte-restricted TFEB deletion suppressed mitochondrial fatty acid-linked respiration in high-fat diet-fed mice. (A) List and concentration of substrates and inhibitors added to the oxygraph chamber sequentially. (B) Sample trace of oxygen flux in isolated AMCMs. (C-D) Oxygen consumption measured in AMCMs isolated from HF-fed males. The graph represents mean ± S.E.M., Statistical analysis was performed using two-way ANOVA with Sidak's multiple comparisons test, *P<0.05, **P<0.01, ***P<0.001, ****P <0.0001. Data represents n = 3.

3.12 Cardiac function remodeling following diet-induced obesity is exacerbated in mice with cardiomyocyte-specific TFEB insufficiency.

Since our data showed that the loss of TFEB precipitates a decline in mitochondrial function and changes in the whole body and cell-autonomous insulin action, we posit that TFEB insufficiency perturbs cardiovascular function during obesity. Cardiac Doppler analysis was performed in anesthetized mice fed at the 18th week of the diet feeding. Diastolic function was determined by analyzing the mitral inflow pattern, while the systolic function was determined by assessing the aortic outflow pattern. Measurements included the peak early (E-wave) and late (A-wave) inflow velocities followed by E/A ratio calculation. In both males and females, TFEB $^{fl/fl\ CRE/-}$ fed high-fat diet had a significantly higher E/A ratio when compared to a low-fat diet in both males **(Figure 3.12 A)** and females **(Figure 3.12 D)**. Strikingly in males, TFEB $^{fl/fl\ CRE/-}$ fed high-fat diet had significantly increased E/A ratio compared to their TFEB $^{fl/fl\ -/-}$ controls also on high-fat **(Figure 3.12 A)**, a difference not observed in females.

I also examined the markers of diastolic dysfunction; isovolumetric contraction, and relaxation time (IVCT and IVRT, respectively). The IVCT were significantly higher in TFEB $^{fl/fl\ CRE/-}$ fed high-fat compared to low-fat in both males **(Figure 3.12 B)** and females **(Figure 3.12 E).** Interestingly**,** in females but not in males fed with high-fat, TFEB $^{fl/fl\ CRE/-}$ mice had increased IVCT values when compared to TFEB $^{fl/fl\ -/-}$ group **(Figure 3.12 E)**. Similar to IVCT, the IVRT was significantly higher in high-fat fed TFEB $^{fl/fl\ CRE/-}$ compared to their controls in both males **(Figure 3.12 C)** and females **(Figure 3.12 F).** Moreover, the floxed male mice fed with high-fat had significantly higher IVRT compared to the floxed mice fed with low-fat, a difference not observed in females. **(Figure 3.12 C, F)**.

s

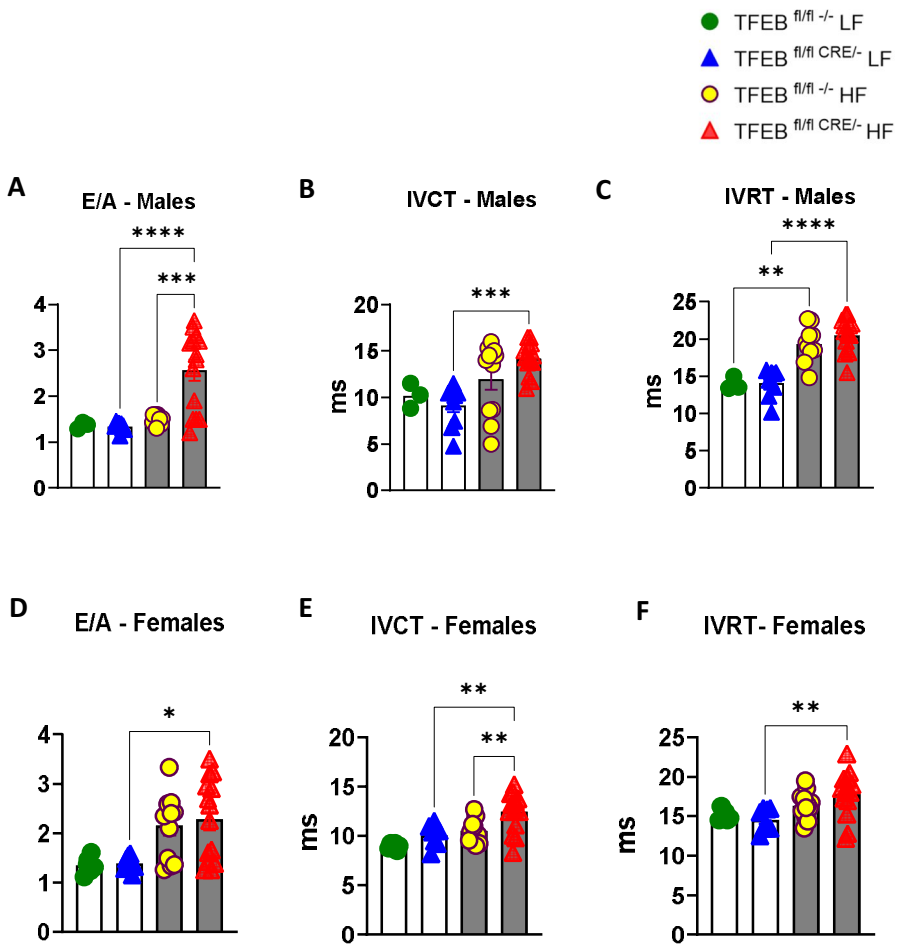

Figure 3.12 Cardiac function remodeling following diet-induced obesity is exacerbated in mice with cardiomyocyte-specific TFEB insufficiency. Ratio of E-wave peak velocity and A-wave peak velocity (EPV/APV) in males (A) and females (D). Isovolumetric contraction time (IVCT) in males (B) and females (E). Isovolumetric relaxation time (IVRT) measured in males (C) and females (F). These Doppler flow observations were made during the 18th week of diet feeding following isoflurane-induced anesthesia. The graph represents mean ± S.E.M., n=3-14. Statistical analysis was performed using One-way ANOVA followed by Tukey's multiple comparison test, ****p<0.0001 for TFEB$^{fl/fl\ CRE/-}$ LF vs TFEB$^{fl/fl\ CRE/-}$ HF and ***p<0.001 for TFEB$^{fl/fl\ -/-}$ HF vs TFEB$^{fl/fl\ CRE/-}$ HF (A); ***p<0.001 for TFEB$^{fl/fl\ CRE/-}$ LF vs TFEB$^{fl/fl\ CRE/-}$ HF (B); **p<0.01 for TFEB$^{fl/fl\ -/-}$ LF vs TFEB$^{fl/fl\ -/-}$ HF and ****p<0.0001 for TFEB$^{fl/fl\ CRE/-}$ LF vs TFEB$^{fl/fl\ CRE/-}$ HF (C); *p<0.05 for TFEB$^{fl/fl\ CRE/-}$ LF vs TFEB$^{fl/fl\ CRE/-}$ HF (D); **p<0.01 for TFEB$^{fl/fl\ CRE/-}$ LF vs TFEB$^{fl/fl\ CRE/-}$ HF and **p<0.01 for TFEB$^{fl/fl\ -/-}$ HF vs TFEB$^{fl/fl\ CRE/-}$ HF (E); **p<0.01 for TFEB$^{fl/fl\ CRE/-}$ LF vs TFEB$^{fl/fl\ CRE/-}$ HF (F).

3.13 Cardiomyocyte-specific TFEB deletion increased atrial weight to tibia length ratio in both sexes however, ventricular weight to tibia length ratio increases in male mice following high-fat diet-feeding.

Morphometric analysis of the hearts isolated from the high-fat and low-fat fed mice included measuring atrial and ventricle weights corrected to tibial lengths. In males and females, TFEB $^{fl/fl\ CRE/-}$ mice on high-fat had significantly higher atrial weight to tibia length ratios when compared to TFEB $^{fl/fl\ CRE/-}$ on low-fat **(Figure 3.13 A-B)**. Furthermore, TFEB $^{fl/fl\ CRE/-}$ on high-fat had increased atrial weights to tibial length ratio compared to TFEB $^{fl/fl\ -/-}$ **(Figure 3.13 A-B),** suggesting that loss of TFEB exacerbated atrial weight gain following high-fat diet feeding. Surprisingly, the ventricular weight to tibial length ratio was increased only in high-fat diet-fed male mice with loss of TFEB **(Figure 3.13 C)**, an effect not observed in female mice across genotypes and diets **(Figure 3.13 D)**. Together, these results indicate that TFEB insufficiency during obesity precipitates chamber-specific hypertrophy in a sex-dependent manner suggesting that male mice lacking TFEB are more susceptible to high-fat diet-induced cardiac hypertrophy.

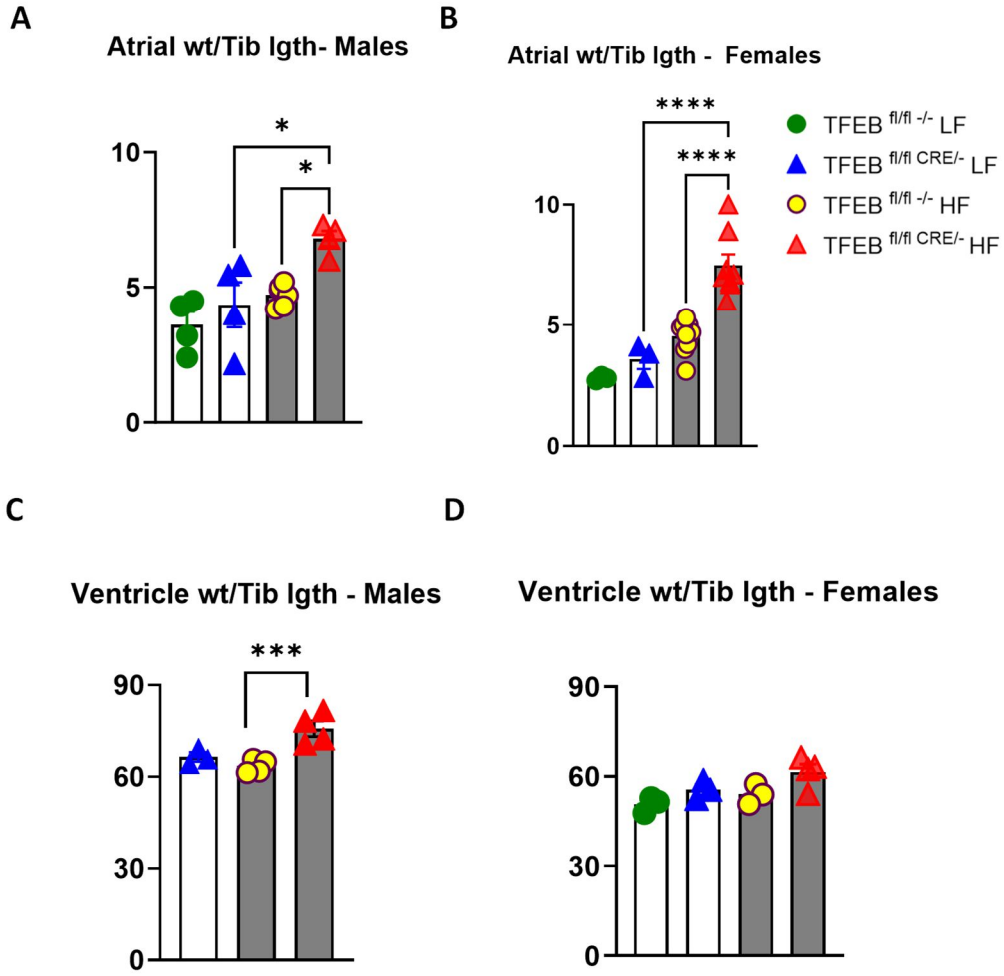

Figure 3.13 Cardiomyocyte-specific TFEB deletion increased atrial weight to tibia length ratio in both sexes however ventricular weight to tibia length ratio is increased in male mice following high-fat diet-feeding. (A) represents the ratio of atrial weight(mg) and tibia length(cm) in males. (B) represents the ratio of atrial weight(mg) and tibia length(cm) in females. (C) The ratio of ventricle weight(mg) and tibia length(cm) in males. (D) The ratio of ventricle weight(mg) and tibia length(cm) in females. These observations were made at the end of 20-week diet period post-decapitation. Graph represents mean ± S.E.M., n=3-11; Statistical analysis was performed using One-way ANOVA followed by Tukey's multiple comparison test, *p<0.05 for TFEB $^{fl/fl\ CRE/-}$ LF vs TFEB $^{fl/fl\ CRE/-}$ HF and *p<0.05 for TFEB $^{fl/fl\ -/-}$ HF vs TFEB $^{fl/fl}$ CRE/- HF (A)****p<0.0001 for TFEB $^{fl/fl\ CRE/-}$ LF vs TFEB $^{fl/fl\ CRE/-}$ HF and ****p<0.0001 for TFEB $^{fl/fl\ -/-}$ HF vs TFEB $^{fl/fl\ CRE/-}$ HF (B) ***p<0.001 for TFEB $^{fl/fl\ -/-}$ HF vs TFEB $^{fl/fl\ CRE/-}$ HF (C).

3.14 Loss of TFEB increased calcium transient amplitude in high-fat fed mice.

Since TFEB insufficiency during lipotoxicity and diet-induced obesity altered insulin signaling, mitochondrial metabolism and cardiac function, I queried if changes in calcium handling could be a cause or consequence of these changes. Indeed, lipotoxicity increases ROS, which oxidizes membrane lipids in organelles, disrupting Ca^{2+}-led excitation-contraction coupling and inducing cell death. Moreover, our Ca^{2+} transient analysis in unchallenged $TFEB^{fl/fl\ Cre/-}$ cardiomyocytes has revealed an increase in Ca^{2+} transient amplitude compared to $TFEB^{fl/fl\ -/-}$ cardiomyocytes (indicating greater SR release), along with a decrease in the time constant of 50% and 80% Ca^{2+} decay (indicating an increased rate of SR re-uptake by SERCA and extrusion by NCX respectively) and lower Ca^{2+} at peak relaxation (indicating lower diastolic Ca^{2+}). Our preliminary data indicate that in unchallenged mice, TFEB deficiency results in adaptive changes in Ca^{2+} handling, however, the mechanisms underlying Ca^{2+} handling changes and whether Ca^{2+} handling becomes impaired in $TFEB^{fl/fl\ Cre/-}$ mice challenged with DIO were unknown.

A significant increase in intracellular Ca^{2+} during contraction (Max Ca) at 0.5, 1, 1.5 and 2 Hz was observed in high-fat fed $TFEB^{fl/fl\ CRE/-}$ compared to the $TFEB^{fl/fl-/-}$ **(Figure 3.14 B).** On the other hand, there was no change observed in Ca^{2+} during relaxation (Min Ca) **(Figure 3.14 A).** Furthermore, there was a significant increase in Ca^{2+} transient amplitude (ΔCa) in cardiomyocytes from $TFEB^{fl/fl\ CRE/-}$ mice compared to $TFEB^{\ fl/fl-/-}$ mice **(Figure 3.14 C)**. A high Ca^{2+} transient amplitude in $TFEB^{fl/fl\ CRE/-}$ mice was further associated with an increase in peak rate of rise $[Ca^{2+}]_i$ during contraction ($+dCa/dt_{max}$) and increased rate of removal of Ca^{2+} during relaxation ($-dCa/dt_{min}$) compared to the floxed controls **(Figure 3.14 D-E)**. Next, time to 50% Ca^{2+} decay resulting from Ca^{2+} sequestration into SR via SERCA was similar among the two groups **(Figure 3.14 F).** However, time to 80% Ca^{2+}decay, which represents the Ca^{2+} removal from the cytoplasm to the extracellular space through the NCX during the late part of the relaxation, was significantly high at 0.5 Hz in $TFEB^{fl/fl\ CRE/-,}$ indicating a delayed decay during lower frequency **(Figure 3.14 G)**. Increased 80% decay times were also observed in female cardiomyocytes lacking TFEB when paced at 0.5Hz compared to the $TFEB^{fl/fl-/-}$ **(Figure 3.15 G).** Finally, the time constant of $[Ca^{2+}]_i$ transients were significantly lower in $TFEB^{fl/fl}$

$^{CRE/-}$ at 2 Hz compared to the floxed controls in males **(Figure 3.14 H).** Whereas, in females, $TFEB^{fl/fl\ CRE/-}$ mice had increased decay time constants (Ca^{2+} Tau decay) at 0.5 Hz compared to $TFEB^{fl/fl-/-}$ **(Figure 3.15 H).** No other significant difference in Ca^{2+} levels during relaxation and contraction was observed in females **(Figure 3.15)**.

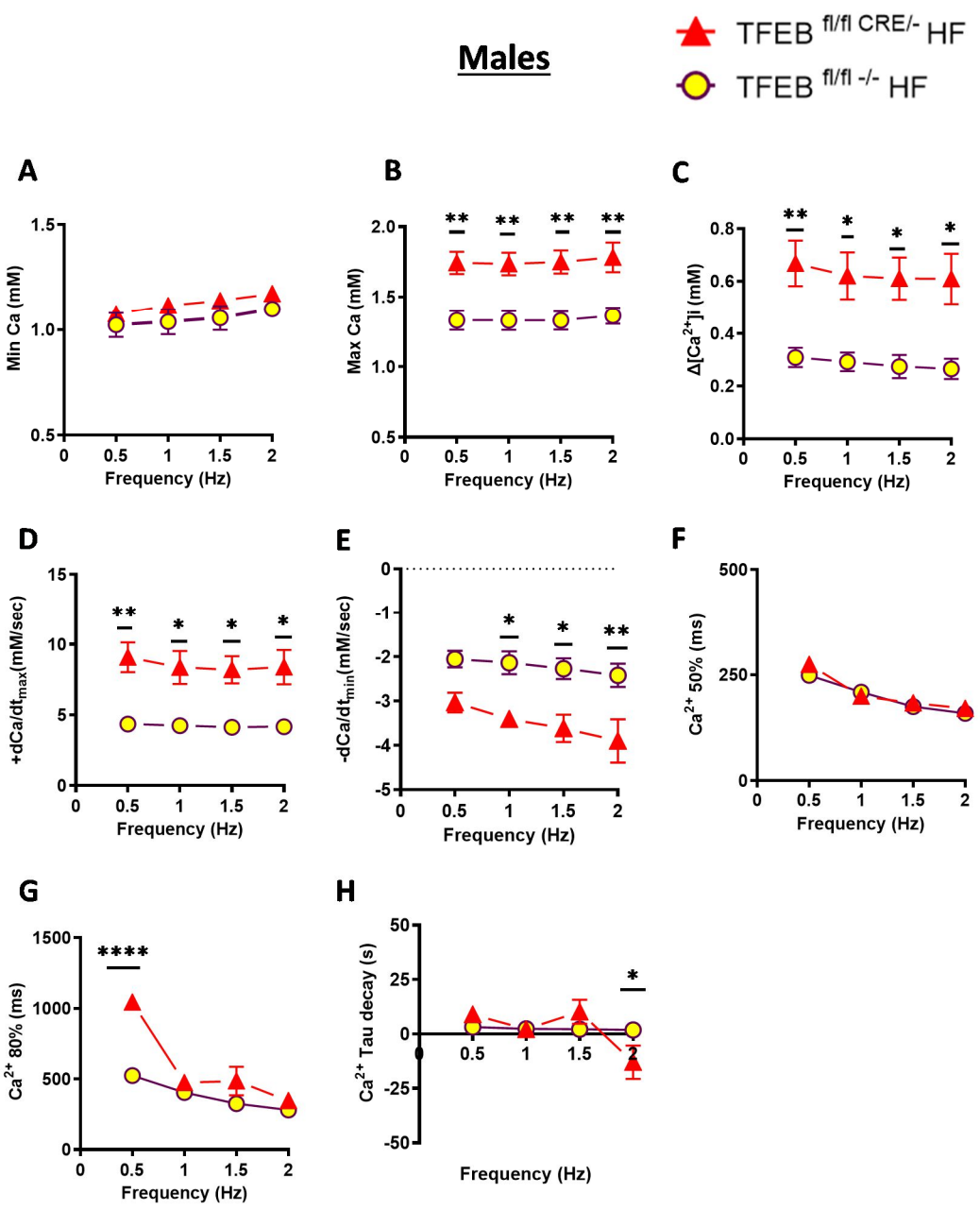

Figure 3.14 Loss of TFEB increased calcium transient amplitude in high-fat male fed mice. (A) Intracellular Ca^{2+} during relaxation, (B) intracellular Ca^{2+} during contraction, (C) change in intracellular Ca^{2+} from the peak of relaxation to the peak of contraction, (D) rate of maximum Ca^{2+} transient, (E) rate of maximum Ca^{2+} decay, (F) time to 50% and (G) time to 80% Ca^{2+} removal decay and (H) time constant of intracellular Ca^{2+} decay in isolated cardiomyocytes. The graph represents mean ± S.E.M., n = 3 mice. Statistical analysis was performed using two-way ANOVA followed by Sidak's multiple comparison test. *P<0.05, **P<0.01 for $TFEB^{fl/fl\ -/-}$ HF vs $TFEB^{fl/fl\ CRE/-}$ HF.

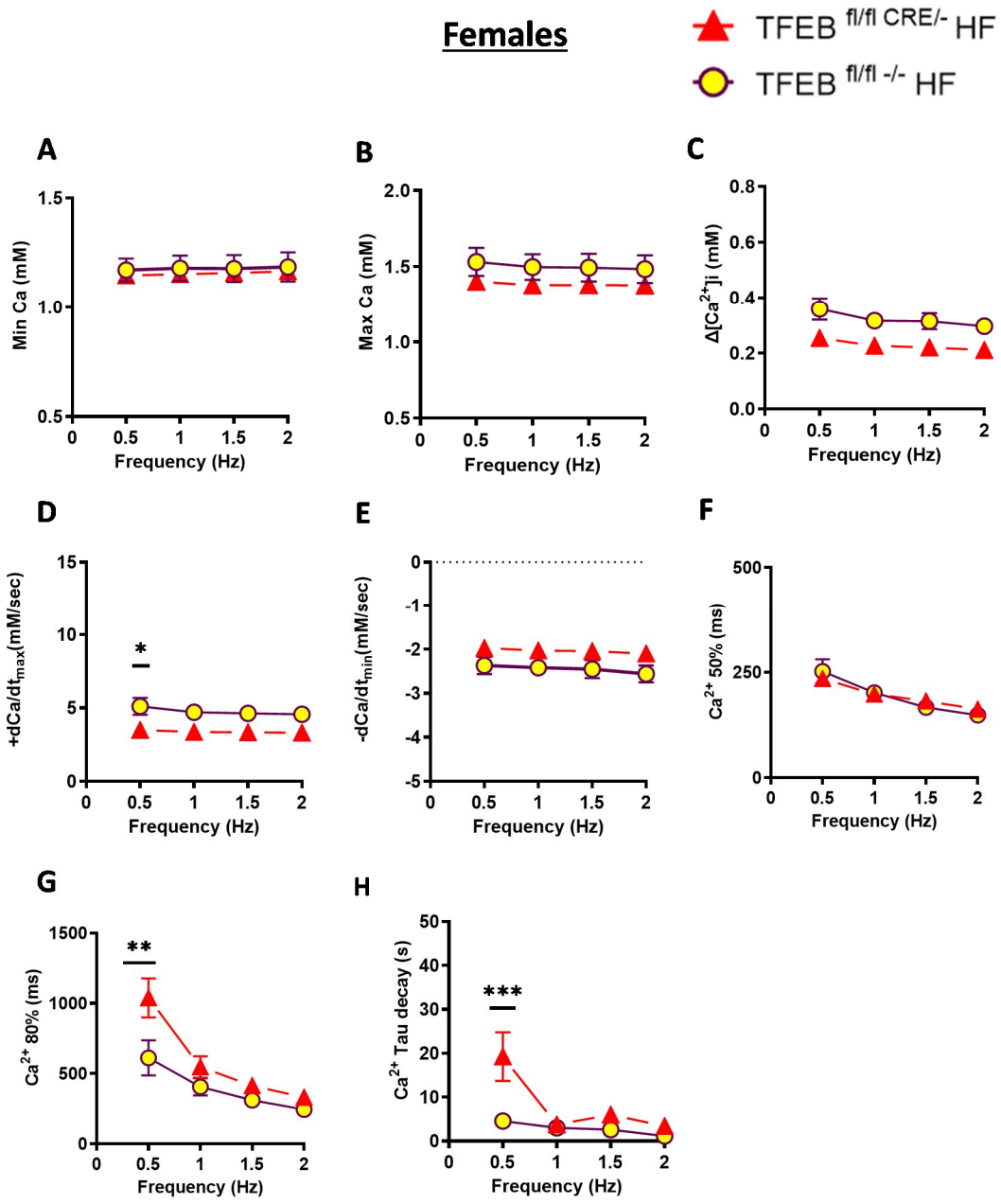

Figure 3.15 Loss of TFEB increased altered calcium dynamics in high-fat fed female mice. (A) Intracellular Ca^{2+} during relaxation, (B) intracellular Ca^{2+} during contraction, (C) change in intracellular Ca^{2+} from the peak of relaxation to the peak of contraction, (D) rate of maximum Ca^{2+} transient, (E) rate of maximum Ca^{2+} decay, (F) time to 50% and (G) time to 80% Ca^{2+} removal decay and (H) time constant of intracellular Ca^{2+} decay in isolated cardiomyocytes. The graph represents mean ± S.E.M., n = 3 mice. Statistical analysis was performed using two-way ANOVA followed by Sidak's multiple comparison test. *P<0.05, **P<0.01, ***P<0.001 for TFEB $^{fl/fl\ -/-}$ HF vs TFEB $^{fl/fl\ CRE/-}$ HF.

3.15 Cardiomyocyte sarcomere length is altered in high-fat-fed male but not female TFEB knockouts.

Next, I examined if the changes in Ca^{2+} transient/dynamics following the loss of TFEB is associated with changes in cardiomyocyte contractile properties during obesity. Contrary to our expectations, unpublished data from our laboratory showed that in unchallenged conditions, alterations in Ca^{2+} transient amplitude did not alter sarcomere length during contraction and relaxation in $TFEB^{fl/fl\ CRE/-}$ cardiomyocytes compared to $TFEB^{fl/fl-/-}$ cardiomyocytes.

Adult mouse cardiomyocytes from male and female high-fat diet-fed animals from both genotypes were isolated and electrically paced using a myopacer at 0.5, 1, 1.5, and 2 Hz to record the sarcomere length. Sarcomere length was significantly increased in male $TFEB^{fl/fl\ CRE/-}$ mice during contraction (Min SL) at 1, 1.5 and 2 Hz **(Figure 3.16 A)**. However, no change was observed in sarcomere length during relaxation (Max SL) in both males **(Figure 3.16 B)** and females **(Figure 3.17 B)**. No difference was observed in sarcomere length from the peak relaxation to peak contraction (ΔSL) **(Figure 3.16 C, 3.17 C).** Similarly, the rate of velocity of cardiomyocyte contraction ($-dSL/dt_{min}$) and relaxation ($+dSL/dt_{max}$) also remained unaltered among the genotypes and the sexes **(Figure 3.16 D-E, 3.17 D-E).** Moreover, the time to reach peak contraction (Time to min SL) were also unchanged **(Figure 3.16 F, 3.17 F).** Together, these findings suggest that in the absence of metabolic stress, despite exhibiting higher Ca^{2+} transient amplitude, $TFEB^{fl/fl\ CRE/-}$ cardiomyocytes did not display a change in contractile properties and were able to contract as efficiently as $TFEB^{fl/fl\ -/-}$ cardiomyocytes. However, during obesity in male mice lacking TFEB, increased Ca^{2+} transient amplitude is observed, which corresponded with altered sarcomere length, an effect not observed in the females.

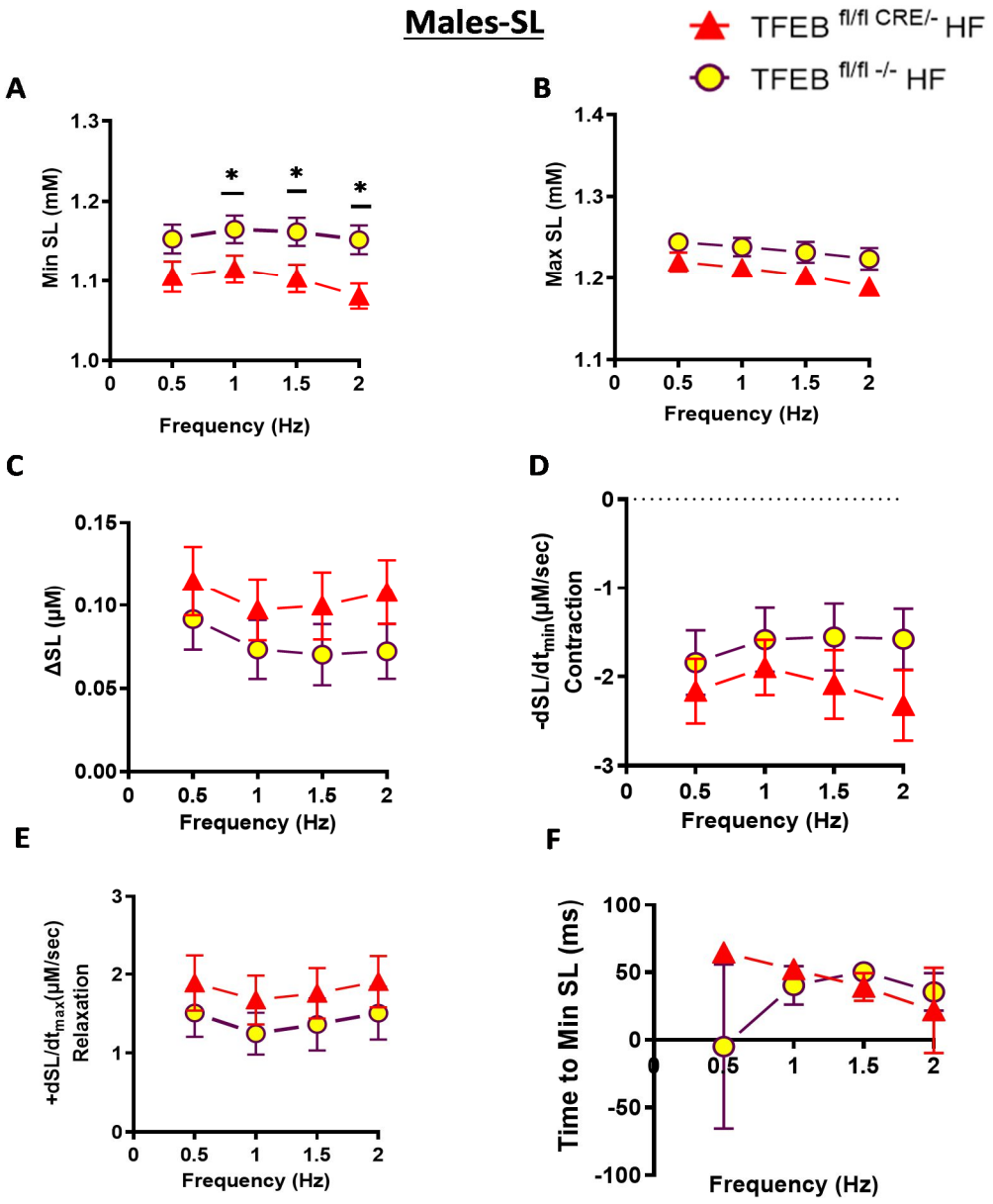

Figure 3.16 Cardiomyocyte sarcomere length is altered in high-fat-fed male TFEB knockouts. Cardiomyocyte contractility was evaluated from male TFEB$^{fl/fl\ -/-}$ HF and TFEB$^{fl/fl\ CRE/-}$ HF. (A) Sarcomere length (SL) during contraction, (B) SL during relaxation, (C) change in SL from the peak of contraction to the peak of relaxation, (D) rate of velocity of cardiomyocyte contraction, (E) rate of velocity of cardiomyocyte relaxation and (F) time to reach peak contraction in isolated cardiomyocytes. The graph represents mean ± S.E.M, n = 10. Statistical analysis was performed using two-way ANOVA followed by Sidak's multiple comparison test. *P<0.05 for TFEB$^{fl/fl\ -/-}$ HF ^{vs} TFEB$^{fl/fl\ CRE/-}$ HF (A).

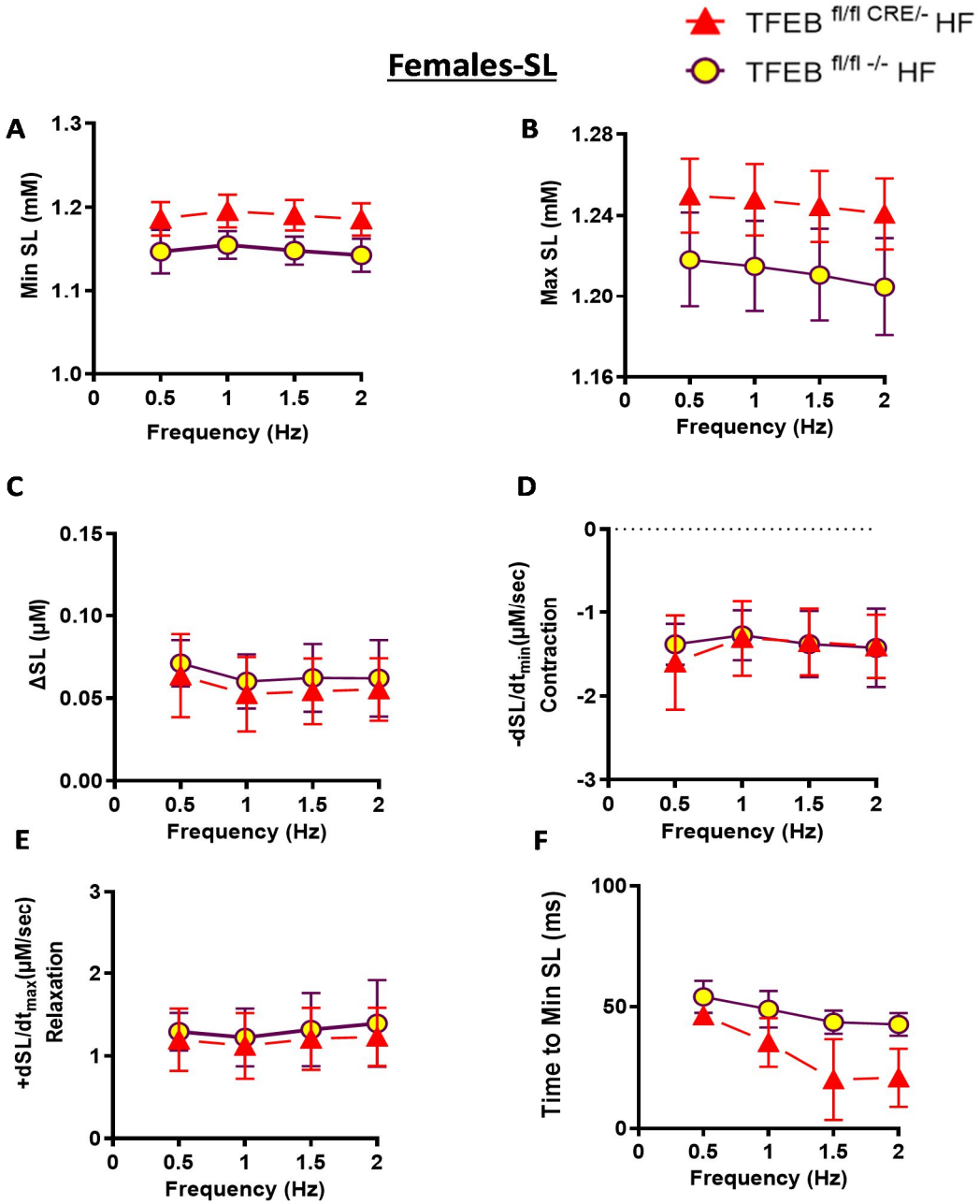

Figure 3.17 Cardiomyocyte sarcomere length is unaltered in female TFEB$^{fl/fl\ CRE/-}$ mice on high-fat. Cardiomyocyte contractility was evaluated from female TFEB$^{fl/fl\ -/-}$ HF and TFEB$^{fl/fl\ CRE/-}$ HF. (A) Sarcomere length (SL) during contraction, (B) SL during relaxation, (C) change in SL from the peak of contraction to the peak of relaxation, (D) rate of velocity of cardiomyocyte contraction, (E) rate of velocity of cardiomyocyte relaxation and (F) time to reach peak contraction in isolated cardiomyocytes. The graph represents mean ± S.E.M., n = 6-7 mice. Statistical analysis was performed using two-way ANOVA followed by Sidak's multiple comparison test.

3.16 Cardiomyocyte-specific TFEB insufficiency did not alter contractile proteins following diet-induced obesity.

Changes in intracellular Ca^{2+} handling could be accompanied by altered myofilament Ca^{2+} sensitivity, affecting contractile function [151]. To clarify if any of these contractile proteins that form the sarcomere are differentially phosphorylated in the TFEB knockouts and floxed mice, myofilaments were isolated from low and high-fat diet fed TFEB $^{fl/fl\ CRE/-}$ and TFEB $^{fl/fl-/-}$ mice. Sarcomeres are composed of long proteins that are organized into thick (contain myosin) and thin filaments (contain actin), which, when slide against each other, cause contraction and relaxation of the cardiac muscle.

Myofilaments were isolated from whole heart tissues using K60 buffer, and the lysates were used for phosphoprotein staining using Pro-Q diamond, followed by overnight Coomassie-Blue staining. The bands imaged after Pro-Q diamond staining were quantified and normalized to the lane volumes obtained from Coomassie-Blue staining **(Figure 3.18 A-B)**.

Quantified bands included – Myosin Heavy Chain (MHC), a contractile protein in the sarcomeric thick filament **(Figure 3.18 C)**; Myosin Light Chain-2 (MLC-2) which regulates cardiac contractility by enabling thick-filament stabilization **(Figure 3.18 D)**; Troponin I which binds to the actin in the thin filaments to hold the actin-tropomyosin in place, inhibiting the contractile interaction between myosin and actin **(Figure 3.18 E)**; Tropomyosin which provides thin filament stability based on its interaction with actin **(Figure 3.18 F)**; Troponin T which is responsible for binding the troponin components to tropomyosin **(Figure 3.18 G)**; Desmin that maintains sarcomere integrity by linking the Z-bands to the plasma membrane **(Figure 3.18 H);** and Myosin Binding Protein (MyBP-C) which contributes to the stabilization of the thick filaments and regulate the formation of actin-myosin cross-bridges **(Figure 3.18 I)**. Contrary to our expectations, none of these proteins were significantly altered during obesity in myofilaments obtained from TFEB-restricted mice. These results suggest that despite alteration in Ca^{2+} transients and sarcomere lengths, phosphorylation-based changes of the sarcomeric proteins is not observed in hearts with TFEB deletion during obesity.

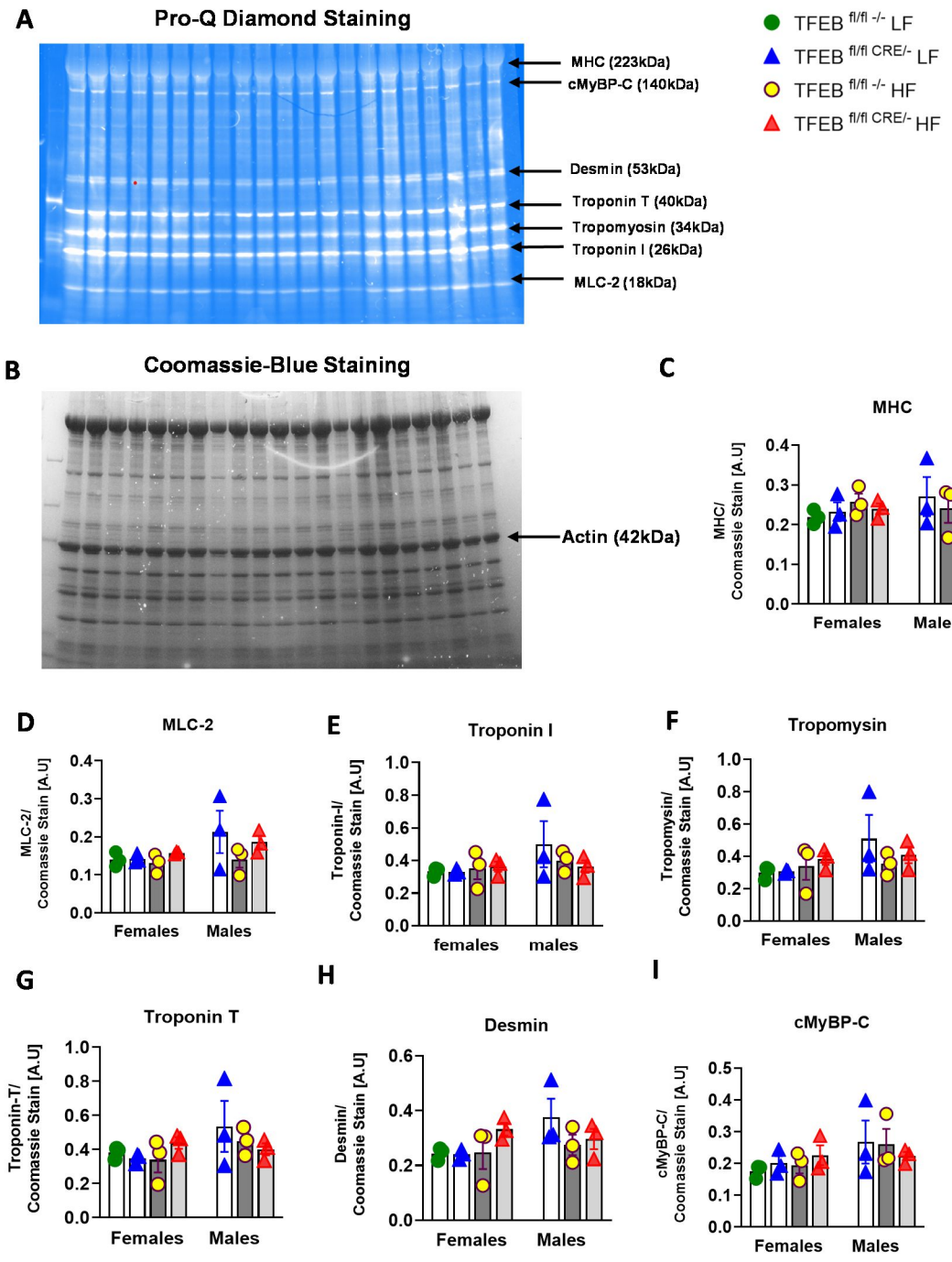

Figure 3.18 Cardiomyocyte-specific TFEB insufficiency did not alter contractile proteins following diet-induced obesity. Myofilament lysates were isolated from whole heart tissue. The membrane was stained with Pro-Q Diamond phosphoprotein stain followed by Coomassie blue staining overnight. Data is normalized to Coomassie blue protein stain. The graph represents mean ± S.E.M. Statistical analysis was performed using one-way ANOVA followed by Tukey's multiple comparison test, n=3(C-I), AU; Arbitrary Unit. Note: all the presented lanes are from the same membranes.

Chapter 4: Discussion

4.1 Study overview and summary of findings.

Despite glycemic and body weight control, patients with obesity and diabetes exhibit left ventricular muscle disease or cardiomyopathy, which occurs independently of vascular complications [152]. In experimental obese and diabetic models, altered cardiac energy metabolism is the earliest causative change observed prior to the onset of cardiomyopathy [24, 153]. However, metabolic changes are underestimated due to rapid metabolic transformation, underdiagnoses and delayed detection in human cases of metabolic cardiomyopathy [154]. In addition to metabolic remodeling, downstream complications of glucolipotoxicity are contributing factors in the development and progression of cardiomyopathy. Primarily mitochondrial, ER and, more recently, lysosomal dysfunction are central events in the initiation and progression of cardiomyopathy [155]. For example, loss of protein quality control leads to inhibition of protein degradation and promotes the build-up of misfolded proteins, accumulation of dysfunctional mitochondria, ROS overproduction, and myocyte cell death. Therefore, it stands to reason that proteotoxic stress secondary to glucolipotoxicity could be an early maladaptation in the diabetic heart, progressing to cardiomyopathy. Prior data from the Pulinilkunnil laboratory showed glucolipotoxicity impairs autophagic flux and suppresses lysosome biogenesis and function, causing cardiomyocyte injury and cellular stress in obese and diabetic hearts, highlighting the pivotal role of lysosome dysfunction in maintaining cardiac function during obesity. Furthermore, the Pulinilkunnil laboratory demonstrated that TFEB is a master regulator of autophagy, lysosomal biogenesis and lysosomal function and is significantly decreased in cardiomyocytes exposed to the lipotoxic (palmitate) or chemotoxic (DOX) environment in-vitro, ex-vivo and in-vivo [156]. Many studies have now definitively shown that loss of TFEB in the unchallenged heart renders the heart susceptible to dysfunction [157, 158]. However, the underlying mechanism by which loss of TFEB engages pathological pathway networks to remodel cardiomyocyte signaling, metabolism, and function remains unexplored. Moreover, it is unclear how palmitate specifically downregulates TFEB and inhibits its action in the cardiomyocyte.

In my thesis, I delved into the transcriptional and translational aspects of TFEB decline induced by palmitate in the heart. Additionally, I investigated the consequences of TFEB loss of function in obesity-mediated cardiomyopathy. Data from this study suggest that: 1) elevated miR-30b-5p levels are associated with palmitate-induced TFEB decline in H9C2 cells and atrial appendages from patients with obesity; 2) in the realm of post-translational regulation, palmitate expedites accelerated TFEB protein degradation, even in the presence of a proteasomal inhibitor, indicating the involvement of alternative mechanisms of degradation and transport; 3) the specific deletion of TFEB in cardiomyocytes, alongside DIO, leads to increased lipid deposition, decreased FA linked mitochondrial respiration, altered Ca^{2+} transients, and exacerbated body weight gain, impaired molecular insulin signalling, diastolic dysfunction, and atrial hypertrophy (Figure 4.1).

4.2 Palmitate-induced TFEB decline in the heart.

One of the goals of my thesis work was to elucidate if palmitate-induced TFEB decline involved miRNA induction and the subsequent degradation of TFEB. While numerous studies have identified miRNAs that govern cellular metabolism and autophagy in cancer, our understanding of how miRNAs influence cellular autophagy in obesity-induced lipotoxic cardiomyopathy remains limited. In cardiac cell lines, amongst the different miRNAs (miR29, miR-30, miR-132/212) tested that specifically target TFEB, miRNA 30b-5p was prominent in regulating TFEB. miRNA 30b-5p has previously been identified as a regulator of autophagy through its binding to CLEAR networks and its ability to modulate the transcriptional activity of TFEB within the nucleus of HEK 293 cells [133]. Studies from my thesis demonstrate definitively that lipotoxicity ex vivo via palmitate treatment or in vivo under conditions of obesity induces significant expression of miRNA 30b-5p with a concomitant decline in TFEB content. Conversely, the inhibition of miR-30b-5p in the cardiac cell line resulted in a significant reversal of palmitate-induced TFEB loss of content and function, suggesting that miRNAs play a critical role in regulating TFEB mRNA and protein and plausibly TFEB action. Our data agrees with a prior study wherein expression of miRNA 30b-5p increased in a murine model of myocardial infarction and hypoxia [159] and in exosomes of individuals diagnosed with type 2 diabetes mellitus [160]. Additionally, a study revealed that miRNA 30b-5p triggers

cardiomyocyte death by targeting Bcl-2 and that inhibiting miR-30b effectively reduced myocardial cell apoptosis induced by Ang II [161]. However, the exact mechanisms through which increased levels of miR-30b degrade TFEB and whether its is cytosolic or nuclear effect remains undetermined. Moreover, whether TFEB mediated changes in metabolism are an outcome of the direct effects of miR-30b on the lipid metabolizing pathway remains to be deciphered. Interestingly, miR-30b-5p altered the expression of lipid metabolizing genes such as peroxisome proliferator-activated receptor (PPAR-α), sterol-binding element regulatory protein 1 (SREBP-1), and glucose transporter 1 (GLUT1) in hepatocellular carcinoma Huh-7 cells [162] and during the progression of NAFLD.

TFEB is not only regulated by post-transcriptional mechanisms, but posttranslational pathways also alter the turnover of TFEB content. A previous study conducted in neuronal cells demonstrated that the inhibition of proteasomal degradation leads to TFEB dephosphorylation and its nuclear translocation [149], activating the autophagy-lysosome pathway. Sha et al. reported that TFEB is degraded by proteasome pathway with a half-life of 4–6 hrs in Hela cells and 13.5 hrs in SH-SY5Y [163] [149]. Notably, in my thesis, I estimated the half-life of TFEB in H9C2 cells to be 16 hrs which is higher than that reported in HeLa and SH-SY5Y cells, suggesting that the degradation rate is lower in cardiomyocytes than in other non-myocyte cell types. Moreover, saturated FA palmitate accelerates TFEB degradation. Unlike non-myocyte cells wherein TFEB degradation was primarily proteasomal, in the myocyte, proteasomal inhibition did not restore TFEB protein content in the presence of palmitate, signifying that palmitate-induced TFEB decline includes more than the proteasomal compartment, which is likely lysosomal, endosomal, or exosomal transport and degradation. The precise location of TFEB degradation remains to be determined, and mechanisms by which palmitate mobilizes TFEB for degradation still merit investigation.

4.3 Impact of myocyte deletion of TFEB on systemic metabolism

TFEB has emerged as an important regulator of cellular metabolism and survival, in addition to its canonical role in promoting lysosome biogenesis and function [125]. Indeed, several studies have demonstrated that TFEB is crucial in regulating energy metabolism in the liver, skeletal muscle, adipocytes, and macrophages [116, 164, 165].

Gain- or loss-of-function of TFEB in mouse liver or adipose tissue influences whole-body energy metabolism. For example, liver-specific TFEB knock-down mice show increased peripheral adiposity, whereas adipocyte-specific TFEB knock-down causes hepatic steatosis [164]. Overexpression of TFEB in the liver or adipocytes protects mice against diet-induced metabolic dysfunction [166]. Interestingly, following high-fat diet feeding, myocyte restricted TFEB KO male and female mice exhibit glucose and insulin intolerance compared to a low-fat diet group. Strikingly, female mice lacking TFEB display exacerbated body weight gain and glucose intolerance when compared to floxed female mice on a high-fat diet. Due to time constraints, I could not examine food intake and brown adipose tissue function, a driver of energy expenditure in rodents, which could likely be impacted in mice with myocyte-specific TFEB deletion and contribute to weight gain and glucose/insulin intolerance following DIO.

Systemic insulin and glucose intolerance are also driven by tissue-specific or cell-autonomous loss of insulin action [167]**.** Ex vivo insulin stimulation studies in cardiomyocytes revealed significant decreases in insulin-induced AKT phosphorylation at Ser473 in female KO mice on a high-fat diet, an effect not observed in male mice lacking myocyte TFEB. Interestingly, Sun et al. demonstrated that endothelial TFEB activation stimulates AKT signaling. Their research revealed that mice lacking TFEB, specifically in vascular endothelial cells, exhibit significantly impaired glucose tolerance compared to control mice when fed a high-fat diet [168]. Another study by Song et al. demonstrated that autophagy deficiency in mice with cardiomyocyte-specific inducible knock-down of Atg7 impairs whole-body glycemic control and insulin sensitivity and increases fat storage in subcutaneous and adipose tissue [169]. These findings agree with our data suggesting that systemic changes observed in glucose and insulin tolerance in response to high-fat diet feeding is attributed to changes in myocyte insulin signaling in mice lacking TFEB, and more pronounced in females with myocyte specific TFEB deletion, pointing to sexual dimorphisms in insulin signaling and sensitivity following loss of TFEB. However, it has yet to be determined whether cardiomyocyte-specific TFEBKO mice influence cellular energy metabolism in other non-cardiac tissues, and if so, how during DIO.

4.4 Non-canonical role of TFEB in governing cardiomyocyte energy metabolism and mitochondrial function.

The Pulinilkunnil laboratory previously showed that high-fat feeding increases DAG (32:0, 32:1, 36:1 and 38:5) and TAG (54:2, 54:3, 54:4) species within the heart after 16 weeks of diet feeding with a concomitant decline in TFEB and suppresses lysosomal function. Furthermore, silencing TFEB in H9C2 cells increases oleate indued lipid droplet accumulation. Conversely, TFEB overexpression in H9C2 cells decreased oleate-induced lipid droplet formation, suggesting that alterations in TFEB action are sufficient to regulate myocyte lipid content [140]. Moreover, a decrease in oleate-induced lipid droplet formation after TFEB overexpression persists in cells lacking Atg7, an activator of macroautophagy. This data suggests that TFEB-mediated regulation of lipid metabolism does not require a functional macroautophagy pathway in the cardiomyocyte. Therefore, we speculate that changes in cytosolic TAG hydrolyzing enzymes and changes in mitochondrial lipid oxidation drive changes in TAG accumulation following TFEB deficiency. Indeed, transcriptome analysis in TFEB-deleted cardiomyocytes revealed that loss of TFEB action induces differential expression of genes involved in lipid transport, lipid storage, FA metabolism, lipolysis, and lipophagy [140]. CD36 and PPARα alpha protein expression is decreased in unchallenged cardiac-specific TFEB-restricted cardiomyocytes [140]. Therefore, we posit that during obesity, TFEB deficiency in the cardiomyocyte exacerbates a decline in FA oxidation, increasing lipotoxic intermediates and diverting incompletely oxidized FA towards TAG. Indeed, my data revealed that FA-linked mitochondrial respiration is reduced in TFEB-deficient cardiomyocytes from DIO mice. We further reason that TFEB is critical for either transport, storage, or catabolism of lipids, which, when compromised during obesity and diabetes, contribute to lipotoxicity and cardiac dysfunction. Incomplete oxidation of FA and ensuing accumulation of lipotoxic intermediates in the heart increases mitochondrial ROS production leading to decreased stability of ETC complexes and impaired mitochondrial energetics and cardiac function [170].

4.5 Role of TFEB in calcium handling homeostasis and cardiac function.

Lipotoxicity increases ROS, which oxidizes membrane lipids in organelles, disrupting Ca^{2+}-led excitation-contraction coupling and inducing cell death [171]. Our

preliminary data indicated that in unchallenged mice, TFEB deficiency results in adaptive changes in Ca^{2+} handling, which is associated with TAG accumulation and inhibition of mitochondrial respiration. However, the mechanisms underlying Ca^{2+} handling changes and whether Ca^{2+} handling becomes impaired in $TFEB^{fl/fl\ Cre/-}$ mice challenged with DIO were unknown. Strikingly, $TFEB^{fl/fl\ CRE/-}$ myocytes from high fat-fed animals showed significant increases in intracellular Ca^{2+} during contraction (Max Ca) and a significant increase in Ca^{2+} transient amplitude (ΔCa). These data provided evidence that Ca^{2+} handling is affected during obesity in myocytes lacking TFEB. The rise in Ca^{2+} transient amplitude in $TFEB^{fl/fl\ Cre/-}$cardiomyocytes on a high-fat diet could be related to a decrease in L-type Ca^{2+} current or elevation in SR Ca^{2+} leak. The increased time to 80% Ca^{2+}decay in $TFEB^{fl/fl\ CRE/-}$ myocytes from high fat-fed animals, which represents the Ca^{2+} removal from the cytoplasm to the extracellular space through the NCX during the late part of the relaxation, could be associated with downregulation of SERCA1a and NCX gene expression which is yet to be ascertained. I further theorized that loss of TFEB that increases Ca^{2+} transient amplitude might modulate myofilament Ca^{2+} sensitivity, however, no significant effects were observed in myocytes from mice with TFEB deletion from both sexes. Contrary to our expectation, the observed alteration in Ca^{2+} dynamics in the $TFEB^{fl/fl\ CRE/-}$ cardiomyocytes occurred independent of any changes in sarcomere length during contraction or relaxation. These data suggest that the Ca^{2+} transient is significantly impacted by the loss of TFEB action, however the intracellular molecular mechanism of this regulation merits further investigation. Importantly, the link between TFEB and Ca^{2+} was reported in a prior study, wherein lysosomal Ca^{2+} regulates TFEB activity. This study showed that lysosomal Ca^{2+} release through mucolipin 1 (MCOLN1) activates calcineurin phosphatase, dephosphorylating TFEB and promoting TFEB nuclear translocation [124]. Furthermore, previous research emphasized the significance of the interaction between the endoplasmic reticulum (ER) and lysosome membranes in controlling Ca^{2+} signaling between these cellular compartments [172, 173]. Notably, a recent investigation revealed that suppressing TFEB in HeLa cells leads to an intriguing outcome: an elevated rate of Ca^{2+} re-uptake in the ER due to its influence on lysosome activity [174]. Whether lysosomal Ca^{2+} likely contributes to a higher intracellular Ca^{2+} transient in $TFEB^{fl/fl\ CRE/-}$ cardiomyocytes remains unanswered.

Ex vivo studies in the Pulinilkunnil laboratory demonstrated that TFEB silencing in palmitate-treated H9C2 and NRCM cells induced lysosomal dysfunction and cell death, which was rescued by TFEB overexpression [105]. Moreover, overexpressing constitutively active phosphorylation-resistant TFEBS142A in NRCM cells enhanced insulin-stimulated phosphorylation of AKT at Ser473 and Thr308, suggesting that TFEB activation prevents lipid overload-induced impairment of insulin signalling. Indeed, loss of TFEB perturbed Ca^{2+} handling during obesity was also reflected in increased atrial weight gain, diastolic dysfunction (both sexes), and ventricular weight (males only). These studies highlight that correcting TFEB deficit and mislocalization during obesity might ameliorate contractile dysfunction. Although cardiomyopathy occurs in males and females, it is unknown whether sex influences susceptibility to cardiomyopathy. Our data show that in high-fat diet-fed male and female mice, cardiomyocyte-specific TFEB deletion precipitates distinct cardiac and whole-body pathology; mechanisms of such sexual dimorphisms are understudied and merit further investigation.

4.6 Limitations and future directions.

While the results of this thesis provide valuable insights into the role of TFEB in obesity-mediated cardiac dysfunction, it is crucial to acknowledge the limitations. These limitations influence the scope and generalizability of the conclusions drawn from this study and require careful interpretation. Firstly, the study of miRNA-mediated transcriptional regulation of TFEB was limited to just one specific miRNA among the four that were initially validated. While we demonstrated that the elevation of miR-30b-5p is associated with palmitate-induced TFEB decrease in the heart, it is important to note that this finding does not provide a comprehensive molecular mechanism underlying this association. Since miR-30b-5p targets not only TFEB but also other members of the MiTF family of transcription factors, such as TFEC and TFE3, it becomes necessary to investigate the impact of this miRNA on other members of the MiTF protein family. Further studies are needed to gain a comprehensive understanding of their regulatory mechanisms. Moreover, the specific mechanism employed for inhibiting endogenous miRNA expression using an inhibitory mimic, such as whether it was based on an agomir or antagomir approach, has not been thoroughly investigated and merits clarification. In this thesis, I examined the recovery of TFEB content under palmitate-induced conditions

by inhibiting proteasomal activity. However, it is important to explore further and understand the additional mechanisms involved in promoting increased palmitate-mediated TFEB protein degradation in the heart, such as the contribution of lysosomal/endosomal degradation of TFEB and the mechanisms therein. The data obtained from in vivo animal studies in TFEB-deleted mice can be strengthened by mitigating time and breeding limitations since the number of mice assigned to the low-fat group was insufficient. Furthermore, molecular mechanisms underlying the physiological changes need to be deciphered. For example, deciphering mechanisms by which cardiomyocyte lipid metabolism and mitochondrial function are reprogrammed following TFEB decline, and specifically determining whether TFEB insufficiency in the cardiomyocyte alters substrate oxidation and TAG turnover and exploring the molecular mechanisms by which TFEB exerts control over cardiac lipid homeostasis. Moreover, how lipotoxicity-induced TFEB decline renders myocytes susceptible to ROS damage, abnormal mitochondrial dynamics, and diminished antioxidant capacity is an open question that remains to be addressed. Additionally, further investigation is needed to understand differences in the effects observed between sexes and to identify specific therapeutic targets for intervention.

Chapter 5: Conclusions

In conclusion, our study has revealed novel associations between elevated miR-30b-5p levels and palmitate-induced TFEB decrease in the heart. Additionally, we have determined the half-life of TFEB protein in H9C2 cells to be 16 hrs and investigated the impact of palmitate on TFEB protein degradation. We investigated the role of cardiomyocyte-specific TFEB deletion in obesity-mediated cardiomyopathy and uncovered its impact on body weight, systemic glucose and insulin tolerance, lipid storage, and FAO. This study also contributes significant insights into the alterations in Ca^{2+} transient amplitudes, contractile properties, and cardiac function resulting from TFEB restriction during nutrient overload conditions. Our results revealed that the effects of TFEB deletion and metabolic dysfunction differ between males and females, emphasizing the importance of considering sexual dimorphism in understanding and addressing cardiac-related conditions.

TFEB represents an appealing therapeutic target for many human diseases, including lysosome storage diseases (LSD), neurodegenerative diseases, and liver disease

[175-177]. Since TFEB plays an important role in regulating autophagy, lysosome biogenesis, and lysosome function, several attempts have been made to enhance the cellular clearance of macromolecules by inducing TFEB expression. This thesis sheds light on the tight linkages between TFEB and metabolism within cardiomyocytes, given the high nutrient and mitogenic demand of the heart to maintain functional homeostasis. This thesis also aimed to clarify the physiological role of TFEB in the cardiomyocyte and its distinction from fibroblasts, macrophages, and endothelial cells, which is vital for advancing TFEB biology. Probing intramyocellular mechanisms regulating TFEB and identifying pathways targeted by TFEB offers promising therapeutic options for treating patients at risk for metabolic cardiomyopathy. Conversely, it is also plausible that overexpressing TFEB without restoring autophagy could diminish myocyte viability since cardiac autophagic flux is reduced in DIO, and TFEB increases autophagosome formation [178]. Data from this thesis will advance knowledge to rationalize the utility of pharmaceutical activators of TFEB to prevent and/or reverse obesity-related heart disease.

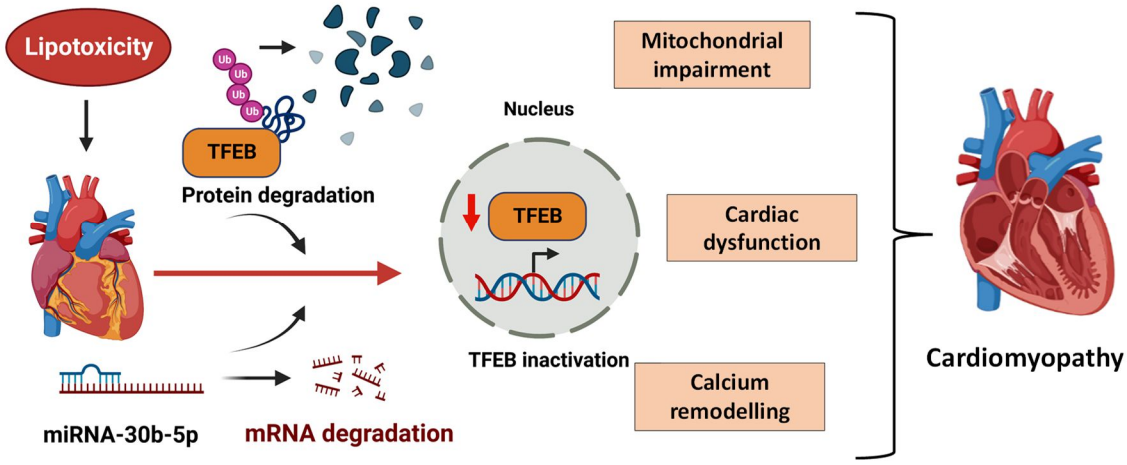

Figure 4.1 Proposed scheme of events.

References

1. Nuttall, F.Q., *Body Mass Index: Obesity, BMI, and Health: A Critical Review.* Nutr Today, 2015. **50**(3): p. 117-128.

2. Twells, L.K., et al., *Current and predicted prevalence of obesity in Canada: a trend analysis.* Canadian Medical Association Open Access Journal, 2014. **2**(1): p. E18-E26.

3. Collaborators, G.B.D.O., et al., *Health Effects of Overweight and Obesity in 195 Countries over 25 Years.* N Engl J Med, 2017. **377**(1): p. 13-27.

4. Bray, G.A., et al., *Obesity: a chronic relapsing progressive disease process. A position statement of the World Obesity Federation.* Obes Rev, 2017. **18**(7): p. 715-723.

5. Gonzalez-Muniesa, P., et al., *Obesity.* Nat Rev Dis Primers, 2017. **3**: p. 17034.

6. Lytvyak, E., et al., *Trends in obesity across Canada from 2005 to 2018: a consecutive cross-sectional population-based study.* CMAJ Open, 2022. **10**(2): p. E439-E449.

7. Valenzuela, P.L., et al., *Obesity and the risk of cardiometabolic diseases.* Nat Rev Cardiol, 2023.

8. Wibmer, A.G., et al., *Brown adipose tissue is associated with healthier body fat distribution and metabolic benefits independent of regional adiposity.* Cell Rep Med, 2021. **2**(7): p. 100332.

9. Aune, D., et al., *BMI and all cause mortality: systematic review and non-linear dose-response meta-analysis of 230 cohort studies with 3.74 million deaths among 30.3 million participants.* BMJ, 2016. **353**: p. i2156.

10. Ren, J., et al., *Obesity cardiomyopathy: evidence, mechanisms, and therapeutic implications.* Physiol Rev, 2021. **101**(4): p. 1745-1807.

11. Chen, C., et al., *Weight change across adulthood in relation to all cause and cause specific mortality: prospective cohort study.* BMJ, 2019. **367**: p. l5584.

12. Ebong, I.A., et al., *Mechanisms of heart failure in obesity.* Obesity research & clinical practice, 2014. **8**(6): p. e540-e548.

13. Organization, W.H. *Cardiovascular Diseases*. 2021.

14. Canada, P.H.A.o. *Heart Disease in Canada*. 2022.

15. Powell-Wiley, T.M., et al., *Obesity and cardiovascular disease: a scientific statement from the American Heart Association.* Circulation, 2021. **143**(21): p. e984-e1010.

16. Mechanick, J.I., et al., *Cardiometabolic-Based Chronic Disease, Adiposity and Dysglycemia Drivers: JACC State-of-the-Art Review.* J Am Coll Cardiol, 2020. **75**(5): p. 525-538.

17. Mahabadi, A.A., et al., *Association of pericardial fat, intrathoracic fat, and visceral abdominal fat with cardiovascular disease burden: the Framingham Heart Study.* Eur Heart J, 2009. **30**(7): p. 850-6.

18. Lee, J.J., et al., *Visceral and Intrahepatic Fat Are Associated with Cardiometabolic Risk Factors Above Other Ectopic Fat Depots: The Framingham Heart Study.* Am J Med, 2018. **131**(6): p. 684-692 e12.

19. Csige, I., et al., *The Impact of Obesity on the Cardiovascular System.* J Diabetes Res, 2018. **2018**: p. 3407306.

20. Larsen, T.S. and K.M. Jansen, *Impact of Obesity-Related Inflammation on Cardiac Metabolism and Function.* J Lipid Atheroscler, 2021. **10**(1): p. 8-23.

21. Miki, T., et al., *Diabetic cardiomyopathy: pathophysiology and clinical features.* Heart Fail Rev, 2013. **18**(2): p. 149-66.

22. Robertson, J., et al., *Body Mass Index in Young Women and Risk of Cardiomyopathy: A Long-Term Follow-Up Study in Sweden.* Circulation, 2020. **141**(7): p. 520-529.

23. Robertson, J., et al., *Higher Body Mass Index in Adolescence Predicts Cardiomyopathy Risk in Midlife.* Circulation, 2019. **140**(2): p. 117-125.

24. Bugger, H. and E.D. Abel, *Rodent models of diabetic cardiomyopathy.* Dis Model Mech, 2009. **2**(9-10): p. 454-66.

25. Peterson, L.R., et al., *Effect of obesity and insulin resistance on myocardial substrate metabolism and efficiency in young women.* Circulation, 2004. **109**(18): p. 2191-6.

26. Woodiwiss, A.J., et al., *Obesity promotes left ventricular concentric rather than eccentric geometric remodeling and hypertrophy independent of blood pressure.* Am J Hypertens, 2008. **21**(10): p. 1144-51.

27. Rodrigues, B., M.C. Cam, and J.H. McNeill, *Myocardial substrate metabolism: implications for diabetic cardiomyopathy.* J Mol Cell Cardiol, 1995. **27**(1): p. 169-79.

28. An, D. and B. Rodrigues, *Role of changes in cardiac metabolism in development of diabetic cardiomyopathy.* Am J Physiol Heart Circ Physiol, 2006. **291**(4): p. H1489-506.

29. Ingwall, J.S., *Energy metabolism in heart failure and remodelling.* Cardiovascular research, 2009. **81**(3): p. 412-419.

30. Ritterhoff, J. and R. Tian, *Metabolism in cardiomyopathy: every substrate matters.* Cardiovascular research, 2017. **113**(4): p. 411-421.

31. Kolwicz Jr, S.C., S. Purohit, and R. Tian, *Cardiac metabolism and its interactions with contraction, growth, and survival of cardiomyocytes.* Circulation research, 2013. **113**(5): p. 603-616.

32. Chabowski, A., et al., *Protein-mediated Fatty Acid Uptake in the Heart.* Curr Cardiol Rev, 2008. **4**(1): p. 12-21.

33. Chen, L., J. Song, and S. Hu, *Metabolic remodeling of substrate utilization during heart failure progression.* Heart failure reviews, 2019. **24**: p. 143-154.

34. Pascual, F. and R.A. Coleman, *Fuel availability and fate in cardiac metabolism: A tale of two substrates.* Biochimica et Biophysica Acta (BBA)-Molecular and Cell Biology of Lipids, 2016. **1861**(10): p. 1425-1433.

35. Haemmerle, G. and A. Lass, *Genetically modified mouse models to study hepatic neutral lipid mobilization.* Biochim Biophys Acta Mol Basis Dis, 2019. **1865**(5): p. 879-894.

36. Morales, P.E., J.L. Bucarey, and A. Espinosa, *Muscle Lipid Metabolism: Role of Lipid Droplets and Perilipins.* J Diabetes Res, 2017. **2017**: p. 1789395.

37. Bickel, P.E., J.T. Tansey, and M.A. Welte, *PAT proteins, an ancient family of lipid droplet proteins that regulate cellular lipid stores.* Biochim Biophys Acta, 2009. **1791**(6): p. 419-40.

38. Wolins, N.E., D.L. Brasaemle, and P.E. Bickel, *A proposed model of fat packaging by exchangeable lipid droplet proteins.* FEBS Lett, 2006. **580**(23): p. 5484-91.

39. Wolins, N.E., et al., *S3-12, Adipophilin, and TIP47 package lipid in adipocytes.* J Biol Chem, 2005. **280**(19): p. 19146-55.

40. Tran, D.H. and Z.V. Wang, *Glucose metabolism in cardiac hypertrophy and heart failure.* Journal of the American Heart Association, 2019. **8**(12): p. e012673.

41. Thorens, B. and M. Mueckler, *Glucose transporters in the 21st Century.* American Journal of Physiology-Endocrinology and Metabolism, 2010. **298**(2): p. E141-E145.

42. Shao, D. and R. Tian, *Glucose transporters in cardiac metabolism and hypertrophy.* Comprehensive Physiology, 2015. **6**(1): p. 331.

43. Martínez-Reyes, I. and N.S. Chandel, *Mitochondrial TCA cycle metabolites control physiology and disease.* Nature communications, 2020. **11**(1): p. 102.

44. Yap, J., et al., *Association of Diabetes Mellitus on Cardiac Remodeling, Quality of Life, and Clinical Outcomes in Heart Failure With Reduced and Preserved Ejection Fraction.* J Am Heart Assoc, 2019. **8**(17): p. e013114.

45. Holscher, M.E., C. Bode, and H. Bugger, *Diabetic Cardiomyopathy: Does the Type of Diabetes Matter?* Int J Mol Sci, 2016. **17**(12).

46. Ormazabal, V., et al., *Association between insulin resistance and the development of cardiovascular disease.* Cardiovasc Diabetol, 2018. **17**(1): p. 122.

47. Sharma, S., et al., *Intramyocardial lipid accumulation in the failing human heart resembles the lipotoxic rat heart.* FASEB J, 2004. **18**(14): p. 1692-700.

48. de Vries, J.E., et al., *Saturated but not mono-unsaturated fatty acids induce apoptotic cell death in neonatal rat ventricular myocytes.* Journal of lipid research, 1997. **38**(7): p. 1384-1394.

49. Schwingshackl, L. and G. Hoffmann, *Monounsaturated fatty acids, olive oil and health status: a systematic review and meta-analysis of cohort studies.* Lipids in health and disease, 2014. **13**: p. 1-15.

50. Riehle, C. and E.D. Abel, *Insulin signaling and heart failure.* Circulation research, 2016. **118**(7): p. 1151-1169.

51. Park, S.Y., et al., *Unraveling the temporal pattern of diet-induced insulin resistance in individual organs and cardiac dysfunction in C57BL/6 mice.* Diabetes, 2005. **54**(12): p. 3530-40.

52. Kahn, B.B. and J.S. Flier, *Obesity and insulin resistance.* J Clin Invest, 2000. **106**(4): p. 473-81.

53. Haidar, A. and H. Taegtmeyer, *Strategies for imaging metabolic remodeling of the heart in obesity and heart failure.* Current Cardiology Reports, 2022. **24**(4): p. 327-335.

54. Walther, T.C. and R.V. Farese Jr, *The life of lipid droplets.* Biochimica et Biophysica Acta (BBA)-Molecular and Cell Biology of Lipids, 2009. **1791**(6): p. 459-466.

55. Xu, S., X. Zhang, and P. Liu, *Lipid droplet proteins and metabolic diseases.* Biochimica et Biophysica Acta (BBA)-Molecular Basis of Disease, 2018. **1864**(5): p. 1968-1983.

56. Goldberg, I.J., C.M. Trent, and P.C. Schulze, *Lipid metabolism and toxicity in the heart.* Cell metabolism, 2012. **15**(6): p. 805-812.

57. Marfella, R., et al., *Myocardial lipid accumulation in patients with pressure-overloaded heart and metabolic syndrome [s].* Journal of lipid research, 2009. **50**(11): p. 2314-2323.

58. McGavock, J.M., et al., *Cardiac steatosis in diabetes mellitus: a 1H-magnetic resonance spectroscopy study.* Circulation, 2007. **116**(10): p. 1170-1175.

59. Sharma, S., et al., *Intramyocardial lipid accumulation in the failing human heart resembles the lipotoxic rat heart.* The FASEB Journal, 2004. **18**(14): p. 1692-1700.

60. Leopoldo, A.S., et al., *Cardiac remodeling in a rat model of diet-induced obesity.* Can J Cardiol, 2010. **26**(8): p. 423-9.

61. Koves, T.R., et al., *Mitochondrial overload and incomplete fatty acid oxidation contribute to skeletal muscle insulin resistance.* Cell metabolism, 2008. **7**(1): p. 45-56.

62. Brindley, D.N., et al., *Shedding light on the enigma of myocardial lipotoxicity: the involvement of known and putative regulators of fatty acid storage and mobilization.* Am J Physiol Endocrinol Metab, 2010. **298**(5): p. E897-908.

63. Finck, B.N., et al., *A critical role for PPARalpha-mediated lipotoxicity in the pathogenesis of diabetic cardiomyopathy: modulation by dietary fat content.* Proc Natl Acad Sci U S A, 2003. **100**(3): p. 1226-31.

64. Duncan, J.G., et al., *Rescue of cardiomyopathy in peroxisome proliferator-activated receptor-alpha transgenic mice by deletion of lipoprotein lipase identifies sources of cardiac lipids and peroxisome proliferator-activated receptor-alpha activators.* Circulation, 2010. **121**(3): p. 426-35.

65. Zhang, L., et al., *Cardiac diacylglycerol accumulation in high fat-fed mice is associated with impaired insulin-stimulated glucose oxidation.* Cardiovasc Res, 2011. **89**(1): p. 148-56.

66. Mori, J., et al., *Angiotensin 1-7 ameliorates diabetic cardiomyopathy and diastolic dysfunction in db/db mice by reducing lipotoxicity and inflammation.* Circ Heart Fail, 2014. **7**(2): p. 327-39.

67. Zhou, Y.T., et al., *Lipotoxic heart disease in obese rats: implications for human obesity.* Proc Natl Acad Sci U S A, 2000. **97**(4): p. 1784-9.

68. Li, C., et al., *The role of lipotoxicity in cardiovascular disease.* Emergency and Critical Care Medicine, 2022.

69. Di Filippo, C., et al., *Oxidative stress as the leading cause of acute myocardial infarction in diabetics.* Cardiovasc Drug Rev, 2006. **24**(2): p. 77-87.

70. Wold, L.E., et al., *Characterization of contractile function in diabetic hypertensive cardiomyopathy in adult rat ventricular myocytes.* J Mol Cell Cardiol, 2001. **33**(9): p. 1719-26.

71. Chen, Z., et al., *Energy substrate metabolism and oxidative stress in metabolic cardiomyopathy.* J Mol Med (Berl), 2022. **100**(12): p. 1721-1739.

72. Li, J., et al., *Cardiolipin remodeling by ALCAT1 links oxidative stress and mitochondrial dysfunction to obesity.* Cell Metab, 2010. **12**(2): p. 154-65.

73. Zima, A.V., et al., *Ca handling during excitation-contraction coupling in heart failure.* Pflugers Arch, 2014. **466**(6): p. 1129-37.

74. Turdi, S., N. Hu, and J. Ren, *Correction: Tauroursodeoxycholic Acid Mitigates High Fat Diet-Induced Cardiomyocyte Contractile and Intracellular Ca2+ Anomalies.* Plos one, 2016. **11**(4): p. e0154907.

75. Abdurrachim, D., et al., *Cardiac diastolic dysfunction in high-fat diet fed mice is associated with lipotoxicity without impairment of cardiac energetics in vivo.* Biochimica et Biophysica Acta (BBA)-Molecular and Cell Biology of Lipids, 2014. **1841**(10): p. 1525-1537.

76. Sharma, S., P. Jackson, and J. Makan, *Cardiac troponins*. 2004, BMJ Publishing Group. p. 1025-1026.

77. James, P., et al., *Nature and site of phospholamban regulation of the Ca2+ pump of sarcoplasmic reticulum.* Nature, 1989. **342**(6245): p. 90-2.

78. Carvajal, K., et al., *Ca(2+) mishandling and cardiac dysfunction in obesity and insulin resistance: role of oxidative stress.* Cell Calcium, 2014. **56**(5): p. 408-15.

79. Li, S.Y., et al., *Cardiac contractile dysfunction in Lep/Lep obesity is accompanied by NADPH oxidase activation, oxidative modification of sarco(endo)plasmic reticulum Ca2+-ATPase and myosin heavy chain isozyme switch.* Diabetologia, 2006. **49**(6): p. 1434-46.

80. Belke, D.D., E.A. Swanson, and W.H. Dillmann, *Decreased sarcoplasmic reticulum activity and contractility in diabetic db/db mouse heart.* Diabetes, 2004. **53**(12): p. 3201-8.

81. Yang, L., et al., *Endoplasmic reticulum stress and protein quality control in diabetic cardiomyopathy.* Biochim Biophys Acta, 2015. **1852**(2): p. 209-18.

82. Sano, R. and J.C. Reed, *ER stress-induced cell death mechanisms.* Biochim Biophys Acta, 2013. **1833**(12): p. 3460-3470.

83. Benbrook, D.M. and A. Long, *Integration of autophagy, proteasomal degradation, unfolded protein response and apoptosis.* Exp Oncol, 2012. **34**(3): p. 286-97.

84. Groenendyk, J., et al., *Biology of endoplasmic reticulum stress in the heart.* Circ Res, 2010. **107**(10): p. 1185-97.

85. Adams, C.J., et al., *Structure and Molecular Mechanism of ER Stress Signaling by the Unfolded Protein Response Signal Activator IRE1.* Front Mol Biosci, 2019. **6**: p. 11.

86. Sha, H., et al., *Stressed out about obesity: IRE1alpha-XBP1 in metabolic disorders.* Trends Endocrinol Metab, 2011. **22**(9): p. 374-81.

87. Hummasti, S. and G.S. Hotamisligil, *Endoplasmic reticulum stress and inflammation in obesity and diabetes.* Circ Res, 2010. **107**(5): p. 579-91.

88. Li, Y., et al., *Enrichment of endoplasmic reticulum with cholesterol inhibits sarcoplasmic-endoplasmic reticulum calcium ATPase-2b activity in parallel with increased order of membrane lipids: implications for depletion of endoplasmic reticulum calcium stores and apoptosis in cholesterol-loaded macrophages.* J Biol Chem, 2004. **279**(35): p. 37030-9.

89. Wang, X. and J. Robbins, *Proteasomal and lysosomal protein degradation and heart disease.* J Mol Cell Cardiol, 2014. **71**: p. 16-24.

90. Szegezdi, E., et al., *Mediators of endoplasmic reticulum stress-induced apoptosis.* EMBO Rep, 2006. **7**(9): p. 880-5.

91. Despa, S., et al., *Hyperamylinemia contributes to cardiac dysfunction in obesity and diabetes: a study in humans and rats.* Circ Res, 2012. **110**(4): p. 598-608.

92. Li, J., et al., *Role of autophagy in proteostasis: friend and foe in cardiac diseases.* Cells, 2018. **7**(12): p. 279.

93. Powell, S.R., et al., *The ubiquitin–proteasome system and cardiovascular disease.* Progress in molecular biology and translational science, 2012. **109**: p. 295-346.

94. McLendon, P.M. and J. Robbins, *Proteotoxicity and cardiac dysfunction.* Circulation research, 2015. **116**(11): p. 1863-1882.

95. Hu, J., et al., *Cardiac muscle protein catabolism in diabetes mellitus: activation of the ubiquitin-proteasome system by insulin deficiency.* Endocrinology, 2008. **149**(11): p. 5384-5390.

96. Liu, J., et al., *Targeting mitochondrial biogenesis for preventing and treating insulin resistance in diabetes and obesity: Hope from natural mitochondrial nutrients.* Advanced drug delivery reviews, 2009. **61**(14): p. 1343-1352.

97. Despa, S., et al., *Hyperamylinemia contributes to cardiac dysfunction in obesity and diabetes: a study in humans and rats.* Circulation research, 2012. **110**(4): p. 598-608.

98. Daleke, D.L., *Regulation of transbilayer plasma membrane phospholipid asymmetry.* Journal of lipid research, 2003. **44**(2): p. 233-242.

99. Feng, Y., et al., *The machinery of macroautophagy.* Cell research, 2014. **24**(1): p. 24-41.

100. Tanida, I., *Autophagosome formation and molecular mechanism of autophagy.* Antioxidants & redox signaling, 2011. **14**(11): p. 2201-2214.

101. Tanida, I., T. Ueno, and E. Kominami, *LC3 and Autophagy.* Autophagosome and phagosome, 2008: p. 77-88.

102. Barth, S., D. Glick, and K.F. Macleod, *Autophagy: assays and artifacts.* The Journal of pathology, 2010. **221**(2): p. 117-124.

103. Yang, J., et al., *The regulation of the autophagic network and its implications for human disease.* International Journal of Biological Sciences, 2013. **9**(10): p. 1121.

104. Xie, Z., et al., *Improvement of cardiac functions by chronic metformin treatment is associated with enhanced cardiac autophagy in diabetic OVE26 mice.* Diabetes, 2011. **60**(6): p. 1770-1778.

105. Trivedi, P.C., et al., *Glucolipotoxicity diminishes cardiomyocyte TFEB and inhibits lysosomal autophagy during obesity and diabetes.* Biochimica et Biophysica Acta (BBA)-Molecular and Cell Biology of Lipids, 2016. **1861**(12): p. 1893-1910.

106. Massey, A.C., C. Zhang, and A.M. Cuervo, *Chaperone-mediated autophagy in aging and disease.* Curr Top Dev Biol, 2006. **73**: p. 205-35.

107. Nishino, I., et al., *Primary LAMP-2 deficiency causes X-linked vacuolar cardiomyopathy and myopathy (Danon disease).* Nature, 2000. **406**(6798): p. 906-10.

108. Sugimoto, S., et al., *LAMP-2 positive vacuolar myopathy with dilated cardiomyopathy.* Intern Med, 2007. **46**(11): p. 757-60.

109. Chauhan, S., et al., *ZKSCAN3 is a master transcriptional repressor of autophagy.* Molecular cell, 2013. **50**(1): p. 16-28.

110. Sardiello, M., et al., *A gene network regulating lysosomal biogenesis and function.* Science, 2009. **325**(5939): p. 473-477.

111. Theodosakis, N., A.D. Pagan, and D.E. Fisher, *The role of MiT/TFE family members in autophagy regulation.* Current topics in biochemical research, 2021. **22**: p. 151.

112. Bronisz, A., et al., *Microphthalmia-associated transcription factor interactions with 14-3-3 modulate differentiation of committed myeloid precursors.* Mol Biol Cell, 2006. **17**(9): p. 3897-906.

113. Slade, L. and T. Pulinilkunnil, *The MiTF/TFE Family of Transcription Factors: Master Regulators of Organelle Signaling, Metabolism, and Stress AdaptationMIT/TFE Regulation of Lysosomal Autophagy.* Molecular Cancer Research, 2017. **15**(12): p. 1637-1643.

114. Napolitano, G. and A. Ballabio, *TFEB at a glance.* Journal of cell science, 2016. **129**(13): p. 2475-2481.

115. Palmieri, M., et al., *Characterization of the CLEAR network reveals an integrated control of cellular clearance pathways.* Human molecular genetics, 2011. **20**(19): p. 3852-3866.

116. Settembre, C., et al., *A lysosome-to-nucleus signalling mechanism senses and regulates the lysosome via mTOR and TFEB.* The EMBO journal, 2012. **31**(5): p. 1095-1108.

117. Li, L., et al., *A TFEB nuclear export signal integrates amino acid supply and glucose availability.* Nat Commun, 2018. **9**(1): p. 2685.

118. Napolitano, G., et al., *mTOR-dependent phosphorylation controls TFEB nuclear export.* Nat Commun, 2018. **9**(1): p. 3312.

119. Zhu, S.Y., et al., *The Role and Regulatory Mechanism of Transcription Factor EB in Health and Diseases.* Front Cell Dev Biol, 2021. **9**: p. 667750.

120. Puertollano, R., *mTOR and lysosome regulation.* F1000Prime Rep, 2014. **6**: p. 52.

121. Abu-Remaileh, M., et al., *Lysosomal metabolomics reveals V-ATPase-and mTOR-dependent regulation of amino acid efflux from lysosomes.* Science, 2017. **358**(6364): p. 807-813.

122. Xu, Y., et al., *YWHA/14-3-3 proteins recognize phosphorylated TFEB by a noncanonical mode for controlling TFEB cytoplasmic localization.* Autophagy, 2019. **15**(6): p. 1017-1030.

123. Sardiello, M., *Transcription factor EB: from master coordinator of lysosomal pathways to candidate therapeutic target in degenerative storage diseases.* Annals of the New York Academy of Sciences, 2016. **1371**(1): p. 3-14.

124. Medina, D.L., et al., *Lysosomal calcium signalling regulates autophagy through calcineurin and TFEB.* Nature cell biology, 2015. **17**(3): p. 288-299.

125. Franco-Juarez, B., et al., *TFEB; Beyond Its Role as an Autophagy and Lysosomes Regulator.* Cells, 2022. **11**(19).

126. Filipowicz, W., S.N. Bhattacharyya, and N. Sonenberg, *Mechanisms of post-transcriptional regulation by microRNAs: are the answers in sight?* Nat Rev Genet, 2008. **9**(2): p. 102-14.

127. Ha, T.Y., *MicroRNAs in Human Diseases: From Cancer to Cardiovascular Disease.* Immune Netw, 2011. **11**(3): p. 135-54.

128. Ying, S.Y., D.C. Chang, and S.L. Lin, *The microRNA (miRNA): overview of the RNA genes that modulate gene function.* Mol Biotechnol, 2008. **38**(3): p. 257-68.

129. Han, J., et al., *The Drosha-DGCR8 complex in primary microRNA processing.* Genes Dev, 2004. **18**(24): p. 3016-27.

130. Pratt, A.J. and I.J. MacRae, *The RNA-induced silencing complex: a versatile gene-silencing machine.* J Biol Chem, 2009. **284**(27): p. 17897-901.

131. O'Brien, J., et al., *Overview of MicroRNA Biogenesis, Mechanisms of Actions, and Circulation.* Front Endocrinol (Lausanne), 2018. **9**: p. 402.

132. Cai, J., et al., *MicroRNA-29 enhances autophagy and cleanses exogenous mutant αB-crystallin in retinal pigment epithelial cells.* Experimental Cell Research, 2019. **374**(1): p. 231-248.

133. Guo, H., et al., *Nuclear miR-30b-5p suppresses TFEB-mediated lysosomal biogenesis and autophagy.* Cell Death Differ, 2021. **28**(1): p. 320-336.

134. Wu, K., et al., *Bioinformatic screening for key mi RNA s and genes associated with myocardial infarction.* FEBS open bio, 2018. **8**(6): p. 897-913.

135. Corà, D., F. Bussolino, and G. Doronzo, *TFEB signalling-related MicroRNAs and autophagy.* Biomolecules, 2021. **11**(7): p. 985.

136. Zhang, Y., et al., *Emerging role of microRNAs in mTOR signaling.* Cellular and Molecular Life Sciences, 2017. **74**: p. 2613-2625.

137. Horita, M., C. Farquharson, and L.A. Stephen, *The role of miR-29 family in disease.* Journal of cellular biochemistry, 2021. **122**(7): p. 696-715.

138. Eskildsen, T.V., et al., *The microRNA-132/212 family fine-tunes multiple targets in Angiotensin II signalling in cardiac fibroblasts.* Journal of the Renin-Angiotensin-Aldosterone System, 2015. **16**(4): p. 1288-1297.

139. Mehta, A., et al., *The microRNA-132 and microRNA-212 cluster regulates hematopoietic stem cell maintenance and survival with age by buffering FOXO3 expression.* Immunity, 2015. **42**(6): p. 1021-1032.

140. Trivedi, P.C., et al., *Loss of function of transcription factor EB remodels lipid metabolism and cell death pathways in the cardiomyocyte.* Biochim Biophys Acta Mol Basis Dis, 2020. **1866**(10): p. 165832.

141. Ritchie, R.H. and E.D. Abel, *Basic Mechanisms of Diabetic Heart Disease.* Circ Res, 2020. **126**(11): p. 1501-1525.

142. Seymour, J., et al., *Non-invasive assessment of the cardiac effects of Chironex fleckeri and Carukia barnesi venoms in mice, using pulse wave doppler.* Toxicon, 2020. **185**: p. 15-25.

143. Joffe, II, et al., *Abnormal cardiac function in the streptozotocin-induced non-insulin-dependent diabetic rat: noninvasive assessment with doppler echocardiography and contribution of the nitric oxide pathway.* J Am Coll Cardiol, 1999. **34**(7): p. 2111-9.

144. Wang, X., et al., *Evaluation of the performance of serum miRNAs as normalizers in microRNA studies focused on cardiovascular disease.* J Thorac Dis, 2018. **10**(5): p. 2599-2607.

145. Avraham, R. and Y. Yarden, *Regulation of signalling by microRNAs.* Biochemical Society Transactions, 2012. **40**(1): p. 26-30.

146. Aguiar, C., et al., *Impact of Obesity on Postoperative Outcomes following cardiac Surgery (The OPOS study): rationale and design of an investigator-initiated prospective study.* BMJ Open, 2019. **9**(3): p. e023418.

147. Schneider-Poetsch, T., et al., *Inhibition of eukaryotic translation elongation by cycloheximide and lactimidomycin.* Nat Chem Biol, 2010. **6**(3): p. 209-217.

148. Aviner, R., *The science of puromycin: From studies of ribosome function to applications in biotechnology.* Comput Struct Biotechnol J, 2020. **18**: p. 1074-1083.

149. Li, C., et al., *Proteasome Inhibition Activates Autophagy-Lysosome Pathway Associated With TFEB Dephosphorylation and Nuclear Translocation.* Front Cell Dev Biol, 2019. **7**: p. 170.

150. Belke, D.D., et al., *Insulin signaling coordinately regulates cardiac size, metabolism, and contractile protein isoform expression.* J Clin Invest, 2002. **109**(5): p. 629-39.

151. Schillinger, W. and H. Kogler, *Altered phosphorylation and Ca2+-sensitivity of myofilaments in human heart failure.* Cardiovasc Res, 2003. **57**(1): p. 5-7.

152. Isfort, M., et al., *Metabolic dysfunction in diabetic cardiomyopathy.* Heart Fail Rev, 2014. **19**(1): p. 35-48.

153. Abe, T., et al., *Left ventricular diastolic dysfunction in type 2 diabetes mellitus model rats.* Am J Physiol Heart Circ Physiol, 2002. **282**(1): p. H138-48.

154. Asghar, O., et al., *Diabetic cardiomyopathy.* Clin Sci (Lond), 2009. **116**(10): p. 741-60.

155. Trivedi, P.C., J.J. Bartlett, and T. Pulinilkunnil, *Lysosomal Biology and Function: Modern View of Cellular Debris Bin.* Cells, 2020. **9**(5).

156. Trivedi, P.C., et al., *Glucolipotoxicity diminishes cardiomyocyte TFEB and inhibits lysosomal autophagy during obesity and diabetes.* Biochim Biophys Acta, 2016. **1861**(12 Pt A): p. 1893-1910.

157. Javaheri, A., et al., *TFEB activation in macrophages attenuates postmyocardial infarction ventricular dysfunction independently of ATG5-mediated autophagy.* JCI Insight, 2019. **4**(21).

158. Abe, T., et al., *Left ventricular diastolic dysfunction in type 2 diabetes mellitus model rats.* American Journal of Physiology-Heart and Circulatory Physiology, 2002. **282**(1): p. H138-H148.

159. Shen, Y., et al., *miRNA-30 family inhibition protects against cardiac ischemic injury by regulating cystathionine-gamma-lyase expression.* Antioxid Redox Signal, 2015. **22**(3): p. 224-40.

160. Stepien, E.L., et al., *Circulating ectosomes: Determination of angiogenic microRNAs in type 2 diabetes.* Theranostics, 2018. **8**(14): p. 3874-3890.

161. Wei, C., L. Li, and S. Gupta, *NF-kappaB-mediated miR-30b regulation in cardiomyocytes cell death by targeting Bcl-2.* Mol Cell Biochem, 2014. **387**(1-2): p. 135-41.

162. Zhang, Q., et al., *MiR-30b-5p regulates the lipid metabolism by targeting PPARGC1A in Huh-7 cell line.* Lipids Health Dis, 2020. **19**(1): p. 76.

163. Sha, Y., et al., *STUB1 regulates TFEB-induced autophagy-lysosome pathway.* EMBO J, 2017. **36**(17): p. 2544-2552.

164. Evans, T.D., et al., *TFEB drives PGC-1α expression in adipocytes to protect against diet-induced metabolic dysfunction.* Science signaling, 2019. **12**(606): p. eaau2281.

165. Mansueto, G., et al., *Transcription Factor EB Controls Metabolic Flexibility during Exercise.* Cell Metab, 2017. **25**(1): p. 182-196.

166. Evans, T.D., et al., *TFEB drives PGC-1alpha expression in adipocytes to protect against diet-induced metabolic dysfunction.* Sci Signal, 2019. **12**(606).

167. Petersen, M.C. and G.I. Shulman, *Mechanisms of Insulin Action and Insulin Resistance.* Physiol Rev, 2018. **98**(4): p. 2133-2223.

168. Sun, J., et al., *Endothelial TFEB (transcription factor EB) improves glucose tolerance via upregulation of IRS (insulin receptor substrate) 1 and IRS2.* Arteriosclerosis, thrombosis, and vascular biology, 2021. **41**(2): p. 783-795.

169. Zhang, Y., et al., *Adipose-specific deletion of autophagy-related gene 7 (atg7) in mice reveals a role in adipogenesis.* Proc Natl Acad Sci U S A, 2009. **106**(47): p. 19860-5.

170. Zhou, B. and R. Tian, *Mitochondrial dysfunction in pathophysiology of heart failure.* J Clin Invest, 2018. **128**(9): p. 3716-3726.

171. Jaquenod De Giusti, C., J. Palomeque, and A. Mattiazzi, *Ca(2+) mishandling and mitochondrial dysfunction: a converging road to prediabetic and diabetic cardiomyopathy.* Pflugers Arch, 2022. **474**(1): p. 33-61.

172. Kilpatrick, B.S., et al., *Direct mobilisation of lysosomal Ca2+ triggers complex Ca2+ signals.* J Cell Sci, 2013. **126**(Pt 1): p. 60-6.

173. Morgan, A.J., et al., *Bidirectional Ca(2)(+) signaling occurs between the endoplasmic reticulum and acidic organelles.* J Cell Biol, 2013. **200**(6): p. 789-805.

174. Sbano, L., et al., *TFEB-mediated increase in peripheral lysosomes regulates store-operated calcium entry.* Sci Rep, 2017. **7**: p. 40797.

175. Jiao, F., B. Zhou, and L. Meng, *The regulatory mechanism and therapeutic potential of transcription factor EB in neurodegenerative diseases.* CNS Neurosci Ther, 2023. **29**(1): p. 37-59.

176. Yan, S., *Role of TFEB in Autophagy and the Pathogenesis of Liver Diseases.* Biomolecules, 2022. **12**(5).

177. Spampanato, C., et al., *Transcription factor EB (TFEB) is a new therapeutic target for Pompe disease.* EMBO Mol Med, 2013. **5**(5): p. 691-706.

178. Pan, B., et al., *TFEB activation protects against cardiac proteotoxicity via increasing autophagic flux.* J Mol Cell Cardiol, 2017. **113**: p. 51-62.